Alma Mater Studiorum · University of Bologna

School of Science
Department of Physics and Astronomy
Master Degree Programme in Astrophysics and Cosmology

INVESTIGATING THE X-RAY PROPERTIES OF A BINARY SMBH CANDIDATE: THE CASE OF MCG+11-11-032

Graduation Thesis

Submitted by:
Letizia Vincetti

Supervisor:
Chiar.mo Prof. Cristian Vignali

Co-supervisor:
Dr. Paola Severgnini

Academic Year [2022/2023]
Graduation date [IV]

«Research is to see what everybody else has seen,
and to think what nobody else has thought.»
Albert Szent-Györgyi

Abstract

According to the ΛCDM cosmological model, galaxy evolution is mainly driven by major and minor mergers. Observational constraints suggest that the majority of galaxies hosts a SMBH, characterized by mass $M > 10^6 M_{sun}$, hence SMBH binaries are expected to be one of the natural results of the merger process. During the merger event, triggered by gas inflow, the two massive BHs could be activated and shine as AGN, defining a dual AGN system at kpc-scale separation. Through dynamical friction and three-body encounters, the BH pair hardens up to pc/sub-pc separation, thus forming a SMBH binary (SMBHB). The journey to coalescence is ensured in the end by Gravitational Wave (GW) emission, which is efficient when the pair is found at $< 10^{-2} - 10^{-3}$ pc distance.

My thesis project consists of the study of MCG+11-11-032, a radio-quiet Seyfert 2 (i.e. obscured) galaxy at $z = 0.0362$, identified as a promising SMBHB candidate (*Severgnini+18*). The X-ray emission is investigated through Swift-XRT monitoring campaigns, comprising both proprietary and archival datasets, for a total of 330 ksec of observational time over a period of $\sim$ 15 years. The X-ray modelling is highly sensitive to the source variability, observed in the modulation of the 0.2-10 keV XRT light curve and in the 15-150 keV BAT-123 months light curve (from which, a $\sim$ 25 months period was estimated, *Serafinelli+20*). Different physical mechanisms may be responsible for the source variability pattern, e.g. periodic accretion flows from the circumbinary accretion disk toward the mini-disks surrounding each BH. The double-peaked Fe Kα emission lines identified in the XRT spectra can be ascribed to the AGN orbital motion which can cause the lines to be Doppler-shifted and not detected at the rest-frame energy of 6.4 keV. Different spectral binning and summing procedure are considered in my work, in order to shed light in particular on line variability on different timescales. This is the preliminary, observational step needed to possibly interpret the complex variability behaviour of the emission lines of MCG+11-11-32 in the framework of mini and circumbinary disks models, predicted by many theoretical studies (e.g. *Dotti+12*). The properties of MCG+11-11-032 are still under discussion, since additional XRT monitorings are needed to place the results obtained so far on a more solid ground.

Despite all the candidate sources currently known, the study of dual and binary AGN is still in its infancy. Future facilities, like SKA in the radio, LISA for GW and NewAthena in X-rays, would definitively provide large sample of binary candidates, enabling a crucial multiwavelength synergy.

Contents

CHAPTER 1

Fundamentals of AGN Physics and SMBH Binaries

1.1 Introduction: What is an AGN?

The name Active Galactic Nuclei (AGN) identifies the extremely powerful phenomenon associated with the accretion mechanism onto a SuperMassive Black Hole (SMBH) [1] and was introduced to differentiate these objects from normal ("non active") galaxies. Looking back to the discoveries of the last century, in 1943 *Carl Seyfert* published an article in the Astrophysical Journal entitled "Nuclear Emission in Spiral Nebulae": he presented the spectra of the nucleus of six extragalactic nebulae, in which he identified broadened highly ionized emission lines (*Seyfert, 1943 [124]*). The first time a similar feature appeared in the observations was in 1909: *Fath* obtained spectra of nebulae now known as spiral galaxies, with strong optical emission lines (*Fath, 1909 [41]*). The AGN discovered by Seyfert were named Quasars (Quasi-Stellar Radio Sources) and soon after it was clear that stellar processes cannot be the energy source of such powerful and exotic objects. According to their energy output, luminosities and spectra, the most suitable hypothesis to unveil their nature was to consider in their core a massive compact object like a Black Hole (BH). The emission comes from the accretion of matter toward this central engine, among other physical processes in action, and covers almost the entire electromagnetic spectrum, from radio up to γ-rays (an illustrative AGN Spectral Energy Distribution (SED) is shown in Figure 1.1).

[1] A Black Hole is classified as SuperMassive if its mass is larger than $\sim 10^{5-6} M_{sun}$.

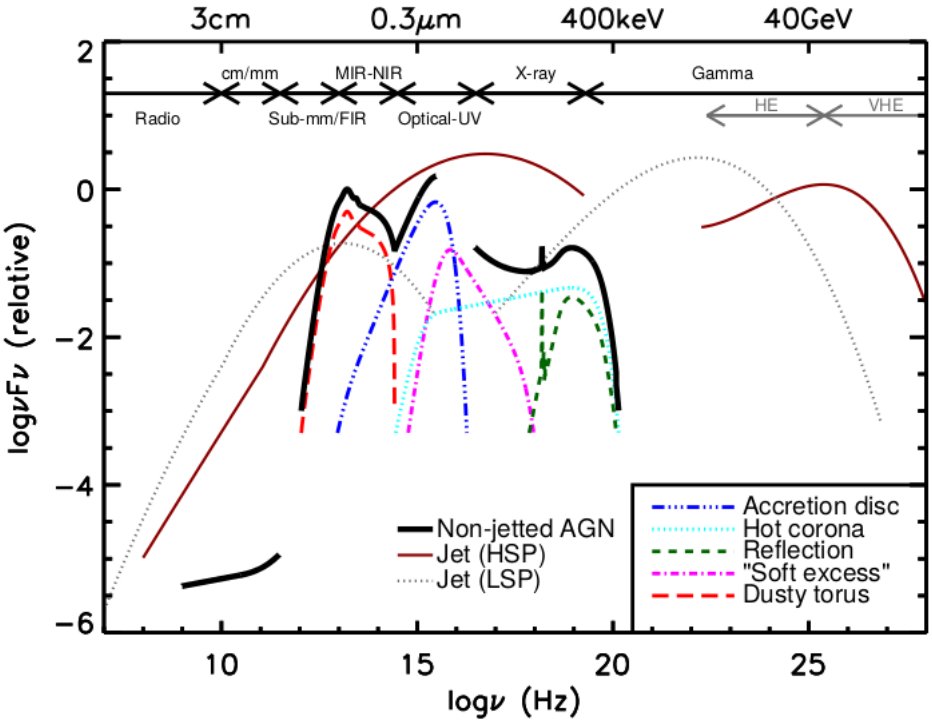

Figure 1.1: AGN broadband emission with contribution from single components. The energies span several orders of magnitude in frequency, from the radio to the γ-ray band. The most important components are the Accretion disk, with the characteristic Big Blue Bump in the optical-UV energy range, the reprocessed emission from a possibly clumpy torus in the MIR and the Hot Corona emission in form of a modified power law in the X-rays. The overall spectrum is shown in black for Non-Jetted AGN and in red/grey for Jetted AGN. *Credit: Harrison, 2014 [53].*

1.1.1 AGN structure

AGN can be defined as the observational result of the accretion mechanism onto a **SMBH**, that constitutes its nucleus.

The spatial region where the BH gravitational attraction dominates over the gravitational potential of the surrounding stars is called sphere of influence and its radius is defined as $R_{BH} = \frac{GM_{BH}}{\sigma_\star^2} \sim 100 \left(\frac{M_{BH}}{10^9 M_{sun}}\right) \left(\frac{200km/s}{\sigma_\star^2}\right)^2 pc$, where M_{BH} is the black hole mass and $\sigma_\star$ is the stellar velocity dispersion (in the second expression both accurately normalized) (e.g. *Ferrarese et al., 2005 [42]*). Several direct and indirect methods have been invoked to measure the mass of the compact object, e.g. dynamical measurements through stellar orbits in the surroundings, reverberation mapping technique, scaling relations and gas kinematics (*Peterson, 2010 [107]* for an overview on different methods).

Since BHs are physical entities whose structure collapsed under the control of gravity, the proper way to describe their extent is through a quantity called Schwarzschild radius $R_S = \frac{2GM_{BH}}{c^2} = 2r_g$ (r_g is the gravitational radius). R_S defines the boundary below which everything, even light, is trapped into the BH. In particular, for non-rotating BHs (Schwarzschild BHs) the innermost stable circular orbit (ISCO), the radius at which matter free falls into the BH, corresponds to $R \simeq 6r_g$ (e.g. *Colpi & Sesana, 2017 [23]*).
The Einstein's field equation, describing the gravitational field in the space-time under the

presence of some sources of energy, accounts for a general solution (*Kerr, 1963* [67]): the presence of a rotating mass perturbs the space-time, with rotational energy as gravitational energy source. The rotation is parametrized with "a", the dimensionless spin parameter, defined between 0 and 1 (i.e. $a = 0$ Schwarzschild BH, $a = 1$ for highly spinning BH). In case of rotating BHs (Kerr BHs) matter settles in stable circular orbits up to $R \simeq 1.24\, r_g$, but this distance depends on the rotation of the accreting matter relative to the one of the BH (i.e. for counter-rotating matter, the stable orbit is placed at $R \simeq 9\, r_g$, *Longair, 2011 [82]*).

Matter accretes on the BH through an **accretion disk** (AD, Multi-color Black Body emission), with temperature decreasing towards the centre of the structure ($T \approx R^{-3/4}$ functional dependence, e.g. see *Done, 2010 [30]*). Viscous forces, in action between adjacent annuli in the disk, transport angular momentum outward, while matter falls in the opposite direction, providing the fuel for the BH. Even in presence of viscosity, the orbits in the disk can be approximated as circular and almost Keplerian. The gravitational potential energy is converted into kinetic energy of the infalling gas and, in the end, in thermal emission of the disk (*Shakura & Sunyaev, 1973 [125]*). Consequently, the growth of the BH mass depends on the rate of accreted gas, considering that in the process part of it is converted into radiation. The efficiency of the process regulates the BH growth, parametrized as $\dot{M_{BH}} = \frac{1-\eta}{\eta}\frac{L_{acc}}{c^2}$, where η represents the efficiency of the accretion process and L_{acc} the luminosity of accretion. Actually, the flow is regulated by turbolent viscous motion, responsible for the transfer of angular momentum requested for accretion.

In order to parametrize the AGN luminosity, L_{Edd}, the Eddington Luminosity, is defined. L_{Edd} is the maximum luminosity that a BH can reach by accretion and, if exceeded, the accretion mechanism itself may be prevented (*Longair, 2011 [82]*). Under the assumptions of a spherically steady-state accretion and ionized hydrogen as accreting fuel, the gravitational force, supposed to act on protons [2] placed at distance R, is defined as:

$$F_{grav} = \frac{GM_{BH}m_p}{R^2} \tag{1.1}$$

The radiation pressure, pushing electrons outward and countering the inward motion driven by gravity, is defined as:

$$F_{rad} = \frac{L\sigma_T}{4\pi R^2 c} \tag{1.2}$$

where σ_T is the Thomson cross section and L the source luminosity. Comparing 1.1 and 1.2

$$L_{Edd} = \frac{4\pi GcM_{BH}m_p}{\sigma_T} = 1.26 \cdot 10^{38}\frac{M}{M_{sun}}\frac{erg}{s} \tag{1.3}$$

The Eddington luminosity can be exceeded in practice, since it constitutes a pure theoretical limit, derived under precise assumptions, that most of the cases are not satisfied (e.g. non

[2] The gravitational attraction acts on electrons as well, but since their masses are much smaller (i.e $m_p \simeq 1.67 \cdot 10^{-24}\, g$ while $m_e \simeq 9.11 \cdot 10^{-28}\, g$), they are neglected.

spherical accretion, different composition of the accreting gas).
The accretion luminosity is defined according to the amount of fuel that spirals toward the BH:

$$L_{acc} = \frac{GM_{BH}\dot{M}}{R} = \eta \dot{M} c^2 \tag{1.4}$$

where $\dot{M}$ stands for the mass accretion rate and η the efficiency. AGN are the most efficient sources in converting matter into radiation, with $\eta = 0.32$ for highly spinning Kerr BH.

The generally adopted model to describe the disk is a geometrically thin, optically thick (or Shakura-Sunyaev-SS) accretion disk (*Shakura & Sunyaev, 1973 [125]*). This configuration is associated with a radiatively efficient AD, with powerful emission. The other widely adopted model is the ADAF (advection dominated accretion flow) solution (*Narayan & Yi, 1995 [96]*). In this latter case, the energy is advected back to the flow sent to the compact system instead of being radiated away. The ADAF model is characterized by a geometrically thick, optically thin configuration and is associated with low accretion rate and much lower gas density; the cooling process is much less efficient and the flow retains most of its energy. Indeed, as the disk becomes hotter, it increases its thickness (*Netzer, 2013 [101]*).
The temperature of the emission associated with each annuli can be measured with the Stefan-Boltzmann formula and comparing it to the heat dissipated by the top and bottom surfaces of the disk, according to angular momentum studies. The total intensity depends on frequency as $I(\nu) \propto \nu^{\frac{1}{3}}$, with hard and soft parts of the emission decay as a function of the innermost and outermost radius, hence on the temperature at those distances from the central BH. The shape at low frequency is referred to as Rayleigh–Jeans regime and, on the other side, the Wien approximation refers to the exponential decay at high frequencies. In case of a BH with mass $10^8 M_{sun}$, with $\dot{M} = 1\, M_{sun}\, yr^{-1}$, the temperature of the disk emission is then of the order of $10^5 K$. Most of the emission is expected in the optical/UV, in the AGN rest frame.

According to the two-phase model, the cold accretion disk is in thermodynamical equilibrium with hot electrons of a structure called **corona**, made of hot and dilute gas, whose geometry and position, along with interested processes, are still under debate (*Netzer, 2013 [101]*). The corona structure results in a compact and small region in the range $3 - 10\, r_g$ (deduced from variability studies, e.g. *De Marco et al., 2011 [27]*, *Kara et al., 2014 [63]*, *Fabian et al., 2015 [37]*, from observations of the emissivity profile of the broad iron line, e.g. *Wilkins & Fabian, 2011 [142]*, and studies of variable obscuration due to AGN X-ray eclipses, e.g. *Risaliti et al., 2011 [116]*). Proposed geometries are the accredited slab-sandwhich corona (the corona "sandwiches" the disk, producing relatively soft spectra), the sphere+disk geometry or the torus+disk geometry and a patchy or "pill box" corona (where small coronal regions locate above and below the AD) (*Reynolds & Nowak, 2003 [113]*). Another widely adopted model is the "lampost" corona model, where the hot corona is approximated as a point source situated along the rotation axis of the disk of negligible vertical extension (e.g. *Corbin & Reynolds, 2018 [133]*). Recent polarimetric observations performed

by the Imaging X-ray Polarimetry Explorer (IXPE) are employed to investigate the corona geometry, since information about the angle and degree of polarization are directly linked with the corona morphology and structure. In order to show how powerful the IXPE results are, the results from *Gianolli et al.*' study of the radio-quiet Seyfert galaxy NGC 4151 are mentioned: combining IXPE data with XMM-Newton and NuSTAR observations, their polarimetric analysis discard the spherical-lampost geometry, since the estimated polarization angle was incompatible with the expected value of $\sim 1\%$. While, a slab model rather than a wadge-like geometry (similar to the slab-like, but with truncated AD and "hot accretion flow" extending up to the ISCO, with corona vertical extension increases as departing from the nucleus), further supported by Monte Carlo simulations, are both viable hypothesis (*Gianolli et al., 2023 [50]*).

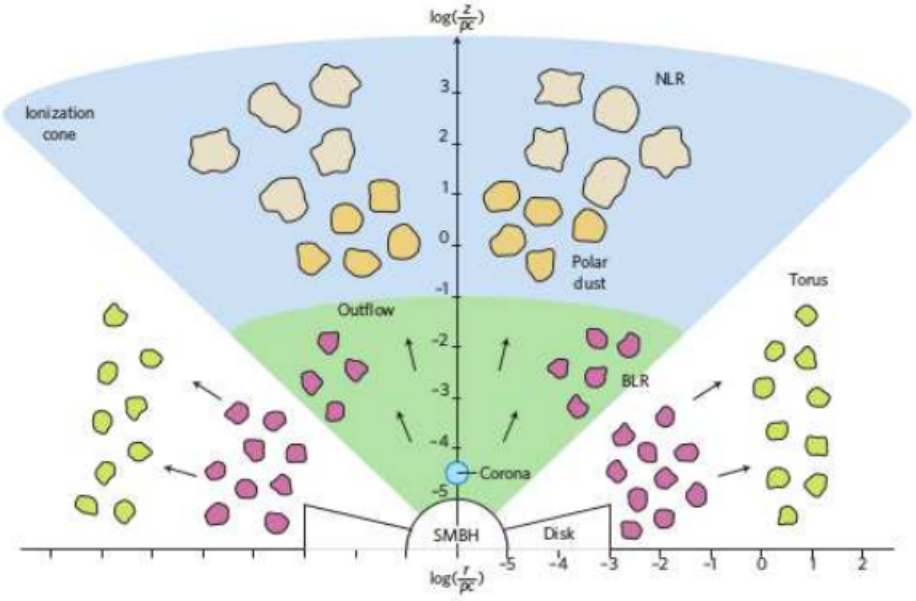

Figure 1.2: Scheme of AGN structure, with relative distances from the central engine, along the polar and equatorial direction. On the bottom, the distance scale in pc units. BLR clouds are shown in pink, NLR clouds in yellow/light beige, while the torus is shown as a dynamical, cloudy and filamentary structure in light green. The line of sight, that enables a clear view toward the central engine, is defined within the Ionization Cone, labeled in the figure. The central SMBH and relative AD are labeled as well. *Credit: Almeida & Ricci, 2017 [111].*

At larger distances from the central engine, the **Broad Line Region** and, more far away, the Narrow Line Region, are the origin of the detected optical/UV emission lines in AGN [3]. The BLR is an ensemble of individual clouds, with densities between $10^9 - 10^{11} cm^{-3}$, temperature around $10^4\,K$ and distances obtained thanks to reverberation mapping technique (approximately $R \sim 0.1 - 1pc$), as depicted in Figure 1.2. The broad optical emission lines originate from gas clouds heated by radiation from the AD, being broad since the BLR is characterized by too high gas density for forbidden transitions and gas velocities in the range

[3]First definition of obscured AGN derives directly from the absence of emission of BLR in the optical band (*Antonucci, 1993 [5]*)

$10^3 - 10^4\,km/s$ (e.g. *Hickox & Alexander, 2018 [55]*). The extension of the BLR proceeds up to the inner edge of the dusty torus structure (e.g. *Padovani et al., 2017 [103]*). To parametrize the BLR size, the efficiency of the line formation is used: the line emissivity is strongly suppressed at a distance from the central engine where the dust sublimation temperature of silicate and graphite (i.e. sublimation radii), whose most dust grains are made of, is reached. At those distances, and far away, the ionizing flux is absorbed (*Netzer, 2015 [100]*). The sublimation radii set a boundary between the dust-free clouds -the BLR- and the dusty ones -the torus-.
The **torus** constitutes the main component of obscuration (nature, modelisation and peculiar characteristics are described in Section 1.5).

The optical emission lines may be originated also from another line region, called **Narrow Line Region** (NLR), mentioned before. The typical velocities of the gas particles in NLR are $< 1000\,km/s$ and the much smaller densities, approximately $10^{3-4}\,cm^{-3}$, justify the observed narrow emission lines (the width is, however larger, than the simple thermal broadening). They are located further from the central BH and accretion disk, indeed they are subject to the gravitational influence of the host galaxy and, in some systems, extend up to kpc scales (*Hickox & Alexander, 2018 [55]*).

Relativistic magnetized jets can depart from the BH. The Radio-loud AGN constitutes just a fraction of the entire population, i.e. 10%. They are so powerful that can extend up to Mpc size, well beyond the host galaxy scale. Jets are defined as plasma collimated outflows and, in case of AGN, are often associated with hot spots and lobes structures, where the jet impacts the surrounding medium. Among jetted AGN, the class of Blazars stand out because their jet is at close inclination with respect to the line of sight, hence their emission suffers from Doppler boosting in the direction of the observer. Their peculiar broad-band (SED) is characterized by a double-peaked profile, with a first hump generated via synchrotron emission and the second hump originated from Inverse Compton either by the same electron population (synchrotron self-Compton) or from external photon field (external IC). These assumptions belong to the leptonic scenario. Another theory developed to explain the second SED component is the hadronic scenario, which postulates the origin of the second peak to reside in high-energy protons loosing energy via a synchrotron process or via photopion production, along with non negligible neutrino flux (*Mücke et al., 2000 [95]*). Due to their intense non-thermal emission and special viewing angle, Blazars can produce radiation up to the γ regime (*Padovani et al., 2017 [103]*). Understanding how jets structures are created, accelerated and confined is still a hot topic in AGN physics. One accredited scenario is the Blandford-Znajek process, where the magnetic field shapes and collimates the jet (*Blandford & Znajek, 1977 [11]*). The field is supposed to originate from the AD, to which it is anchored, and extracts energy from a rotating BH ejecting plasma along two opposite directions.

1.2 AGN classification

AGN classification is complex and variegate: some factors can be taken into account, like the presence of strong relativistic jets, the observer viewing angle and the accretion rate, the contamination from the host galaxy and surroundings (*Padovani et al., 2017 [103]*). All the classes can be collected below the same unified scheme: the AGN unified model (see section 1.3). There are two main "modus operandi" in the classification of AGN: first, considering their observational properties (e.g. observed SED, properties of the host galaxy, inclination of the source), while the second approach considers the physical parameters of the source (like BH mass and spin or BH accretion rate). Then, a sort of sub-category division considers specific observational features like the ionization level of the emission lines, their width and intensity or the presence of central obscuration (*Netzer, 2013 [101]*).

The first distinction treated here is between type I and type II AGN, depending on the obscuration of the central engine. Type I AGN are characterized by a clear and direct view of the nuclear region, i.e. the torus does not intercept the line of sight, and both the emission fro the AD and the lines emitted by the BLR and NLR are observable. Type II AGN are characterized by a line of sight that intercepts the torus, hence their continuum appeared flat and extincted (i.e. the emission from the AD is extincted and re-emitted at mid-IR wavelengths and the UV/optical spectra are characterized only by NLR). This idea underlies the AGN unification scheme (see section 1.3).
The spectral distinction appears evident also in the X-ray band, where the two classes show different flux level at lower-energies (i.e. below 10 keV) (e.g. *Malizia et al., 2003 [86]*). Among AGN classes, low-luminosity AGN having $M_B > -23$ (*Schmidt & Green, 1983 [117]*) are hystorically known under the name of Seyfert galaxies. Relating to the previous distinction, depending on the observer line of sight, they are classified as Sey type 1 or Sey type 2 galaxies. The picture is far more complex since there exist also intermediate type Seyfert Galaxies, e.g. Seyfert 1.8 or Seyfert 1.9 Galaxies (*Osterbrock, 1981 [102]*).
A useful tool in the characterization of this type of objects and differentiation from normal emission line galaxies is the diagnostic BPT diagram: *Baldwin et al. (1981) [8]* developed a method to distinguish between star-forming galaxies and AGN, using as parameter the strength of the line ratios [OIII]/Hβ versus [NII]/Hα [4]. Exploiting stellar population synthesis models and detailed self-consistent photoionization models, *Kewley et al.* (2001) [68] defined a theoretical "maximum star-burst line" on the diagram, as the upper limit of the theoretical pure stellar photoionization models: galaxies placed above this line are potentially dominated by an AGN. An empirical line was later added by *Kauffmann et al.* (2003) [64] to further differentiate pure star-forming galaxies from composite galaxies, which are possibly defined by both a metal-rich stellar population and an AGN. We note that in this

[4]The emission lines are chosen to have similar wavelengths to reduce the effect of dust reddening on the emission line ratio.

classification the emission-line spectroscopy concerns only the narrow-line emitting regions. In addition, the class of LINERs (Low-Ionization Nuclear Emission-Line Region) can be included in BPT diagrams as well, since also this class is characterized by relatively strong radiation field, but not as powerful as one of Seyfert Galaxies.

Another important distinction is between Radio Loud (RL) and Radio Quiet (RQ) AGN: the observational parameter here is the Radio Loudness parameter R, defined as the ratio between the AGN flux density in the radio band (e.g. at 5 GHz) and the optical flux density (in the B-band, at 4400 Å). If $R > 10$ the AGN is classified as RL, while if $R < 10$ the AGN is RQ (*Kellermann et al., 1989 [66]*). Another observational evidence of the presence of a dichotomy in radio selected AGN corresponds to their morphology and radio power. *Fanaroff and Riley (1974) [39]* developed a classification scheme according to the morphological shape of the observed radio galaxy: sources with extended radio structures are divided according to their brightness profile, edge darkened (or core-brightened) (FR I) vs. edge brightened (or FR II). The ratio between the highest surface brightness regions at the sides of the central galaxy and the entire source extension (from lowest surface brightness contours) in the first class remains below 0.5, while in the second group is larger than 0.5 (*Padovani et al., 2017 [103]*). The extended vs. compact source separation is observed also in the spectral shape: the synchrotron power-law continuum, typical of radio galaxies, with dependence like $\nu^{-\alpha}$, differentiates in a flat one (with $\alpha < 0.5$) or a steep one (with $\alpha > 0.5$) and corresponds to the groups of flat and steep radio sources, respectively.

Radio Galaxies evidences different accretion mechanism: the class of Low-Excitation Radio Galaxies (LERGs) and High-Excitation Radio Galaxies (HERGs) are defined according to the Excitation Index (EI), obtained using line ratios as in BPT diagnostic diagrams (first suggestion from *Hine & Longair, 1979 [56]*). If $EI < 0.95$, the engine powering the emission process is radiatively inefficient and characterized by an ADAF kind of accretion disk, while if $EI > 0.95$ the AD is possibly a SS-disk like and so radiatively efficient one (*Buttiglione et al., 2010 [15]*).

In the recent review from *Padovani et al. (2017) [103]*, the authors suggest a new definition of AGN classes, that regroups AGN according to the mode of the accretion mechanism (radiatively efficient vs. radiatively inefficient) and the relativistic jet strength (weak unification model): for example, most of FR II radio galaxies, HERGs, and jetted Quasars are grouped in the class of radiatively efficient AGN with strong jets, while non-jetted Type I and Type II AGN belong to the class of radiatively efficient but with weak (if not absent) jet AGN.

1.3 AGN unification

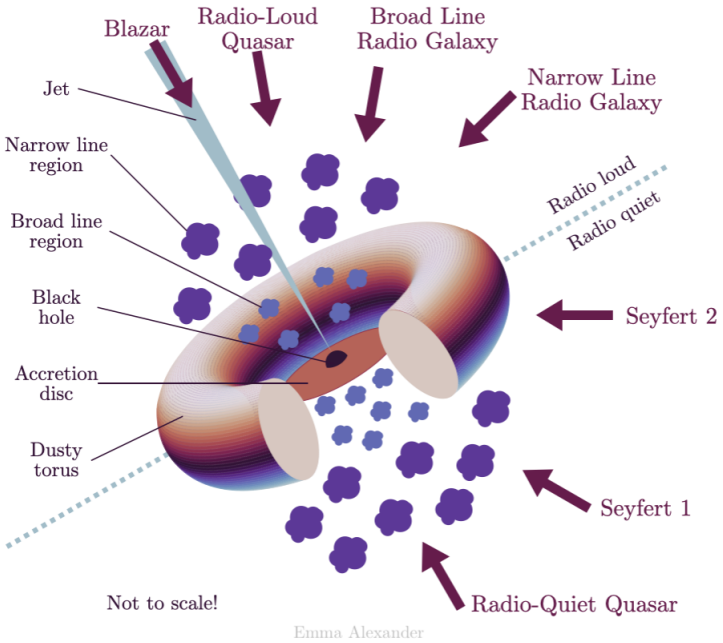

Figure 1.3: AGN unified scheme. *Credit: adopted from Urry & Padovani, 1995 [134].*

"AGN unification is the idea that the large diversity of observed AGN properties can be explained by a small number of physical parameters" (*Netzer, 2015 [100]*). The "unification by inclination" scheme groups in one single phenomenon all the AGN classes. In 1985, *Antonucci and Miller* associated diverse observational properties with the same physical mechanism: the accretion onto a compact object. Their work concerned the study of a Seyfert II Galaxy, NCG 1068, with polarized emission that resembles the one of a Seyfert I object (*Antonucci & Miller, [4]*). The polarized emission is generated by the scattering of nuclear emission with free electrons in the polar direction (NLR?), above and below the disk structure. In this picture, the torus, made of dust in a smooth or clumpy distribution around the AD, is the main component that stands in the path of the photons and, depending on the observer's viewing angle, obscures the nucleus.

As shown in Figure 1.3, the observational appearance depends on the line of sight and on the source luminosity. The picture divides jetted, on the top, and non-jetted AGN, at the bottom, BL and NL Radio Galaxies according to viewing angle and Seyfert I and Seyfert II Galaxies depending on torus obscuration.

Even so diversified, all the species in this big AGN "zoo" share some common characteristics: large bolometric luminosities ($L_{bol} = 10^{40} - 10^{48}\ \frac{erg}{s}$), emission on different wavebands across the electromagnetic spectrum and duty cycle pattern.

1.4 AGN High-Energy Emission

The X-ray band is the energy band defined by frequency in the range $3{\cdot}10^{16} < \nu < 3{\cdot}10^{19}\,Hz$, with associated energies from 0.1 keV up to 100 keV. X-ray emission can penetrate through large column density of material and can give access to the most central region of AGN, where it is produced. The X-ray band is also less affected by the host galaxy contamination. An example of the AGN X-ray spectrum is shown in Figure 1.4, where three main components are highlighted: the *primary power-law* (in green), with the photoelectric cut off at lower energies due to obscuration, the *soft excess* (in red) and the *reflection component* (in blue), with the characteristic Compton Hump and the prominent iron emission line.

The main component, the power-law continuum, is produced by accretion disk photons up-scatter by the hot electrons in the corona, through Inverse Compton scattering. The thermal Comptonization in action defines the process of multiple scattering of a photon due to a thermal (or quasi–thermal) distribution of electrons (*Pozdnyakov et al., 1983 [110]*). The resulting spectrum is the sum of the single electron scatterings and is in form of a power-law function:

$$J(\nu) \propto \nu^{-\frac{\delta-1}{2}} = \nu^{-\alpha} \tag{1.5}$$

given an electron population distributed as $N(E) = N_0 E^{-\delta}$, with α defined as the spectral index (*Fanti & Fanti, 2012 [40]*). If the flux is measured as $photons\,cm^{-2}\,s^{-1}$, rather than $keV\,cm^{-2}\,s^{-1}$, then the power-law emission has the exponent in terms of the photon index Γ, defined as $\frac{\delta+1}{2} = \alpha + 1$. The typical intrinsic slope is $\Gamma \sim 1.8$ and fit the spectrum of unobscured AGN (e.g. *Dadina, 2008 [26]*).

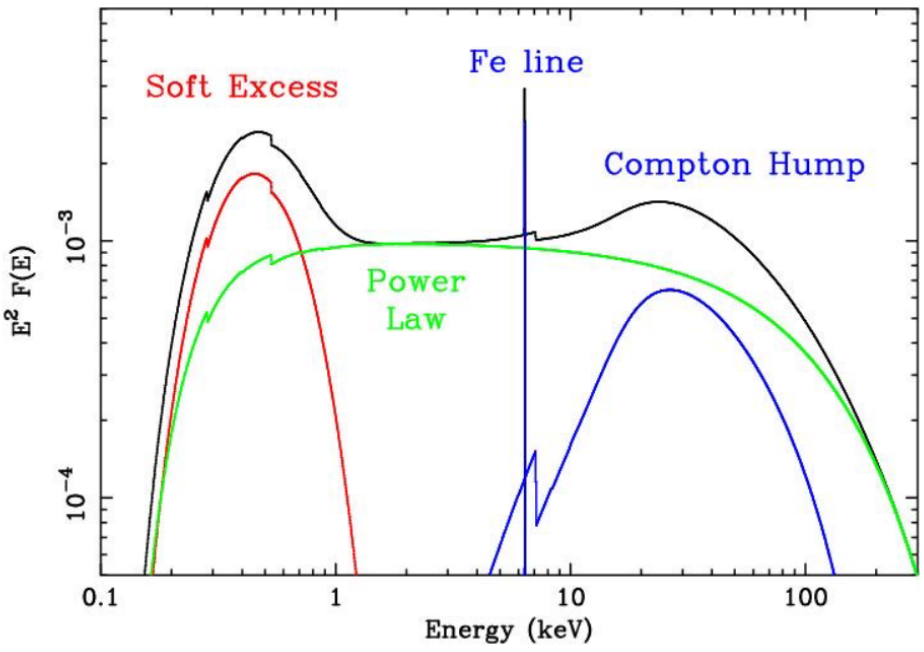

Figure 1.4: Representation of the components of AGN X-ray emission in X-ray spectrum scheme. *Credit: Fabian, 2006 [35].*

This emission is truncated at low energies because of photoelectric absorption by the K-shell electrons in the nuclear surroundings medium. The higher the obscuration, the larger the energy of the cut-off and the spectrum results more depressed in the soft band. The cross section for photoelectric absorption is defined as $\sigma_{ph} \propto Z^5 E^{-3.5}$, with Z the atomic number of the absorbing material and E the photon energy (*Morrison & McCammon, 1983 [94]*). The associated optical depth of the medium causing absorption is $\tau_e(h\nu) = \int \sigma_e N_H dl$ with N_H the number density of hydrogen atoms ($\#particles/m^3$) integrated over the path of unit element dl travelled by the photons (*Longair, 2011 [82]*)
In case of ionized (or partially ionized) absorbing material, the medium is defined as warm absorber and, from a spectral point of view, is characterized by strong bound–free absorption edges typically below 1 keV, like Oxygen edges around 0.7-0.8 keV (*Reynolds & Fabian, 1995 [112]*). Obscuration and its spectral characterization are described in details in the following section 1.5.

The Soft Excess is defined as excess with respect to the power law emission in the low energy band below 1 keV (first evidence from *Singh et al., 1985 [126]* and *Arnaud et al., 1985 [6]*). Two preferred scenarios are actually under debate: in the first case, Comptonization process to the UV seed disk photons by a warm (i.e. $kT \sim$ 0.1-1 keV) and optically thick corona is considered (e.g. *Done et al., 2012 [31]*); the second case is the relativistically blurred reflection scenario, where broad emission lines by corona irradiation in the inner region of the AD are produced (*Crummy et al., 2006 [24]*).

Part of the photons produced by the hot corona are backscattered mainly into the AD. Here, the photons are reprocessed producing the reflected spectrum (e.g. *Ricci et al., 2011 [115]*). In particular, the X-ray photons interacting with the accretion disk can be:

1. absorbed by metals in the disk, if $E_{ph} < 10$ keV;
2. Thomson scattered in the upward direction if 10 keV $< E_{ph} <$ 40 keV;
3. by Compton recoil effect, scattered in the direction of the disk. At high energies, the cross section of interaction is smaller and photons penetrates in the disk and are later absorbed (high energy cut-off). This mechanism is responsible for the characteristic Compton Hump peaking at $E \sim 30\,keV$ (*Magdziarz & Zdziarski, 1995 [84]*).

The interaction with the disk and with the torus, generates also the peculiar iron emission line (neutral line at 6.4 keV), along with a plethora of fluoresence lines from most abundant metals. Among them, because of the large cosmic abundance and fluorescence yield [5], the iron line is the most prominent one (see the following subsection).

[5]The fluorescence yield is defined as the probability that an excited ion will de-excite via fluorescence radiative emission rathen than via Auger effect. The Auger effect consists of a rearrangement of electron in the atom to replace the vacancy, with no photon emission, but the subsequent ejection of an atomic electron.

1.4.1 The Iron Line

The iron line stands out as the main observable of the reflection continuum, in addition to a plethora of other, less prominent, emission lines from most abundant metals like Magnesium, Silicium, Carbon, Nichel.
The iron fluorescent line is the result of an atomic transition, due to the absorption of an X-ray photon by an inner-shell electron (mostly K-shell ones) and, if the photon energy is sufficient, the subsequent electron ejection. The electron vacancy is replaced through a decay of one upper electron, from an outer shell, to the empty lower atomic level, followed by a photon emission. This effect is in contrast with the other possible non-radiative transition, called Auger effect, which also for iron is way less probable (*Longair, 2011 [82]*).
The line transition from the atomic level n=2 to n=1 is labelled Kα line. Its energy depends on the ionization state of the element, so the rest frame value of $6.4\,keV$ is the neutral one (in principle, there are two components of the Kα iron line, the Kα_1 at 6.404 and Kα_2 at 6.391 keV) (*Fabian & Miniutti, 2005 [38]*). Other iron fluorescent lines are produced in case of different ionization levels, with He-like iron (Fe XXV) and H-like iron (Fe XXVI), at 6.7 keV and 6.97 keV, respectively.

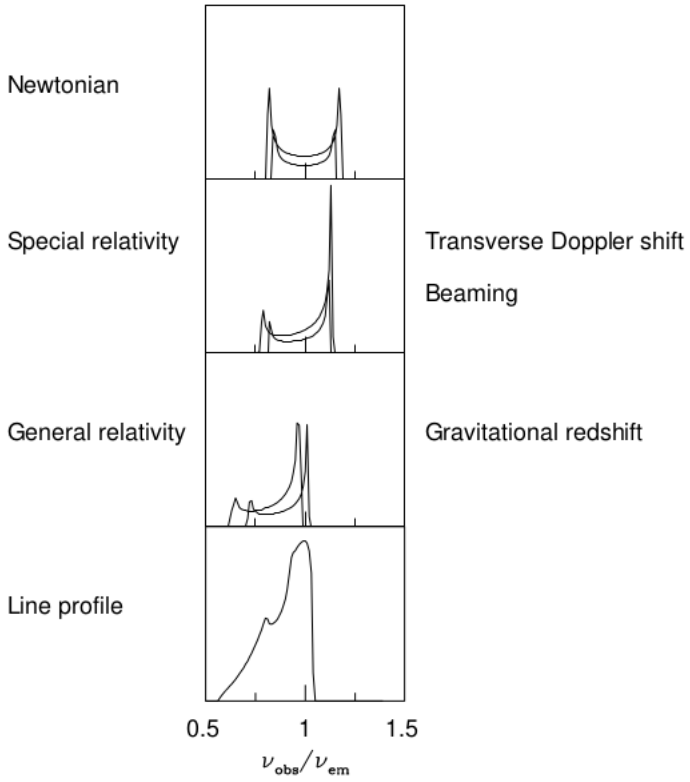

Figure 1.5: Narrow Iron line sketch modified by relativistic effects. *Credit: Fabian et al., 2000 [36].*

The Kα line can appear blurred and broadened due to Doppler and gravitational redshift effects, important when produced close to the central object, where this line is thought to originate. Being the line intrinsically narrow, this feature represents a crucial tool for

studying the dynamics of the emitting region. In case of non-relativistic AD, the line profile appears symmetric and double-horned (Newtonian case in the Figure 1.5). The broadening of the line is caused by the vicinity to the central black hole, where the Keplerian velocity of the disk annuli is higher. From this standard configuration, because of Doppler beaming effect, the blue extent is enhanced compared to the red one; then, by transverse Doppler shift, the profile results redder. In the end, including also General Relativity effect (the deviation of photons because of a strong gravitational field), a significant shift to red frequencies of overall skewed line is observed (*Ghisellini, 2013 [49]*). The final spectral shape appears asymmetric and with a steep blue wing and an extended red one. The parameters that regulate the entire shape are:

1. BH spin: the spin parameter "a" can be inferred from the line profile broadening, since its strictly connected with the concept of ISCO (for spin-ISCO connection, see the previous paragraph 1.1.1). The closer to the central BH, the larger the line broadening.

2. disk inclination: the "blue"-side energy of the line is strongly determined by the inclination of the observer line of sight with respect to the accretion disk axis, meaning that the profile is broadened going from a face-on to an edge-on configuration.

3. emissivity profile: it indicates where most of the photons of the line are produced. The emissivity profile traces the energy dissipation on the disk, since it originites from disk illumination by hard X-rays from the hot corona, illumination determined by the energy dissipation and hence by the heating events in the corona itself (*Fabian & Miniutti, 2005 [38]*). A simple power-law is used to describe its shape: $\epsilon(r) \propto r^{-q}$, with q the emissivity index. Larger q, e.g. $q = 6$ (note $q = 3$ corresponds to standard value), means that most of the photons are generated closer to the BH, hence the line profile appears broadened because of larger GR effect. Indeed, this means that the illumination is concentrated on the inner region of the AD.

The strength of the line is measured through its Equivalent Width (EW), i.e. how prominent is the line compared to the continuum. The EW is defined as

$$EW_\nu = \int \frac{F_C - F_\nu}{F_C} d\nu \tag{1.6}$$

with F_C is the continuum flux expected without the line and F_ν the line flux (*Longair, 2011 [82]*). It is measured in eV units and depends upon the geometry of the accretion disk, the elemental abundances of the reflecting matter, the inclination angle at which the reflecting surface is viewed, and the ionization state of the surface layers of the disk (*Fabian et al., 2000 [36]*).

The iron emission line can be followed by a weaker or stronger absorption edge, depending on the element ionization level and condition of the surrounding environment. An edge

feature can be observed whenever the energy of the incoming photons is exactly equal to, or slightly larger than, the precise electronic transition or, in this case, to the binding energy of the K-shell electron, so that it suffers from photoelectric absorption. The neutral iron K-edge is located at 7.1 keV and is observed at larger energies as the ionization level increase, till it disappears for competely ionized iron (*Fabian et al., 2000 [36]*). The ionization level is parametrized by $\xi(r) = \frac{L_X}{n\,r}\, erg\, cm^{-1}\, s^{-1}$ with n the electron density and r the distance from the ionising flux of luminosity L.

1.5 AGN Obscuration Model

In the SED of AGN, one of the main components is the mid-infrared emission (mid-IR, at $\lambda \sim 10 - 20 \mu m$), obtained from reprocessed radiation originated in the central region by the torus structure. The dusty torus is defined as a geometrically thick structure surrounding the accretion disk and hot corona. Initially described as a smooth dust distribution, this possibility was soon ruled out by comparison with observations (see *Hickox & Alexander, 2018 [55]* for reference studies). To date, it is known that the dusty torus is a clumpy agglomeration of dust clouds, whose concentration decreases going from the equatorial plane toward the perpendicular on the disk plane (see figure 1.6 for obscuration distribution). In addition, it appears to be a dynamic structure, rather than a static one, and is placed within about 10 pc under the gravitational influence of the SMBH (*Hickox & Alexander, 2018 [55]*). Since most of the current facilities cannot reach such small scales, the torus models are necessary in order to emulate the observed SEDs and investigate torus properties.
As introduced in the AGN classification and unification scheme (sec 1.2 and 1.3) obscured sources can be defined as the class of objects where the emission from the AD is partially or totally absorbed, because intercepted by material toward the observer (*Hickox & Alexander, 2018 [55]*). Actually, dust made of silicates and graphites causes extinction in the UV-IR energy band, while gas is the main responsible for SED depression in case of X-ray radiation. The parameter used to evaluate the level of obscuration intercepted along the line of sight is the hydrogen column density N_H and represents the equivalent hydrogen density to the absorption metals. An AGN is defined as X-ray obscured for $N_H > 10^{22}\, cm^{-2}$. AGN with $N_H \simeq 10^{24}\, cm^{-2}$ are defined Compton-thick. The clumpy nature of the torus manifests as an inhomogeneity of its properties like composition, temperature (T) and density.

From the IR observations, the toroidal region divides the dust-free BLR and the distant NLR (*Almeida & Ricci, 2017*). Indeed, the dust sublimation temperature plays an important role in defining the boundary between the BLR and outer dusty torus (for details see sec 1.1.1).
From the mid-IR spectroscopy, the two main classes of AGN (SeyI - SeyII) can be recognized because of the peculiar Silicate feature at 9.7 μm, found in emission for unobscured/type 1 systems and in absorption for the obscured/type 2 AGN (e.g. *Hao et al, 2007 [51]*).

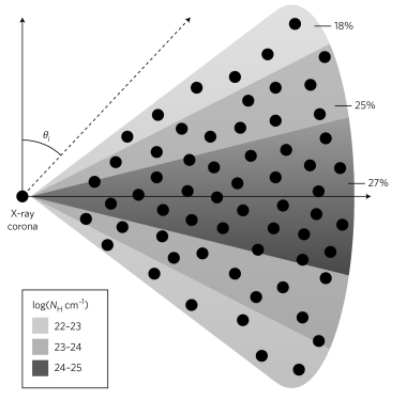

Figure 1.6: Level of obscuration depending on the line of sight, in terms of inclination Θ_i angle to the observer. *Credit: Almeida & Ricci, 2017 [111].*

A useful technique to identify obscured AGN is the modelling of their X-ray spectra, since the photon index of the primary power-law component is flattened to values below the usual 1.8 of non obscured sources (e.g. *Piconcelli et al., 2005* [108]). In addition, by looking at the spectral shape at larger energies, the presence of a strong iron Kα line, above the usual reflection component with the characteristic Compton Hump, as in Figure 1.4, suggests that the object can be classified as obscured AGN.
The torus is not the only obscuring medium in AGN but multiple components are involved: BLR, NLR and the host-galaxy, on scales larger than 10 kpc. The simplest scenario of the "obscuration produced by the orientation" of the dusty torus is complicated by additional interaction between AGN emission and nuclear starburst, generated by the large amount of gas inflowing toward the central SMBH and transformed into a starburst disk.
Under this consideration, AGN obscuration places within the description of the connection between the central SMBH and its host galaxy, for the self-regulating feedback mechanism (both fuelling and feedback processes).

1.6 AGN variability

AGN variability can be observed at almost all wavelengths (*McHardy, 2010 [88]*), with important hard X-ray fast variations possibly connected to regions at small distance from the BH (causality argument). Some hints of correlation between different bands also exist. The timescales of energy fluctuations span from days (in X-ray band also hours) up to years. Systematic studies on a large AGN sample (e.g. *Soldi et al., 2014 [128], Vagnetti et al., 2016 [135]*) are performed in order to discover some variability pattern. Usually, this pattern can be ascribed to some AGN structure/process instabilities, e.g. the disk corona or the accretion rate in the disk.
In X-ray, Power Spectral Density (PSD) is used to define the light curve variability. The PSD is defined as the mean value of the squared amplitude as a function of the temporal

frequency (*Serafinelli et al., 2020 [119]*). Specifically, any time series function, as in case of AGN variability, can be represented by a combination of separate periodic signals with frequencies ν. The time series can be decomposed into a frequency series and the PSD obtained by the square of the Fourier transform of the signal (*Kozłowski, 2016 [73]*). In particular, even in the case of a low signal-to-noise ratio or in sinusoidal/quasi-sinusoidal shape hidden by noise, using PSD allows to recognize some period trends in light curve.
The main issue with AGN variability is that it comes as the result of many stochastic processes, therefore comparable to noise (in particular, in case of shortest timescale), being difficult to model and so validate in the source spectrum (*Serafinelli et al., 2020 [119]*).

1.7 Galaxy Merger Theory: The Formation of a SMBH Binary

The adopted cosmological model describing the Universe is the ΛCDM model, that states the presence of three distinct components of the cosmic fluids: matter, radiation and dark energy. The relevant contribution is defined in terms of density parameters, derived from different studies, such as CMB modelling, mass measurement in galaxy clusters, weak-gravitational lensing. In this picture, the Universe is homogeneous and isotropic, according to the cosmological principle, and geometrically flat, meaning a total dimensionaless density parameter $\Omega = 1$, made of a matter fraction of $\Omega_{m,0} = 0.3$, a radiation contribution negligible being $\Omega_{rad,0} \simeq 10^{-5}$ and a dark energy density parameter of $\Omega_{\Lambda,0} = 0.7$. The model is defined CDM because the majority of the matter component is in the form of Cold Dark Matter. The Λ letter states for non-zero cosmological constant (e.g. *Cimatti, Fraternali, Nipoti, 2020 [18]*).

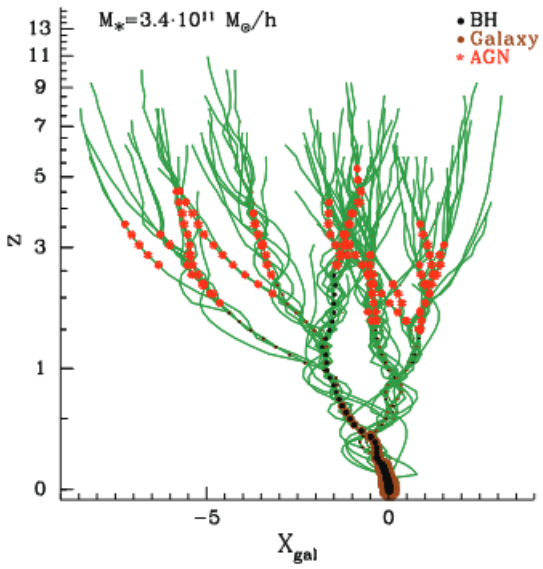

Figure 1.7: AGN merger tree model, tracing the merger history of a parent galaxy of stellar mass $M_\star = 3.4 \cdot 10^{11}\, M_{sun}/h$ from present time up to z=10. *Credit: Marulli et al., 2009 [87].*

According to this theory, galaxy formation and evolution are triggered by merger events, both of major and minor entities. Baryonic matter aggregates to form gravitationally collapsed objects, like galaxies, following the channels of dark matter halos evolution. Therefore, the past history of galaxies interactions can be described in light of the Merger Tree Model (Figure 1.7) and the associated 'bottom-up' formation scenario (*White & Rees, 1978 [141]*): the first smaller and less massive galaxies formed in mini-halos structured around $z \sim 20$ (*Volonteri et al., 2003 [139]*).
As these systems evolve through multiple mergers, larger and larger halos are produced and host, in the end, in case of major merger events, final elliptical galaxies.

The merger history of dark matter halos is investigated through Monte Carlo and N-body simulations (e.g. *Cole et al., 2000 [19]*, *Volonteri et al., 2003 [139]*, *Zivancgalaxiesev et al., 2020 [144]*), which allow also to reveal the connection between the evolution of massive and super-massive black holes and the respective galactic one (i.e. BH-galaxy co-evolution).
According to the mass ratio parameter $q = \frac{M_1}{M_2}$, with $M_1 \geq M_2$, the mergers are classified as major mergers, when $q > 4$ [6] and minor mergers, when $q < 4$, mainly linked to isolated BH population. In the former case, the less massive galaxy, named "satellite", sinks toward the centre of the major one because of dynamical friction, with also gas fuelling (the amount of gas depends on the halo properties) and activating the accretion process (e.g. *Koss et al., 2018 [72]*).

In the SMBH-galaxy co-evolution paradigm, the galaxy formation and evolution is regulated by the AGN activity, i.e. the growth of SMBH and the AGN feedback. The connection between the compact object and its host system manifests with different scaling relations between the BH mass and the galactic properties (like host spheroid mass, luminosity, stellar velocity dispersion, *Kormendy & Richstone, 1995 [70]*, *Magorrian et al., 1998 [85]*, *Ferrarese & Merritt, 2000 [43]*, *Gebhardt et al., 2000 [47]*). The co-evolution can be illustrated through phases of a "cosmic cycle" (*Hopkins et al., 2006 [58]*), in Figure 1.8. When isolated disk galaxies interact and possibly give rise to a merger event, the BH is activated and shine as AGN. This coalescence phase is the most powerful and, at the same time, the most obscured (in this case AGN appear as ULIRG/sub-mm galaxies), since the gas inflow triggers both starburst and AGN activity (*Hopkins et al., 2006 [58]*) as suggested from simulations (e.g. *Di Matteo et al., 2005 [29]* , *Springel et al., 2005 [129]*). Then, AGN feedback, along with Supernova feedback, expel most of the gas, leaving a highly dust-reddened or IR-luminous quasars ("blowout" phase). The self-regulatory feedback mechanisms consists on a common gas reservoir that constitutes the fuel for BH growth and, through feedback impact, the fuel supply recycled in star formation processes (e.g. *Harrison et al., 2017 [52]*). After dust removal, the "traditional" quasar object becomes optically visible and, finally, when it fades, the galaxy remnant relaxes leaving a "dead quasar" in a normal galaxy evolving passively

[6] These mergers are responsible for the formation of SMBH binary systems (SMBHB) *Volonteri et al., 2003 [139].*

(*Hopkins et al., 2008 [57]*). The connection between the BH and the host body is also reflected in the BHAR (Black Hole Accretion Rate) and SFR (Star Formation Accretion Rate), being the two curves closely linked at all redshift (e.g. *Mandau & Dickinson, 2014 [83]*).

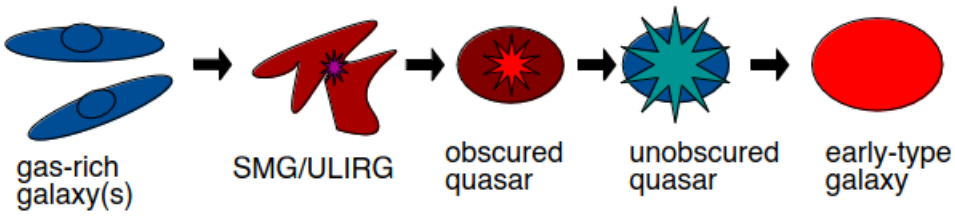

Figure 1.8: Schematic representation of the major merger "cosmic cycle" phases. *Credit: Alexander & Hickox, 2012 [3].*

1.7.1 Binary evolution

Since each massive galaxy harbours in its centre a massive BH (e.g. *Ferrarese & Ford, 2005 [42]*), when two galactic systems interact, the compact objects are found at close separations, giving rise to what is defined a SMBH binary.
The evolution progresses from two distinct systems observed at separation of $\sim 100\,kpc$ to single remnant with an unbound couple of BHs at separation $< 1\,kpc$ (e.g. *De Rosa et al., 2019 [28]*).
Under singular isothermal sphere hypothesis, the binary is theoretically formed when the relative separation is

$$a_{BHB} = \frac{G(M_1 + M_2)}{2\sigma^2} = 0.2\, M_{BHB,6}\, \sigma_{100}^{-2}\, pc \tag{1.7}$$

where $M_{BHB,6} = (M_1 + M_2)$ in units of $10^6\, M_{sun}$ and σ_{100} is the velocity dispersion of the host galaxy in units of $10^2\, km/s$ (*Dotti et al., 2012 [32]*). This separation is comparable to the sphere of influence of a BH of mass $M_{BH} = (M_1 + M_2)$.
The binary dynamical evolution depends on the relative mass ratio and on the gas richness of the host galaxy. In *Capelo et al., 2015 [16]*, through hydrodynamical simulations, they studied the growth and accretion of SMBH in galaxy merger and recognized three main phases: stochastic phase, with small accretion rate values; the merger phase, characterized by enhanced AGN activity, and the remnant phase, where the accretion is powered by same gas reservoir. This evolutionary steps are connected with the binary evolution itself.

In general, three main stages in the evolution of binary systems can be accounted for:

1. **Pairing phase**. The two BHs approach each other, moving toward the centre of the common potential well, due to the interaction of the system with neighbouring stars through dynamical friction (*Begelman et al., 1980 [10]*). The systems are not

gravitationally bound yet and are named at this stage "Dual AGN" [7], with separation between $\sim 1\,pc$ and $\sim 100\,kpc$ (e.g. *De Rosa et al., 2019 [28]*).

2. **Hardening phase**. At this stage, the binary hardens, so the compact objects are found at smaller and smaller separation, due to three-body encounters (star-binary) (*Colpi, 2014 [22]*). The pair is now gravitationally bound. The gravitational slingshot mechanism predicts that the star in question is possibly ejected to infinity with a velocity $v_\star \sim \sqrt{\frac{G(M_1+M_2)}{a}}$, carrying away energy and angular momentum, leading to further hardening of the binary at each interaction (e.g. *Sesana et al.,2006 [120]*). The distance between the components of the systems could achieve sub-pc/pc scales, becoming ultimately a "Binary AGN" (e.g. *De Rosa et al., 2019 [28]*), at an orbital separation smaller than $10\,pc$. The binary may stall in this situation, i.e. BHs separation $a_{BHB} \sim 0.1 - 1pc$, and not proceed toward the final coalescence, a theoretical issue known as 'last parsec problem', to which some solutions have been postulated (see below for details).

3. **Gravitational Wave inspiral phase**. The final orbital angular momentum is removed when gravitational radiation becomes efficient, around $10^{-2} - 10^{-3}\,pc$ separation, leading to the coalescence of the two BHs in a timescale that depends on the masses involved, but typically smaller than $10^8\,yrs$ (e.g. *De Rosa et al., 2019 [28]*). This last phase is also called "decoupling phase", because the binary can break away from the circumbinary disk structure. The CBD formation and role in the binary evolution is discussed later in this section.

As mentioned at point 2., the characterization of the binary evolution is more complex than this simple qualitative description: whenever the binary interacts with a star, pushing it far away, it starts depleting the surroundings. This tiny and closed environment, where stellar orbits are found close to the BHB and are perturbed by the rotating quadrupole component of the binary's potential, is called "binary loss cone" (*Milosavljević & Merritt, 2003 [91]*). The consequence is an increase in the binding energy of the binary and a decrease of its semi-major axis. Since the number of stars in the loss cone decreases at each interaction and the binary hardens, for spherical galaxies, a star/gas refill is needed to repopulate the cone via a two-body relaxation process and to allow, in the end, the binary coalescence (*Vasiliev et al., 2015 [136]*). However, this process results on a timescale larger than the Hubble time. This is what the "last parsec problem" is about (e.g. *Milosavljević & Merritt, 2003 [91]*).
At present time, this topic is still controversial, since in the literature many studies suggest that this problem is just "an artefact of the oversimplifying assumption of sphericity of the relic galaxy" (*Colpi et al., 2014 [22]*). In spherical galaxies, a secondary slingshot of returned stars in the cone, because not ejected from the system by the previous interaction,

[7] In the following treatment, BHs/SMBHs are considered now activated by the fuelling of gas during the the merger process, and so referred to as AGN.

can support the binary decay (*Sesana et al., 2007 [120]*). For non-spherical systems, like axisymmetric, triaxial, or irregular galaxies, the number of stars that intercepts the loss cone along their orbit is potentially larger (e.g. *Vasiliev et al., 2015 [136]*). Another viable theoretical mechanism could be the interaction with a third SMBH, or even a fourth SMBH, derived from a later merger event (e.g. *Bonetti et al., 2016 [12]*). This third compact object forms a hierarchical triplet, where the order of orbital separation between compact objects defines an inner and outer binary; this process increases up to 20% the predicted fraction of SMBHBs at low redshift that reaches coalescence (*Volonteri et al., 2003 [139]*).

The eccentricity parameter traces the binary evolution along its journey from separate distant systems to single remnant object. Basically, circular binary systems tends to remain circular, while eccentric ones increase their eccentricity as the system hardens (in addition, because of the angular momentum conservation argument, counterrotating stars with the binary extract more angular momentum and cause an increase in the eccentricity) (*Dotti et al., 2012 [32]*). The eccentricity is also regulated by the type of the surrounding environment.

Indeed, it is worth mentioning the distinction between gas-poor and gas-rich environments. In particular, the latter possesses also a possible solution to the final parsec problem addressed before, since, by the interaction between the black hole and surrounding gas, additional angular momentum can be extracted from the binary (*Hayasaki, 2009 [54]*).

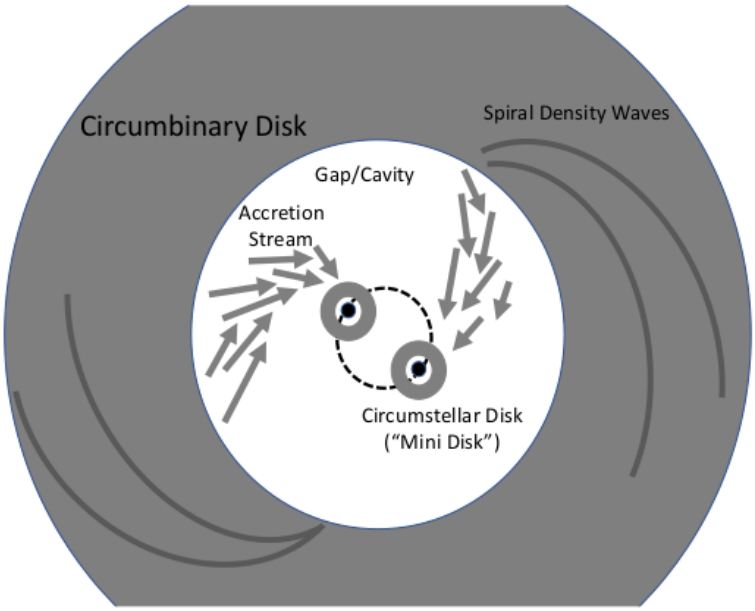

Figure 1.9: Explicative representation of pc/sub-pc Binary in the triple disk configuration. *Credit: Lai & Mũnoz, 2023 [74].*

The other peculiar feature of these gaseous systems is that the BH binary is surrounded by a self-gravitating circumbinary accretion disk (CBD), up to $\sim 100\,pc$. Along with the single mini-disk structures (called also circum-single disks or CSD) around each compact object,

the CBD creates the final triple disk configuration, depicted in Figure 1.9. The accretion disk on small scales is formed because of mass transfer, on a periodic occurrence at each orbit, from the circumbinary structure and is subsequently subjected to viscous evolution.
Between the circumbinary disk and the other two disks, because of the action of tidal torques exerted by the binary on the gas in the vicinity, the region becomes empty of matter, defining a gap or a cavity between the CBD and CSD. In the presence of the gap, it comes that the binary and circumbinary disks around are co-rotating, as expected from the evolution of gas-rich galaxy mergers (*Dotti et al., 2012 [32]*).
The dynamical evolution is then driven by the interaction between the large-scale gas distribution and the smaller ones, depending on the re-filling of material from the inner edge of the circumbinary disk toward the inward. Indeed, matter from CBD crosses the gap in narrow streams and can accrete in the mini-disks or can be sent back with subsequent shock on its original disk (*D'Ascoli et al., 2018 [25]*). The periodic streams of gas that fed the mini-disks show periodicity comparable to the binary period (*Serafinelli et al., 2020 [119]*).
This "triple disk interaction" is regulated by the binary mass ratio q (*De Rosa et al., 2019 [28]*). There are three main regimes: $q \ll 1$, $10^{-4} \leq q \leq 0.05$ and $0.1 \leq q \leq 1$ (the latter being the best case for SMBHB formation).
The evolution timescales depend ultimately on the compact object masses and their initial separation, along with the amount of available gas and stars in the merged galaxy.
Additional angular momentum is lost in the end because of Gravitational Waves (GW), that facilitates the coalescence, being the loss more efficient for more eccentric binaries (for GW treatment see section 1.7.3).

1.7.2 SMBHB emission

The presence of gas is a crucial ingredient not only for the accretion mechanism, but also in the detection of SMBH binaries. In the following section, a detailed analysis of the emission and possible detection techniques throughout the electromagnetic spectrum is presented, following the line of argument from *De Rosa et al. (2019) [28]*. For these compact systems, direct imaging is beyond the capability (i.e., angular resolution) of most of the current instruments, hence direct observations are still a challenging task, while indirect methods can be exploited for their detection (e.g. *Severgnini et al., 2022 [122]*). For this reason and given the extreme complexity of these systems, in order to understand formation mechanism and emission features, hydrodynamical simulations are essential.
The high-energy band is the most suitable to search for binaries of this kind, since it is less affected by obscuration and absorption by gas of the host galaxy and is the preferential one to look for nuclear emission in AGN, revealing the presence of a strong gravitational field.

1.7.2.1 Quest for Dual AGN

Several methods have been employed to search for Dual AGN: one of these considers follow-up observations of candidates, selected among large catalogs, wide-field surveys in the optical and deep field surveys like COSMOS and Chandra Deep Field North-South in X-rays, limited in size (i.e. COSMOS covers $2\,deg^2$ and CDFN-S covers $0.11\,deg^2$).

- **Optical Surveys**
  The SDSS (Sloan Digital Sky Survey) is a large and detailed astronomical survey, collecting data with a dedicated 2.5m optical telescope in New Mexico [8]. BOSS (Baryon Oscillation Spectroscopic Survey) is part of the SDSS-III data release and measures the scale of baryonic acoustic oscillations (BAO) in the early Universe by mapping the spatial distribution of luminous red galaxies (LRGs) and quasars [9]. These two surveys are the suitable ones to find Dual AGN candidates, along with the XDQSO photometric Quasar catalog, for brightest less obscured nuclei (*Bovy et al., 2011 [13]*). The optical surveys are limited because of instrumental issues, due to the fiber collision limit (the fiber size is $3''$ for SDSS and $2.5''$ for BOSS, with relative minimum separation for fibers of $55''$ and $62''$, respectively): just pairs, that not lie in a single fiber, at a minimum physical separation of $\sim$ 500 kpc at redshift $z \simeq 2$, can be detected. If the AGN cannot be spatially resolved, spectroscopy [10] can overcome the photometric limit: studying emission lines can reveal the presence of AGN binaries, for example in case of a double-peaked emission line profile in the optical spectra. The study from *Wang et al. (2009)* revealed that the [OIII] λ5007 line with a double-peaked profile is a promising signature of two orbiting narrow-line regions, an indicator of an ongoing merging process. Other forbidden high-ionization lines, like [NeV] λ3426 and [NeIII] λ3869 are employed, in particular for higher-redshift sources (e.g. *Barrows et al., 2013 [9]*). The double line profile is adopted in optical surveys under the hypothesis of two NLR, each one associated to the parent AGN in the double system. However, this is just the first imprint at dual AGN candidates, that requires further investigations and possible observational follow-ups, including eventually integral field spectroscopy (this is a powerful tool, in particular to separate cases in which the double-peaked profile is caused by a single AGN, which however can resemble the dual observational appearance, see e.g. study of *Fu et al., 2012 [45]*). The optical hunting is limited by stellar processes contamination, diluting and sometimes overcoming the AGN emission.

- **X-ray surveys**
  The first SMBH binary system was discovered using both Chandra X-ray imaging and spectroscopy, for which subsequent optical (VLT/MUSE) and radio (ALMA) follow

[8] SDSS link (*url:https://www.sdss.org/ [21]*)
[9] BOSS link (*url:https://www.sdss3.org/surveys/boss.php [20]*)
[10] The spectroscopic quest is limited just by the the spectral resolution of the instrument at work.

ups were performed: the source NGC 6240 shows the presence of two disentangled northern and southern nuclei, optically separated by 1.8″ corresponding to a physical distance of $\sim 1\,kpc$ (*Fried & Shulz, 1983 [44]*), where a neutral Kα Fe line is detected in both (*Komossa et al., 2003 [69]*). Direct imaging/spectroscopy of dual AGN are currently employed with present facilities, e.g. Chandra and XMM-Newton, even if low-photon statistics and worst angular resolution, respectively, are issues that prevent source identification. Neverthless, X-rays can be employed for dedicated follow-ups of previous dual AGN or for all-sky surveys, hence probing the entire FOV to reveal AGN pairs. We refer to the review by *De Rosa et al., 2019 [28]* for recent dual AGN discoveries with related studies. From the all sky hard X-Ray SWIFT/BAT survey, *Koss and collaborators* showed that close pairs with separation below $30\,kpc$ are more frequent within luminous AGN (*Koss et al., 2012 [71]*), in agreement with the suggestions from other studies where lower luminous AGN pairs were found at larger relative distances. Moreover, *Ricci et al., 2017 [114]* found that an higher fraction of heavily obscured AGN (i.e. $N_H > 10^{23} cm^{-2}$) is present in late mergers, for which the large obscuration cannot be associated with the torus structure. The link between the merger stage and the obscured AGN fraction (e.g. *Lanzuisi et al., 2018 [76]*) demonstrates how important is to carry out a multi-wavelength study of such sources. For what concern high-redshift (i.e. z>1) dual systems, they are more elusive, due to a combination of available facilities and to an eventually large system obscuration. In this regard, the study from *Vignali et al, 2018 [137]* identified three quasar pairs, one at z=3.0, another z=3.3, and the last at z=5, with physical separation between the SMBH in the pair of 43 kpc, 65 kpc and 136 kpc, respectively.

- **NIR-MIR surveys**
  Samples of mid-IR selected AGN are employed to search for possible Dual AGN candidates. The reprocessed emission from dust surrounding AGN can be identified as a mid-IR continuum, hence probing heavy extincted systems missing from optical selections. Candidate sources were selected among the WISE all sky survey mid-IR sample, the SDSS sample and LBT sample from pre-selected WISE advanced mergers. Unfortunately, probably due to the limited angular resolution of the available facilities and to the large obscuration, the candidate dual AGN should be further investigated with e.g. X-rays follow ups to probe first their nature as active nuclei and then the pair hypothesis. In this sense, the work from *Perna et al., 2023 [106]* took advantage of the JWST NIRSpec Integral Field Spectrograph (IFS) observations to look at the LBQS 0302-0019, a quasar at $z \sim 3.3$, ultra-dense environment. They unveiled the presence of a companion at ~ 20 kpc from the primary QSO, hence forming an AGN pair at high redshift.

- **Radio surveys**
  The radio emission from AGN originates near the compact source because of the interaction between high energetic electrons and magnetic field lines, subsequently launched at large distances in jets/outflows structures. VLA (Very Large Array), ATCA (Australia Telescope Compact Array) and eMERLIN (electronic Multi-Element Remotely-Linked Interferometre Network) facilities work well in resolving pairs angular scales. They are also able to enlight possible radio jets and outflows. Exploiting *cm* observations with the VLBI network, dual AGN, at a spatial projected separation of a pc or so (in the local Universe) and $\sim 10\,pc$ away (at any redshift) are resolved [11], whenever each source can be defined as a radio AGN (further details in *De Rosa et al., 2019 [28]* and references therein).

1.7.2.2 Quest for Binary AGN

When the pairs is defined as binary, the two SMBH are gravitationally bound and in a Keplerian binary. They are found at pc/sub-pc separation: this is the reason why all candidates detected so far were so challenging to be found. A theoretical approach, inclusive of hydrodynamical simulations, is the right path to investigate these systems, in order to study their formation and evolution (fundamentals on binary systems given in sec. 1.7.1). From an observational point of view, direct imaging, spectroscopy and photometry have been employed.

- **Radio Imaging**
  Exploiting VLBI observations, even in case of low-resolution data, harder binary systems can be detected, at least in local Universe and for pc separations. Indeed, the presence of pairs of relativistic jets, possibly perturbed periodically by the binary interaction, can be resolved thanks to the angular resolution provided by the interferometric technique.

- **Spectroscopic surveys: broad emission-line profile**
  If the disk scenario is correct, the BLR and NLR can be investigated in order to enlight possible features suggesting the nature of the binary system due to its orbital motion. Up to 0.01 pc separation, the two BLR are distinct and detectable, producing double emission line profile. When two BHs are at close separation such that the individual BLRs are already settled in equilibrium, the BLR appears observationally as a single one. In X-rays, the double-line profile can arise from the mini-disks around each BH (see futher characterization of MCG+11-11-032, the source under investigation, in the following chapters), each one producing its Fe Kα line (e.g. *Popović et al., 2012 [109]*).

[11] VLBI can achieve milli-arcsec resolution at cm-wavelengths.

- **Photometric surveys**
  The expected luminosities from simulations are quasar-like luminosities, so Quasars that exhibit photometric variability can be a good starting point. In addition, the presence of periodic streams of gas, from the circumbinary disk toward the mini-disks, generates a peculiar feature to look for in these systems. However, determining the periodic variability of quasars is not so simple, since the stochastic nature of the source may interfere.

1.7.3 Gravitational Wave emission

In this context, Gravitational Waves (GWs) represent a unique tool to investigate SMBHB emission, since their detection reveals the presence of a binary system with high significance, rather then depicting a simple candidate source (*De Rosa et al., 2019 [28]*). Gravitational Waves are ripples in space-time framework, detectable at different frequency ranges depending on the astrophysical source properties and according to the available facilities. Among all the emitters, compact binary coalescences are the most powerful ones (first detection GW150914, *Abbott et al., 2016 [1]*). Since the frequency of the GW signal scales as:

$$f_{GW}(\tau) = \frac{1}{8\pi}\left(\frac{5}{\tau}\right)^{\frac{3}{8}}\left(\frac{GM_C}{c^3}\right)^{-\frac{5}{8}} \tag{1.8}$$

where τ is defined as the time to coalescence, being $\tau = 0$ at the merger of the two objects, M_C the Chirp mass, defined as $M_c = \mu^{\frac{3}{5}} m_{tot}^{\frac{2}{5}}$, with μ the reduced mass ($\mu = \frac{m_1 m_2}{m_1+m_2}$) and $m_{tot} = m_1 + m_2$ the total mass of the system (*Maggiore, 2007 [89]*). As τ tends to 0, hence as the system approaches to coalescence, the frequency of the observed signal increases up to a divergence; in parallel, at larger masses of the compact objects, a lower frequency of the signal is expected (in the mHz/nHz domain). The amplitude of the GW signal is defined as:

$$h_+ = \frac{4}{r}\left(\frac{GM_c}{c^2}\right)^{\frac{5}{3}}\left(\frac{\pi f_{GW}}{c}\right)^{\frac{2}{3}}\left(\frac{1+\cos i^2}{2}\right)\cos\phi \tag{1.9}$$

where i is the inclination with respect to the perpendicular to the orbital plane of the binary and ϕ is the GW phase.
If the expansion of the Universe is taken into account, sources placed at cosmological distance produce a signal like 1.9, with the redshift-dependent chirp mass $\mathcal{M}_c = (1+z)M_c$ in place of M_c and the luminosity distance d_L in place of the simple r parameter. The variation in time is described as:

$$\dot{f_{GW}} = \frac{96}{5}\pi^{\frac{3}{8}}\left(\frac{GM_C}{c^3}\right)^{-\frac{5}{3}} f^{\frac{11}{3}} \tag{1.10}$$

As mentioned in the description of the merger phases, when the binary hardens, GW dominates the loss of energy and allows the binary to approach the coalescence: this happens when two objects are placed at small separation, of the order of $10^{-3}\,pc$ (e.g. *Colpi & Sesana,*

2017 [23]).

Figure 1.10 shows the strain amplitude of the GW signal as a function of frequency, from nanoHz up to tens of kHz, with the sensitivity of different current and future GW observatories and techniques (Advanced LIGO (aLIGO), Virgo, Evolved LISA (eLISA), International PTA (IPTA) and SKA).
Between 100 μHz and 100 mHz, space-based facilities and eLISA (Laser Interferometer Space Antenna) for the near future, will probe the *low-frequency Universe*: LISA will take advanced of space distances and allows the detection of compact sources with a mass of the order of $10^4 - 10^7 M_{sun}$, with mass ratio $0.1 < q < 1$ and at coalescence redshifts ranging from $z \sim 20$ to the present. In addition, other LISA targets will be the compact binaries in the inspiral phase, like NS-NS binaries or stellar BH-BH ones, and stochastic gravitational waves associated with a background signal from primordial Universe. If LISA source localization of the order of arcsec precision is achieved, follow-up observations would provide multi-wavelength coverage of candidate sources. As a result, the study of the binary surroundings will provide additional constrains on the binary periodicity and spectral evolution (e.g. *Tang et al., 2018 [132]*).

While the *very low-frequency Universe* (i.e. $10^{-9} - 10^{-7} Hz$) will be investigated thanks to PTA technique: the signal from a millisecond pulsar represents a stable clock in the Universe and, since GWs fluctuations create perturbation in the space-time metric, this signal at a radio observatory, from spatially separated pulsars, is shifted in time. In this case, the perturbations are supposed to originate from supermassive black hole binaries, with $10^8 - 10^9 M_{sun}$, creating a collective background that affects the pulsar signal. The Astrophysical GW Background is defined as a broadband signal with peculiar spectral shape, extending from the high-frequency band covered by the Ligo-Virgo-Kagra detectors to the mHz band covered by future detectors like LISA (e.g. *Staelens & Nelemans, 2023 [130]*).
Different research groups [12] around the world have recently published few articles concerning the study of fifteen years of observations of millisecond pulsars in the Milky Way. These studies can be exploited to look for the presence of a low-frequency gravitational-wave background (GWB) (*Jenet et al., 2005 [60]*), whose origin is still under debate. Assuming a SMBH binary population distributed across the Universe, the GWB would be the result of the superposition of many unresolved binaries of massive entities (*Agazie et al., 2023 [2]*). *Agazie's group* found SMBH binary population models able to reproduce both the amplitude and shape of the observed low-frequency gravitational-wave spectrum. In this context, PTAs are able to identify source localization within tens of square degrees thanks to triangulation technique and, in this sense, allow follow-up electromagnetic observations of the region, in particular tracing the possible periodic signal associated to CBD of a SMBH binary (*Colpi & Sesana, 2017 [23]*).

[12]The collaboration involves the NANOGrav, EPTA-European Pulsar Timing Array- with InPTA- Indian Pulsar Timing Array-, PPTA-Parkes Pulsar Timing Array- and CPTA-Chinese Pulsar Timing Array-.

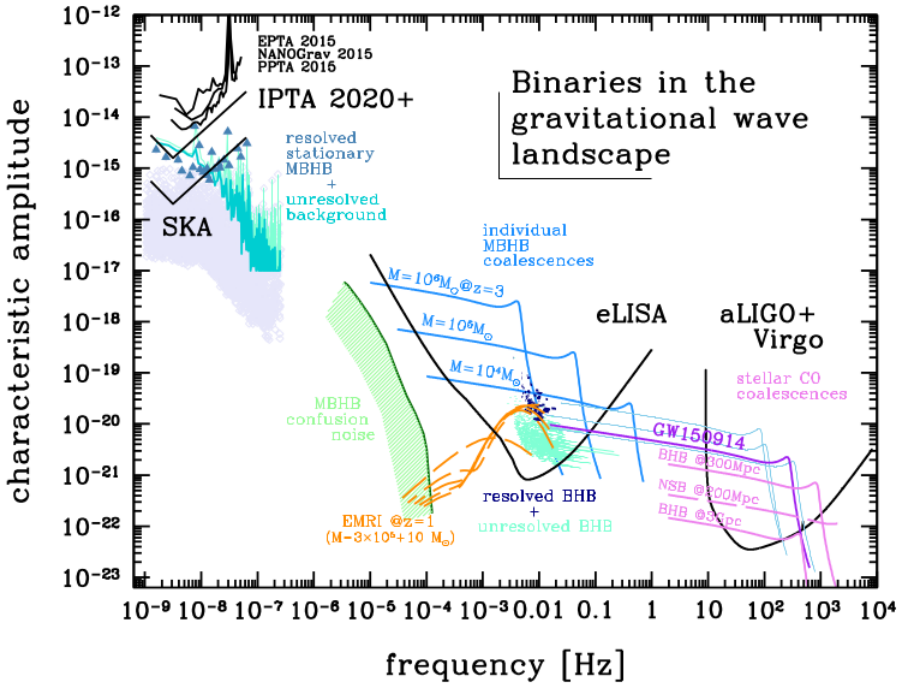

Figure 1.10: Amplitude of the Gravitational Wave signal at different frequency domains. The sensitivity of present and future GW facilities is placed, from right to left: Advanced LIGO and Virgo are targeting stellar compact object coalescence and neutron star merger, LISA is targeting SMBH binaries and BHB both resolved and not resolved and PTA and radio SKA survey for unresolved background signal from SMBHB and primordial Universe. *Credit: Colpi & Sesana, 2017 [23].*

CHAPTER 2

How X-ray telescopes work

In the case of high-energy band (X- and γ-ray ranges), space telescope are needed to collect emission from astrophysical objects.
The best instrument, used to perform an observation, is chosen according to the specific scientific mission, defined by the combination of optics, effective collecting area, temporal resolution, energy resolution, field of view (FOV). Depending on the photon energies, there are different types of high-energy telescopes: collimators, grazing incidence mirrors, coded masks, Compton telescopes and Pair production telescopes. In particular, in the case of focusing systems, the X-rays photons are collected and focused. These systems allow to achieve better angular resolution and detect faint/weak sources.

2.1 Grazing Incidence Technique

The optical system, used for telescopes in the visible/UV band, is not suitable for X-ray photons: for these photons the energies are higher than the binding energy of the atomic electrons and the refracting index of the mirror is less than 1. In order to reflect X-ray photons, it is necessary that they hit the mirror surface below a given angle, defined as *grazing incidence angle*, with the following dependence [1]:

$$\Theta \propto \frac{\sqrt{\rho}}{E_{ph}} \tag{2.1}$$

where ρ is the density of the coating layer and E_{ph} is the energy of the incoming photon. Therefore high-Z [2] materials on the mirror surface, like gold, platinum and iridium, give a better performance in terms of reflectivity, but at the same time they are subject to photo-electric absorption phenomena and the presence of absorption edges.
In addition, the smoothness of the surface plays an important role: the roughness of the mirror needs to be very small to ensure good reflectivity.

[1] According to Snell's Law, total external reflection is possible for X-ray photons whenever $cosin\theta = n$, where θ is the angle between the arrival direction of the photon and the mirror surface and n the complex index of refraction.

[2] In this case, Z stands for the atomic number of the material.

2.2 Wolter Type Mirror

Wolter Type mirrors are a combination of parabolic and hyperbolic optics. Using a parabolic mirror, it is possible to collect all on-axis photons to the focal point. The main issue is that it suffers from optical aberrations; including also a hyperbolic mirror, the off-axis photon aberration can be overcome. In addition, it helps in reducing the focal length of X-ray telescope, otherwise extremely large [3]. Another important advantage of this configuration (in Figure 2.1) is that these mirrors can be nested, increasing significantly the collecting area of the telescope.

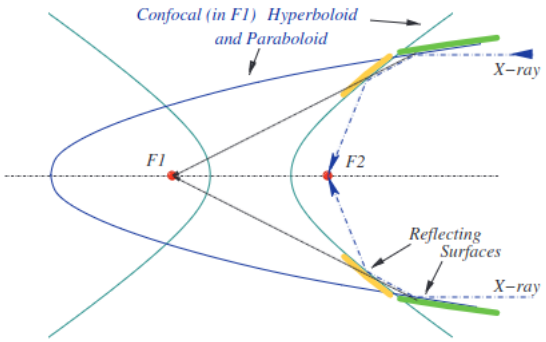

Figure 2.1: Wolter type I mirror configuration, made of a hyperbolic and a parabolic mirror surface, stuck properly. The path of an incident X-ray photon is shown with a dotted line. *Credit: Pareschi et al., 2023 [104].*

There are also other two types of Wolter mirrors, *Wolter type II* and *Wolter type III*, but just *Wolter type I* is used for X-ray science since the other two have larger focal lengths.
In case of an X-ray telescope, the effective collecting area is defined as:

$$A_{eff}(E, \Theta, x, y) = A_{geom} \cdot R(E) \cdot V(E, \Theta) \cdot QE(E, x, y) \tag{2.2}$$

where the functional dependences are in terms of E, the energy of the incoming photon, Θ, the distance with respect to the optical axis, x and y the position on the detector, while A_{geom} is the geometric area of the telescope, R is the reflectivity term (the fraction of photons that are reflected by the mirror), V term is the vignetting (the fraction of photons lost as a function of their energy and position with respect to the optical axis) and QE term is the quantum efficiency (the fraction of photons registered by the detector).
In X-ray data analysis, this information is contained in a file called Ancillary Response File, or ARF, exploiting the shape of the effective collecting area (the effective area performance as function of photon energy is shown in Figure 2.2, in logarithmic scale).

[3] The focal length in these systems is defined by the distance between the intersection of paraboloid and hyperboloid mirror shell and the focal point. It can be computed in the following way $F = \frac{R}{tan(4\Theta)}$, with R the mirror reflectivity.

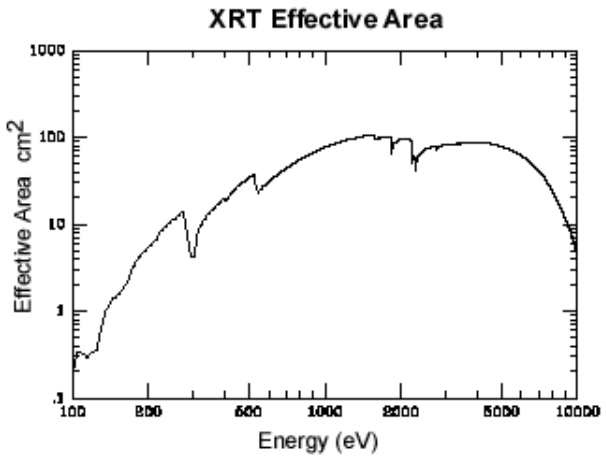

Figure 2.2: Example of the Effective Area curve of Swift X-Ray Telescope as a function of the energy of the incoming photon. *Credit: Nasa [98].*

2.3 The Angular Resolution: The PSF

The *PSF*, or Point Spread Function, represents how point-like source photons are spread on the detector plane (an illustrative PSF is shown in Figure 2.3) and is linked with the concept of angular resolution of a telescope. The angular resolution is defined as the minimum angular separation between nearby objects that can be distinguished by the telescope detector.

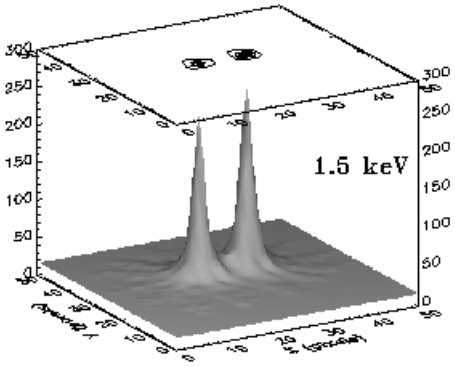

Figure 2.3: PSF illustrative example, with relative image dispersion. *Credit: PennState, Mission Operation Center for Swift [105].*

In the case of an X-ray telescope, the PSF depends on the energy of the incoming photon, the off-axis angle and on the position in the FOV. The shape can be modelled or approximated using a Gaussian function. The angular resolution is quantified through the Full Width at Half Maximum (FWHM), defining the PSF profile width at half the profile height or, equivalently, the Half Energy Width (HEW), as the diameter that contains 50% of the total flux.

For the Swft telescope - whose data have been used in this master thesis work - the chosen

model is the following function:

$$PSF = W \cdot e^{-\frac{r^2}{2\sigma^2}} + (1 - W)\left(1 + \left(\frac{r}{r_c}\right)^2\right)^{-\beta} \tag{2.3}$$

characterized by a central Gaussian profile and a King model for the wings shape, with W, r_c, σ and β functions of energy and position on the detector (*Moretti et al., 2004 [93]*).

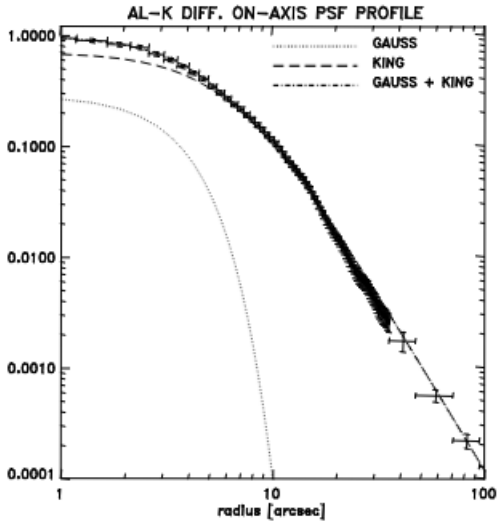

Figure 2.4: Example of the on-axis PSF of the Swift X-Ray Telescope, modelled as a Gaussian plus a King profile. *Credit: Moretti et al., 2004 [93].*

The EEF (Encircled Energy Fraction) is a useful parameter used often to define telescope angular resolution, since it represents the radial integration of the PSF, defining the fraction of photons contained within a certain angular radius.

2.4 The Spectral Resolution

The spectral resolution of a telescope can be defined as the capability to distinguish features in the spectrum placed at tight energy separation. In an X-ray telescope, the energy resolution ΔE is expressed as $\frac{\Delta E}{E} \propto E^{-\frac{1}{2}}$, where E is the incident photon energy and the energies are expressed in keV. The analogous $\frac{E}{\Delta E}$ ratio defines the resolving power of the telescope. In case of CCD detectors, the spectral resolution is usually of the order of $\sim 100 - 150\, eV$ at 6 keV. In case of the XRT CCD camera on board of the Swift satellite, the pre-launch resolution was 135 eV at 5.9 keV, subsequently it degrades because of radiation damage.

2.5 The Swift Telescope

SWIFT is a multi-wavelength observatory launched with success in November 2004 and has been operating since then. The satellite is located in a low-Earth orbit and is part of the NASA's Medium Explorer (MIDEX) program (*Credit:Swift Fact Sheet [99]*).

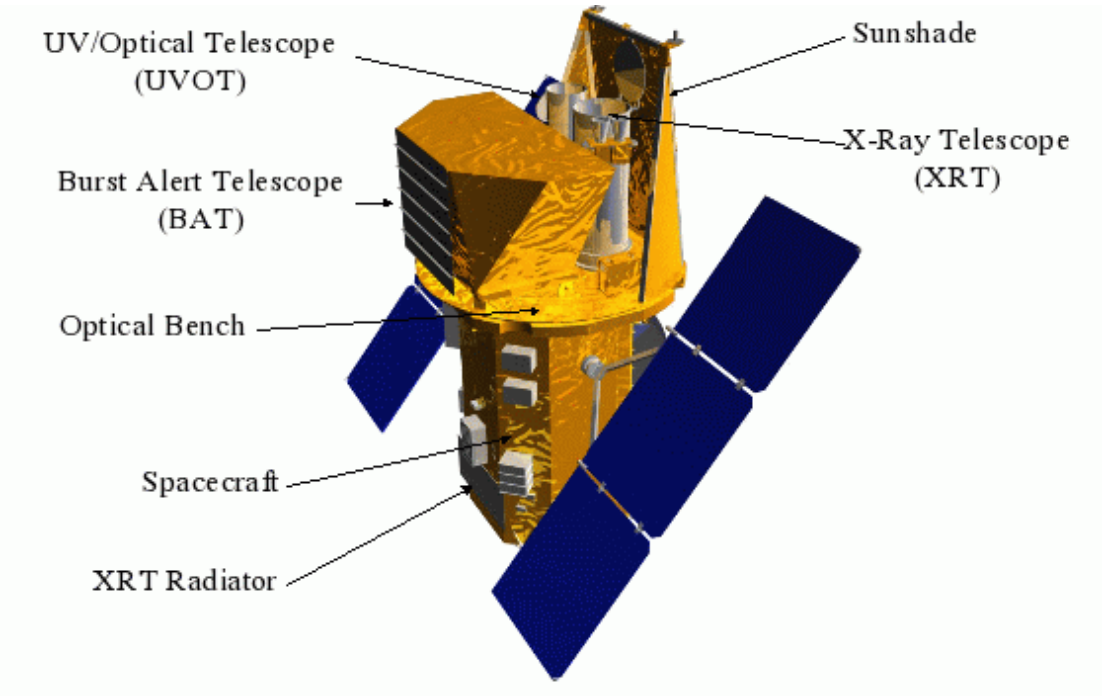

Figure 2.5: Swift telescope and instruments. *Credit: University of Leicester [79].*

2.5.1 Swift science

Swift is a rapid-response multi-wavelength facility which means it is ideal for observations of transient and variable sources. The main goal of the mission is to study Gamma Ray Bursts (GRBs) events, in order to determine their origin, their classification, to use them to investigate early Universe up to z>10 and to allow studies on the ultra-relativistic outflows, evolution and impact on the ambient medium. In addition to the primary objectives of GRB science, the satellite performed the first high-sensitive hard X-ray sky survey, making possible also challenging non-GRB science. Indeed, it is used as a general gamma-ray/X-ray/optical telescope, performing rapid "target of opportunity" observations of many transient phenomena.

2.5.2 Instruments onboard of Swift satellite

On the optical bench, three instruments [4] are allocated:

- *BAT* (Burst Alert Telescope) [15-150 keV] :
  It is a 2D coded-aperture mask made to detect hard X-ray sources (among which, GRBs), whenever it reveals an excess in the detector count rate compared to the background level. It works in the 15-150 keV energy range and the FOV is 1.4 steradian. Its FOV includes the FOV of the other two instruments, allowing a simultaneous study of the burst in the X-ray/UV energy band. BAT performs an all-sky hard X-ray survey and looks forward to X-ray transients performing a continous monitoring as it awaits for new GRB trigger. Its energy resolution is defined according to the ratio $\frac{\Delta E}{E} = 5\%$ for CZT (Cadmium Zinc Telluride) detectors. The instrument PSF is $< 20'$.

- *XRT* (X-Ray Telescope) [0.2-10 keV]:
  According to the focusing X-ray photons technique via Wolter-I type mirror, XRT produces accurate flux measurements, spectra and high time resolution light curves. It is made of twelve co-axial and co-focal mirror shells. It is characterized by a $23'$ x $23'$ FOV and works in the 0.2-10 keV energy range, with a telescope on-axis PSF of $18''$ at $\sim$ 1.5 keV and of $22''$ at 8.1 keV. The CCD detector has an energy resolution that varies from $\sim$ 190 eV at 10 keV down to $\sim$ 50 eV at 0.1 keV, being then at 6 keV $\sim$ 140 eV. The resolution will degrade during the mission, but it will remain below 200 eV at the end of the mission life for a worst-case environment. According to its primary scope (i.e. studying afterglow emission), XRT is used to perform long-term monitoring.
  The telescope has three different readout/processing modes:

  1. **Imaging Mode** | The CCD operates like a normal optical CCD. The result is an integrated image, allowing also pile-up of the source. It does not allow spectroscopy and is used only for bright sources.
  2. **Windowed Timing Mode** | This mode is used for fluxes below 50 Crabs [5] and has no pile-up for fluxes below 600 mCrabs. It allows for high-time resolution (2.2 ms) and bright source spectroscopy.
  3. **Photon-counting Mode** | At very low fluxes (from $2{\cdot}10^{-14}$ to $2{\cdot}10^{-11}\, erg\, cm^{-2}\, s^{-1}$), this mode works for full spectral and spatial information, with a time resolution of 2.5 s.

[4] Credit for instruments description: *Asi [118]*

[5] The Crab Nebula has been used as a standard candle for the calibration of X-ray telescopes and as an absolute flux scale to measure the flux of astrophysical sources in most space-based facilities. It has been one of the brightest sources in X-ray/γ-ray energy band, with stable intensity profile making it suitable to be used as units of measurement (*Wilson et al., 2011 [143]*). In the 2-10 keV range, $1\, Crab = 2.4\, 10^{-8} erg\, cm^{-2}\, s^{-1}$.

There was also a fourth Readout Mode, **Photodiode Mode**, able to produce high speed light curves with a time resolution of 0.14 ms, providing accurate timing information for very bright sources, but it was disabled.

- *UVOT* (Ultraviolet/Optical Telescope) [170-600 nm]:
  It is a modified Ritchey-Chretien UV/optical telescope, co-aligned with the X-ray Telescope, and carries 11-position filter wheels, among which low-resolution grism spectra of bright GRBs, magnification and broad-band UV/visible photometry can be performed. The two detectors are photon-counting instruments and the system allows for two different data collection modes, an event and imaging one.

The present thesis work will make use of archival data and dedicated monitoring (log-term X-ray monitoring, started in 2015, renewed for 2022 and still ongoing at the writing date of this thesis-November 2023) of the source MCG+11-11-032. The data are collected using the XRT instrument in the PC-mode. In order to study the variability properties of the source, the Swift-BAT all-sky monitoring is also taken into consideration, looking at the 105-months and 123-months BAT light curve (previous works *Severgnini et al., 2018 [123]*, *Serafinelli et al., 2020 [119]*).

CHAPTER 3

The source: MCG+11-11-032

MCG+11-11-032 is a local radio-quiet Seyfert 2 galaxy at $z \sim 0.0362$ (mass derived from the CO velocity dispersion, $log\left(\frac{M}{M_{sun}}\right) = 8.66 \pm 0.30$, *Lamperti et al., 2017 [75]*). In the following sections, I will present the source under investigation in this project, as studied in *Wang and collaborators*' optical analysis ([140]), *Severgnini and collaborators*' optical and X-ray analysis ([123], [122]) and *Serafinelli and collaborators*' variability analysis ([119]).

3.1 Optical selection

Wang et al. (2009) analysed a sample of 87 type 2 AGN selected from the SDSS-DR7 survey and showing double-peaked [OIII] λ 5007 Å emission lines. Details about the double-peaked AGN selection from *Wang et al.* work are briefly summarized below:

- According to the BPT diagram, all the AGN were identified in the catalog;
- among them, type 2 AGN are selected according to the following criteria related to line ratios, $log\left(\frac{[OIII]}{H\beta}\right) > 0.61/\left[log\left([NII]/H\alpha\right) - 0.47\right] + 1.19$ or $log\left(\frac{[NII]}{H\alpha}\right) > 0.47$;
- the additional criteria adopted were: r magnitude < 17.7, $z \leq 0.15$ [1] and $EW_{[OIII]} > 55\,$Å;
- they selected sources with a line shift between the two [OIII] components of $\Delta\lambda > 1\,$Å and flux ratio in the $[0.1, 10]$ range.

According to the line profile, typically one component results blue-shifted and the other red-shifted with respect to the systemic velocity of the host galaxy. Because of this line-profile characterization, AGN selected in the catalog are proposed as putative dual AGN. The line shift can be attributed to the orbital rotation of two AGN around common centre of mass, causing an emission line at rest wavelength λ_0 to split into a red and blue components. As for MCG+11-11-032, almost all the most prominent optical emission lines (Hβ, [OIII], Hα,...)

[1] Being obscured systems, they were able to determine the redshift of the host galaxies using stellar absorption lines.

show double-peaked profiles.

Another validation of the dual AGN scenario is the strong correlation between the line shifts $\Delta\lambda = \lambda_i - \lambda_0$, being λ_i the wavelength of the blue and red components with respect to the reference one λ_0, and the relative line luminosities. From Kepler's law applied to a binary system in circular orbit and with conserved angular momentum, $\frac{M_2}{M_1} = \frac{V_1}{V_2}$, where V_1,V_2 are the orbital velocities and $\frac{V_1}{V_2} = \frac{\Delta\lambda_1}{\Delta\lambda_2}$. From the M-L relation $\frac{M_{BH,2}}{M_{BH,1}} = \frac{L_{[OIII],2}}{L_{[OIII],1}}$ (where, according to the Magorrian relation, $M_{BH,1} \propto M_1$, as for $M_{BH,2}$), hence by concatenating the above relations they found $\frac{L_{[OIII],1}}{L_{[OIII],2}} \propto \left(\frac{\Delta\lambda_1}{\Delta\lambda_2}\right)$. The advantage of this linear relation is that both parameters can be extracted from the observed spectrum, without any assumption on the inclination of the system.

Emission from bi-polar outflows or accretion disk are alternative explanations for double-line profiles (e.g. *Eracleous & Halpern, 2003 [33]*). The disk/jet outflows hypothesis was discarded by *Wang et al. (2009) [140]*, because the associated luminosity-(line-shift) correlation would be tighter (like $\frac{L_{line1}}{L_{line2}} \propto \left(\frac{\Delta\lambda_1}{\Delta\lambda_2}\right)^3$), compared instead to the one found by their analysis. In the end, the conclusion, at which they came, involves the emission from two orbiting NLR during the merger process.

Severgnini et al. (2018) [123] carried out the same optical analysis for MCG+11-11-032, exploiting the SDSS-DR13 spectrum.

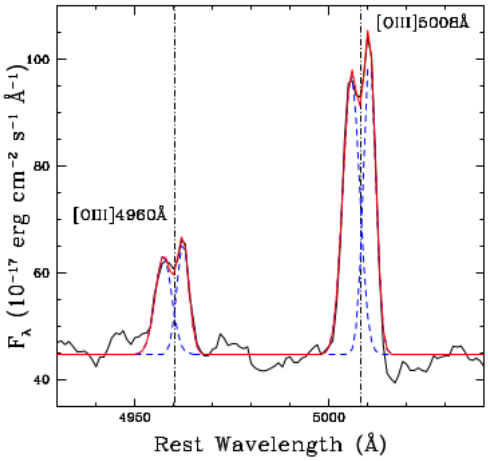

Figure 3.1: Example of MCG+11-11-032 rest frame spectrum around [OIII] lines. Red solid line and dashed blue lines represent the best fit model and the single Gaussian components, respectively. Vertical lines corresponding to the wavelength of the lines at a systemic velocity of the host galaxy are depicted. *Credit: Severgnini et al., 2018 [123].*

The overall adopted model for the optical spectrum is made of a power-law continuum and two narrow Gaussian components for all the prominent emission lines, leaving free to vary the peaks, the width and the normalization of the two lines ([OIII] is shown in Figure 3.1): the width of the blue component is set independently on the width of the red one, being this one smaller, and the associated velocity offset of the optical transitions is consistent over the spectrum. Exploiting the third Kepler's law, once the orbital period estimation was derived, *Serafinelli et al.* (2020) [119] inferred a sub-pc separation for this source, i.e.

$a = (6.5 \pm 1.5) \times 10^{-3}\, pc$.
Giving the small inferred orbital separation, the double peaked profile of the emission lines can arise from the motion of a single NLR surrounding the pair.

3.2 X-ray modelling

Severgnini et al. (2018) (*S18* hereafter) performed a set of variability studies, exploiting the X-ray modelling of Swift spectra, using XRT instrument in PC-mode. The observational campaign started on December 2015 and ended on February 2016, with a total of 26 proprietary datasets (for a total of $\sim 166\, ks$), one excluded because not completed. In the analysis, they included also six previous archival observations and one immediately after their campaign.
The study, based on XRT data product extracted from the online tool, consisted of the analysis of the images, spectra and light curves. The observed 0.3-10 keV spectra are divided according to the intensity state of the source: they enlighted two distinct count rate states, a high level ($\sim 0.03\, counts\, s^{-1}$), with the associated spectrum of ~ 4170 net counts, and a low one ($\sim 0.01\, counts\, s^{-1}$), with ~ 100 net counts. The results, outlined here, correspond to the analysis of the high-state spectrum.

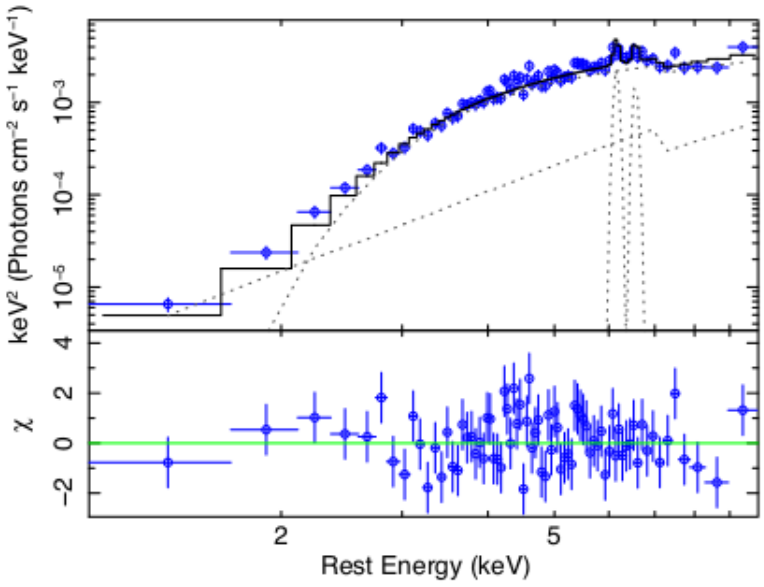

Figure 3.2: In the upper panel, MCG+11-11-032 unfolded spectrum (blue dots), in units of number of photons per unit area, time and energy, and best-fit model (model components in dotted lines). In the lower panel, the residuals of the fit are reported in terms of χ deviation ($\chi = \frac{data-model}{error}$). *Credit: Severgnini et al., 2018 [123].*

The model components will be explained in Section 5.2. The results of this analysis are not presented here in details, since they constitute the starting point for my project work. Briefly, a single narrow emission line is considered in order to fit the residuals around $6 - 7\, keV$ and

is found at $6.18 \pm 0.09\,keV$, with significance of $\sim 2\sigma$. From the line energy vs normalization contour plot, another line component was emerging. The double-line profile found by *S18* is characterized by two emission lines, one at $E = 6.16 \pm 0.08\,keV$ (which is not easily associated to any expected transition) and the other at $E = 6.56 \pm 0.16\,keV$, with significance of $\sim 1.3\sigma$. One possible explanation is that the single disk surrounding each SMBH in the binary produces a fluorescent line (i.e. Fe Kα). The model with two lines is shown in Figure 3.2. From the rest-frame line peaks, the energy shift is $\Delta v = 0.06c$, assuming the system to be seen edge on. Indeed, the source is obscured at some level (see X-ray modelling of Chp. 5 for the estimation of the obscuration level through the n_H parameter), not only because of the AGN intrinsic obscuration but also because of the binary small and big substructures (e.g. the CBD), if these systems are aligned along the line of sight.
The study of the 123-months BAT light curve suggests a periodic variability in the source 15-150 keV emission, with estimated period of ~ 25 months by looking at the peaks in the count rate variation.
On smaller timescales, the XRT light curve shows a variability pattern in agreement with the previous estimation. On the basis of the X-ray colors [2], the X-ray source variability is interpreted as an intrinsic variation in the source flux, rather than a varying absorption along the line of sight.

The modular behaviour of the source flux may represent a supportive signature of the source binary nature: the source variability may be linked to the modulation of the orbital period due the circumbinary mass accretion rate (i.e. periodic fed by streams of gas from the circumbinary to the mini-disks) or to relativistic Doppler-boosting of the single mini-disk emission, with same correspondence between variability timescale and orbital period (*S18* [123]). Under these assumptions, the double emission-line profile could be associated with the motion of a single NLR, discussed in Sec. 3.1.

In *Serafinelli et al.* (2020), the source variability is investigated through the phase folding of the hard X-ray light curve, both on the 105 Month Swift-BAT and 123 Month Swift-BAT light curves (Figure 3.3). The epoch folding procedure consists on a timing analysis of the data, choosing a range in period and folding the data to that period. The phase is referred to the difference of the folded data compared to the assumed period. The resulting epoch folding light curve shows a possible source trend, e.g. an epoch folding flat light curve demonstrates that the source seems not to vary according to the chosen period. The epoch folding is a way to estimate periodicities in a time-dependent data (e.g. *Leahy et al., 1983 [77]* for epoch folding application).
Serafinelli confirmed a periodic behaviour, consistent with the period previously obtained from 123-m BAT light curve (*S18*), with a constant level flux model rejected at 99.95% confidence level.

[2]Here the term X-ray colors is meant as the 4-10 keV to 2-4 keV flux ratio, which provides a first-order indication of the shape of the spectrum.

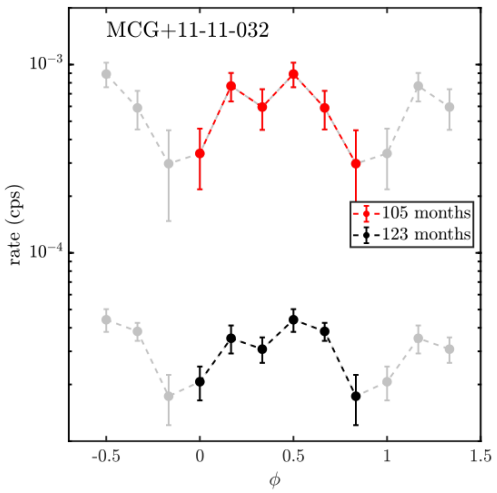

Figure 3.3: Phase folding of MCG+11-11-032 BAT light curve into six phase bins. The 105-m BAT ligth curve phase folding is shown in red in the upper curve, while the 123-m BAT light curve is shown with black points in the lower curve. *Credit: Serafinelli et al., 2020 [119].*

From the estimated period $P_0 \sim 25$ months, *Serafinelli et al.* (2020) derived the hypothetical sub-pc separation between the two compact objects and the orbital velocity, consistent with the rest-frame line energy shift. Under the assumption of an equal mass binary, i.e. $q = 1$, knowing the total mass M and the semi-major axis a of the binary, the time to coalesce is estimated $\tau = \frac{5}{256}\frac{c^5(1+q)^2a^4}{G^3M^3q} \sim 3.3 \cdot 10^4$ yrs (*Severgnini et al., 2022 [122]*).
In the end, MCG+11-11-032 can be considered a promising SMBH binary candidate for two main reasons:

- From the X-ray spectra modelling, a double-peaked iron line profile, not found at the rest frame energy of 6.4 keV expected from neutral Fe line emission, suggests the origin of each line to be a single accretion disk, enveloping a compact massive source, like a SMBH. The energy shift corresponds to a velocity offset of $\Delta v = 0.06c$.

- From the 123-BAT light curve, the best-fit period of the variability of the source is $\sim 25-26$ months. If the mini-disks scenario is adopted, this corresponds to the orbital period of the two disk structures. The orbital velocity measured is $(0.06 \pm 0.02)c$, in agreement with the other estimation.

Additional observing time is obtained by *Severgnini* and collaborators for the years 2022-2023, in order to continue the Swift-XRT monitoring and possibly confirm the nature of the source as a double system, providing double-peaked emission lines modelling and variability studies.

CHAPTER 4

X-ray datasets: reduction and analysis

The nature of MCG+11-11-032 is still uncertain and can be further investigated, thanks to additional observations obtained for the source in the period 2022 and 2023 using the Swift satellite. My thesis project consists of the reduction, analysis and X-ray modelling of all the datasets collected so far. I have exploited different data grouping and spectral binning with the aim of confirming or discarding the possible presence of double and/or variable Fe emission lines and a possible periodic behaviour, thus providing constraints on the source nature.

In the following paragraph, the reduction of all the available XRT datasets is presented. The X-ray monitoring provides few data points before 2015, a weekly but mostly daily monitoring in 2015 and 2016, and a monthly monitoring in 2022 and 2023, up to the observations obtained in September 2023 (see Table 4.1).

4.1 Manual Data Reduction

The datasets are obtained from the ASI (Agenzia Spaziale Italiana)-Space Science Data Center website. The analysed datasets are 66 exposures, comprehensive of the past and current monitoring, for a total of $\sim 330\,ks$, collected with the XRT instrument. Among the downloaded files, the "auxil" and "xrt" folders are those containing the interested files (e.g. event files, evt). The analysis is made on the dataset characterized by an XRT exposure time longer than 400 s (i.e. the dataset corresponding to the observational ID 00084954003, 00084954004, 00084954006, 00084954007 are excluded). The data reprocessing is carried out manually, according to the xrtpipeline procedure. The downloaded FITS files are named with the following convention: *sw-[ObsID]-<mode><window><type>_uf.evt* for the Level 1 files (raw event and image files) and *sw-[ObsID]-<mode><window><type>_cl.evt* for the Level 2 files (obtained from the Level 1 correcting for bias and bad pixel, for example). <mode> refers to the instrument operating modes ("pc"), <window> refers to the window setting of CCD ("w3" meaning 600 × 600 pixels) and <type> refers to the mode through which the satellites acquired data.
All the Swift FITS files have the same structure: the primary header contains the general

information about the mission, the instrument and the "ObsID"; the events files store photons information, like time, position and energy; the GTI (Good Time Interval) files contain the time interval of good data; the BPT (Bad Pixel Table) flags the position of pixels or columns that performed badly (dead, hot or flickering pixels). The files are dived into primary header, with the general information as before, and image files, whose number depend on the number of exposures, typically one image per exposure.

The Level 1 files are obtained automatically through a task that converts telemetry data[1] into FITS files. They are the product of Stage 1 data reduction in order to generate cleaned event files (i.e. calibrated in the end for bad pixels or bad columns, coordinates transformation, elimination of pile-up frames). Performing a standard screening process adopting different criteria, Level 1 files transform into Level 2 files, with event ones possibly ready for XSELECT environment and for image and spectra extraction.
Calibration data are obtained through CALDB, the High Energy Astrophysics Science Archive Research Center (HEASARC) Calibration Database.
Following the data analysis procedure reported on the SWIFT/XRT website [80], two main tasks are implemented.

xrtpipeline is a task used to process Level 1 files and generate cleaned event ones.

xselect is an interface extractor to generate images, light curves and spectra. Once the cleaned evt file is inserted as input, the images are produced via "extract image" command line and the information about the total and good counts and count rate of all the field of view are displayed. The source spectrum is extracted from a circular region of radius between 17″ and 24″ centered on the target [2], depending upon the source emission and the intensity distribution; the background spectrum is extracted from a larger (110″ - 130″ of radius) source-free circular region (far from the interested source but close enough to be representative of the background level at the source position, see Fig. 4.1). The spectrum extraction (command line "extract spectrum") is performed with the grade [3] filter applied (for the PC mode grades in the range 0-12 have been considered).

While the RMF matrix is obtained from CALDB, the ARF matrix is produced with *xrtmkarf* command, including PSF correction that accounts for bad pixels and possible loss of counts, important in particular in case of pile-up (which is not the case of our source, since it is not bright). XRT-ARF and RMF (in Energy-keV versus Channel) are shown in Fig. 4.2.
In the end, we used the *grppha* command to associate the extracted spectrum with the background spectrum and the response matrices and to group the channels. The grouping procedure refers to the recast of counts from the original set of channels into a new one,

[1]Telemetry procedure refers to the transmission of collected data from missions like Swift to the receiver on Earth (data can be pre-processed onboard).

[2]The fraction of photons collected within these radii (encircled energy fraction, EEF) is $\sim 70 - 80\%$.

[3]The grade represents the "goodness" of the events to be an X-ray one and is related to the charge spread created by the event on the CCD. For XRT, 32 are the total grades defined.

without changing channel or contents of the spectral files. At first, the data are grouped in order to have 1 count per bin channel.
Observational IDs identifying each exposure, with relative XRT-exposure time, size of source extraction region, source counts and count rate are reported in Table 4.1. As shown from the column 5^{th} of the Table, the total signal is dominated by the source emission.

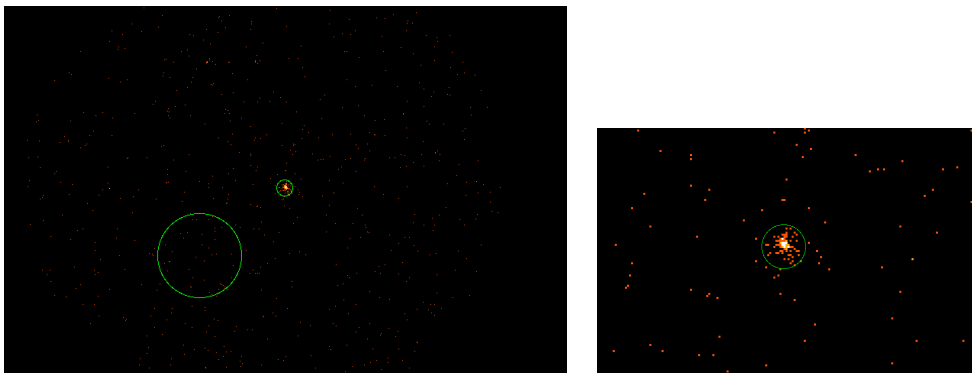

(a) **(b)**

Figure 4.1: Extracted $23' \times 23'$ XRT FOV-image and zoomed on the source region from cleaned event files of the dataset 00034134001 in the 0.3-10 keV energy range.

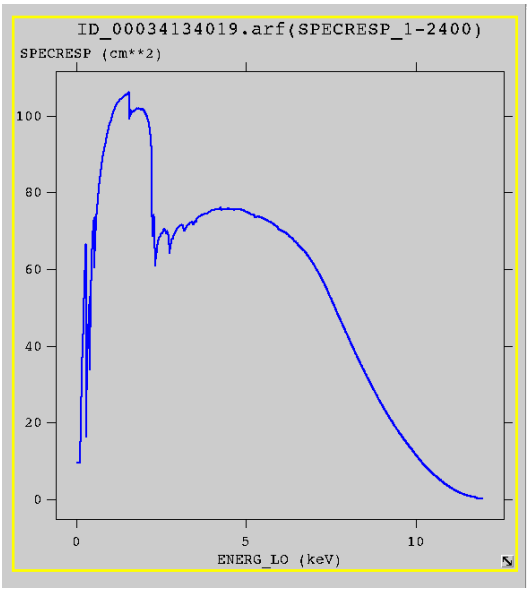

(a) Ancillary Response Matrix (ARF). The ARF distribution represents the telescope sensitivity, hence the mirror+instrument response at a given a position on the detector (in this case, on-axis) and as a function of the photon energy. The capability of collecting photons reaches its maximum below 2 keV and it decreases below 50 % around 5 keV.

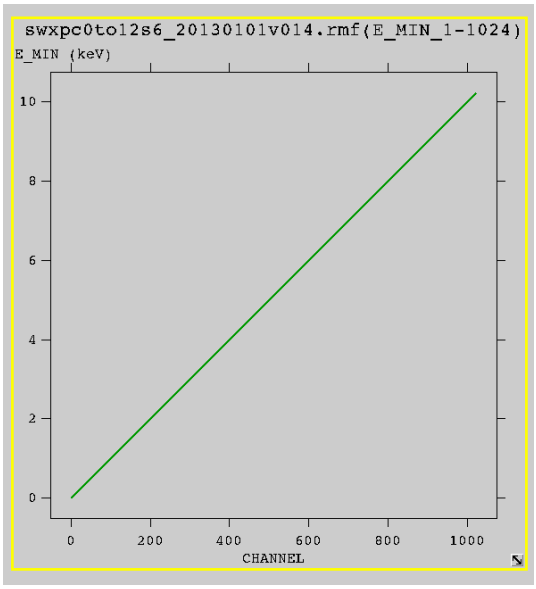

(b) Redistribution Matrix File (RMF). The RMF determines to which channel corresponds a given photon energy and represents the link between the instrumental channel scale and the physical energy scale.

Figure 4.2: Response Matrices for XRT-SWIFT instrument, from the old monitoring reduction for the ARF file (via **xrtmkarf** command) and the RMF, obtained instead from the online database.

ObsID (1)	Date (2)	Exp. time (s) (3)	Src reg(arcsec) (4)	$\frac{Src\,cnts}{Total\,cnts}$ (5)	Net src cnts (6)	(Cnts/s) (7)
			Old Monitoring			
00038045001	2008.11.20	4892	18	99.0 %	46 ± 7	$(9.168 \pm 1.361)10^{-3}$
00038045002	2009.01.28	5030	20	99.5 %	118 ± 11	$(2.353 \pm 0.217)10^{-2}$
00090163002	2009.09.06	5599	20	98.0 %	32 ± 6	$(5.779 \pm 1.026)10^{-3}$
00084954001	2015.01.23	457	20	99.2 %	9 ± 3	$(1.954 \pm 0.657)10^{-2}$
00084954002	2015.02.02	627	13	99.5 %	13 ± 4	$(2.064 \pm 0.575)10^{-3}$
00084954005	2015.03.24	1261	23	99.3 %	8 ± 3	$(6.301 \pm 2.243)10^{-3}$
00034134001	2015.12.14	3251	23	98.8 %	91 ± 10	$(2.795 \pm 0.295)10^{-2}$
00034134002	2015.12.15	4450	21	99.6 %	90 ± 9	$(2.015 \pm 0.213)10^{-2}$
00034134003	2015.12.15	7317	23	99.1 %	112 ± 11	$(1.530 \pm 0.145)10^{-2}$
00034134004	2015.12.19	917	20	99.8 %	28 ± 5	$(3.050 \pm 0.577)10^{-2}$
00034134005	2015.12.19	15890	21	99.1 %	388 ± 20	$(2.444 \pm 0.125)10^{-2}$
00034134006	2015.12.24	8346	20	99.5 %	191 ± 14	$(2.288 \pm 0.166)10^{-2}$
00034134007	2015.12.25	11060	22	99.6 %	312 ± 18	$(2.820 \pm 0.160)10^{-2}$
00034134008	2015.12.29	8131	20	99.3 %	159 ± 13	$(1.954 \pm 0.156)10^{-2}$
00034134009	2015.12.30	5881	21	99.6 %	140 ± 12	$(2.388 \pm 0.202)10^{-2}$
00034134010	2016.01.10	7357	20	99.7 %	226 ± 15	$(3.075 \pm 0.205)10^{-2}$
00034134011	2016.01.12	7295	23	99.5 %	164 ± 13	$(2.250 \pm 0.176)10^{-2}$
00034134012	2016.01.13	944	20	100 %	19 ± 4	$(2.013 \pm 0.462)10^{-2}$
00034134013	2016.01.14	2532	20	99.3 %	42 ± 6	$(1.647 \pm 0.256)10^{-2}$
00034134014	2016.01.14	16830	20	99.3 %	227 ± 15	$(1.351 \pm 0.090)10^{-2}$
00034134015	2016.01.19	3349	20	99.5 %	55 ± 7	$(1.635 \pm 0.222)10^{-2}$
00034134016	2016.01.16	8278	22	99.4 %	194 ± 14	$(2.342 \pm 0.169)10^{-2}$
00034134017	2016.01.21	1116	20	99.5 %	18 ± 4	$(1.604 \pm 0.080)10^{-2}$
00034134018	2016.01.22	1064	17	99.9 %	17 ± 4	$(1.596 \pm 0.388)10^{-2}$
00034134019	2016.01.24	6131	20	99.4 %	88 ± 9	$(1.443 \pm 0.154)10^{-2}$
00034134020	2016.01.27	952	18	98.9 %	14 ± 4	$(1.455 \pm 0.393)10^{-2}$
00034134021	2016.01.28	10340	20	99.4 %	186 ± 14	$(1.797 \pm 0.132)10^{-2}$
00034134022	2016.01.29	15410	22	99.3 %	223 ± 15	$(1.449 \pm 0.973)10^{-2}$
00034134024	2016.02.03	3913	21	99.7 %	89 ± 9	$(2.268 \pm 0.241)10^{-2}$
00034134025	2016.02.03	3606	23	99.4 %	94 ± 10	$(2.602 \pm 0.270)10^{-2}$
00034134026	2016.02.05	11540	19	99.2 %	279 ± 17	$(2.417 \pm 0.145)10^{-2}$
00080403001	2016.02.18	1836	20	99.8 %	47 ± 7	$(2.555 \pm 0.374)10^{-2}$
			New Monitoring			
00034134027	2022.01.04	5092	22	99.2 %	71 ± 8	$(1.403 \pm 0.168)10^{-2}$
00034134030	2022.02.24	5000	17	99.3 %	50 ± 7	$(9.935 \pm 1.414)10^{-3}$
00034134031	2022.03.13	4355	19	99.2 %	26 ± 5	$(5.921 \pm 1.171)10^{-3}$
00034140032	2002.03.30	4860	22	98.7 %	42 ± 7	$(8.736 \pm 1.350)10^{-3}$
00034134033	2022.04.16	4473	22	98.8 %	40 ± 6	$(8.834 \pm 1.414)10^{-3}$
00034134034	2022.05.03	4975	23	96.1 %	59 ± 8	$(1.178 \pm 0.157)10^{-2}$
00034134035	2022.05.20	4887	23	97.9 %	50 ± 7	$(1.022 \pm 0.146)10^{-2}$
00034134036	2022.06.06	4170	21	98.9 %	34 ± 6	$(8.065 \pm 1.398)10^{-3}$
00034134037	2022.06.23	3596	22	98.8 %	38 ± 6	$(1.044 \pm 0.171)10^{-2}$
00034134038	2022.08.04	4555	23	98.3 %	46 ± 7	$(1.014 \pm 0.151)10^{-2}$
00034134039	2022.08.25	3723	20	98.4 %	31 ± 6	$(8.456 \pm 1.520)10^{-3}$
00034134040	2022.09.07	5579	19	99.1 %	78 ± 9	$(1.403 \pm 0.159)10^{-3}$
00034134041	2022.09.24	3656	22	98.1 %	40 ± 6	$(1.100 \pm 0.175)10^{-2}$
00034134042	2022.10.28	4305	23	99.4 %	78 ± 9	$(1.801 \pm 0.205)10^{-2}$
00034134043	2022.11.14	4183	21	98.3 %	46 ± 7	$(1.112 \pm 1.639)10^{-2}$
00034134044	2022.12.04	2924	22	98.7 %	38 ± 6	$(1.316 \pm 0.214)10^{-2}$
00034134045	2022.12.18	3084	23	99.6 %	43 ± 7	$(1.388 \pm 0.213)10^{-2}$
00034134046	2022.12.21	2852	23	99.7 %	53 ± 7	$(1.853 \pm 0.255)10^{-2}$
00034134047	2023.01.04	4573	24	99.0 %	59 ± 8	$(1.300 \pm 0.169)10^{-2}$
00034134048	2023.01.24	4405	20	99.0 %	63 ± 8	$(1.439 \pm 0.182)10^{-2}$
00034134049	2023.02.10	3761	18	99.5 %	45 ± 7	$(1.191 \pm 0.178)10^{-2}$
00034134050	2023.02.15	1154	19	97.3 %	18 ± 4	$(1.602 \pm 0.178)10^{-2}$
00034134051	2023.02.27	4490	21	99.3 %	53 ± 7	$(1.172 \pm 0.162)10^{-2}$
00034134052	2023.03.16	3943	21	98.9 %	58 ± 8	$(1.480 \pm 0.195)10^{-2}$
00034134053	2023.04.02	5199	20	99.7 %	93 ± 10	$(1.784 \pm 0.186)10^{-2}$
00034134054	2023.04.19	4578	19	99.5 %	84 ± 9	$(1.826 \pm 0.200)10^{-2}$
00034134055	2023.05.06	2809	18	99.8 %	35 ± 6	$(1.244 \pm 0.211)10^{-2}$
00034134056	2023.05.20	2053	19	99.5 %	27 ± 5	$(1.309 \pm 0.253)10^{-2}$
00034134057	2023.05.23	4835	24	98.9 %	68 ± 8	$(1.411 \pm 0.172)10^{-2}$
00034134058	2023.06.09	6608	24	99.5 %	133 ± 12	$(2.033 \pm 0.176)10^{-2}$
00034134059	2023.06.26	4415	20	99.4 %	72 ± 8	$(1.620 \pm 0.192)10^{-2}$
00034134060	2023.08.18	3833	17	99.6 %	40 ± 6	$(1.039 \pm 0.165)10^{-2}$
00034134061	2023.09.02	5317	20	98.0 %	25 ± 5	$(4.792 \pm 0.959)10^{-3}$
00034134062	2023.09.19	3821	17	99.6 %	61 ± 8	$(1.590 \pm 0.204)10^{-2}$

Table 4.1: MCG+11-11-032 XRT monitoring. (1): observational ID, (2): observational date (yy.mm.dd), (3): exposure time in units of seconds, (4): size of the circular region for extraction of the source spectrum in arcsec, (5): source contribution in the extraction region compared to the total counts (i.e. src cnts + bkg cnts), (6): background-subtracted source net counts with associated errors (assuming Poisson statistics), (7): net count rate with 1σ errors.

4.2 Data summing procedure

The X-ray analysis is carried out in a low-statistic regime, indeed each observation collected a small amount of photons (typically $\sim 15-200$ counts). Before the spectrum modelling, the individual spectra are combined adopting different time constraints. Initially, the spectra are combined according to the observational date time, producing three single spectra; the first one obtained by considering only data observed up to 2016, the second obtained by considering all the 2022 data and the third one by using 2023 data. In the following chapters, shorter temporal combinations for the new monitoring, i.e. 2022-2023 observations, are adopted in order to investigate line features and line variations on smaller timescales (e.g. on periods of four months).

The command *mathpha* performs the sum in units of counts. Poisson errors are adopted. The procedure is performed both on source spectra and background spectra. The background spectrum needs to be properly scaled, before subtracting the background counts from the source counts extraction region, to account for the different size of the background region compared to the relative source one. To this end, the *dmkeypar* command is used. The last step is to adequately sum the "arf" matrices, weighted by the exposure time fraction of the single exposure compared to the total one (i.e. $weight = \frac{Exposure_i}{Exposure_{tot}}$, where with $Exposure_{tot}$ we refer to $\sum_i Exposure_i$). The total exposure times, fractions of the source counts, net source counts (background-subtracted) and count rates are reported in Table 4.2.

Manually reduced spectra				
Year (1)	Exp. Time (s) (2)	$\frac{Src\,cnts}{Total\,cnts}$ (3)	Net src cnts (4)	Cnts/s (5)
2008-2016	185700	99.2 %	3715 ± 61	$(2.016 \pm 0.033)10^{-2}$
2022	76270	98.1 %	857 ± 29	$(1.146 \pm 0.039)10^{-2}$
2023	65790	99.4 %	938 ± 31	$(1.417 \pm 0.047)10^{-2}$

Table 4.2: Summed spectra as described in Sec. 4.2. (1): Relative years of the summed spectra, (2): total exposure time, (3): source contribution over total counts, (4): source net counts (background-subtracted) with associated errors assuming Poisson distribution, (5): count rate.

4.3 XRT and BAT Light Curves

The light curve of the source shows how the count rate varies with time and traces the source state level. The XRT light curve is shown in Figure 4.3, including both the old and the new monitoring datasets. The associated Poisson error is taken from XSPEC data analysis and correspond to 1σ. The points are color-coded on the basis of the year of observation. The monitoring of 2022-2023 (in dark green and light green) places the source in an intermediate state level with respect to the previous observations and cannot be associated with any previous source state. In particular, a peak is reached around May/June 2023 (vertical orange dash-dotted line), with a rising trend from $\sim$ mid-2022. Adopting the $\sim$ 25 months estimated variability period from BAT studies (Sec. 3.2), looking at the XRT light curve it is possible to identify a previous source peak in 2016. However, we note that the previous data sampling cannot be reliable in terms of variability analysis. Indeed, the previous data sampling is not uniform in time and highly concentrated (the exposures are obtained daily or weekly) in the end of 2015 and at the beginning of 2016. While, on the other hand, the monthly cadence of the recent monitoring is extremely important to confirm the variability period and investigate source variability on different timescales.

Combining the information from the XRT and BAT (hard X-ray energy range) instruments is crucial to provide hints on the nature of MCG+11-11-032 as double system. Indeed, the BAT monitoring extends over a wide range in time (for the 123-months light curve over more than ten years) and can provide additional details about the source variability. The light curve variations presents a periodic behaviour on a timescale of the order of $\sim$ 25 months, as shown by the red points and the dashed line. The 123-months BAT light curve is shown in Figure 4.4 and comprises more or less five periods.

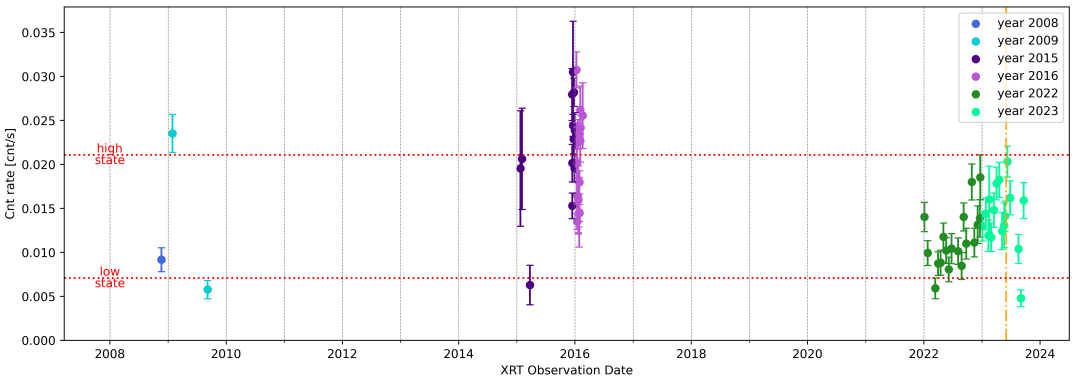

Figure 4.3: XRT Light Curve (0.3-10 keV), comprehensive of the past and current monitoring, from the year 2008 to the year 2023. The observations included are up to Sept 2023. The different colors refers to observations of the same year, as labeled in the legend. 1σ error bars are shown as well. Vertical orange dash-dotted line defines the peak position in the source emission. Red dotted horizontal lines mark the high and low state levels, from the old monitoring analysis, and are placed at the mean count rate of the two different states, respectively.

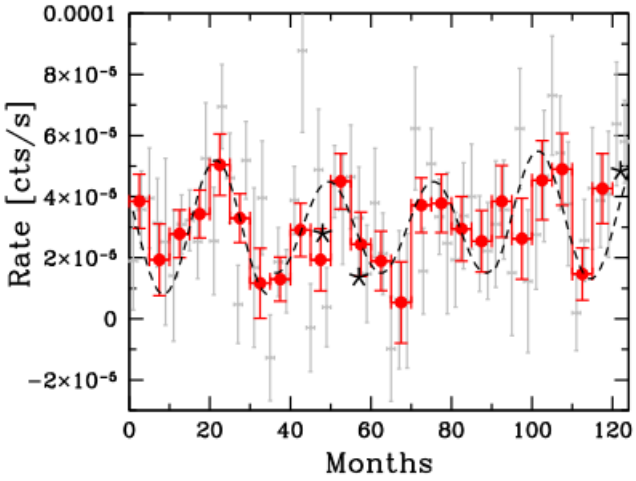

Figure 4.4: BAT Light Curve ($15 - 150$ keV). The grey data points are binned within two months, while red data points are binned within five months. The errors are evaluated at 1σ. Dashed line is the sum of four different sinusoidal curve with same period, but different amplitude, in order to highlight the periodic variability in the source count rate. The three black star-like points represent the rescaled and binned XRT count rate, from datasets obtained at the same BAT observational time. Credit: *Severgnini et al., 2018 [123].*

The analysis of the XRT spectra is reported in the following chapters and in the Table below (4.3) I summarize the structure of the subsequent sections and paragraphs.

General data approach		
Data loading in XSPEC [a]		Sec. 5.1
Model Components		Sec. 5.2
"Summed" Spectrum 2008-2016		
Manual data reduction	binning at 25	Sec. 5.3
Online data reduction	binning at 25	Sec. 5.4
"Summed" Spectrum 2022		
Online data reduction	binning at 25	Sec. 6.1
"Summed" Spectrum 2023		
Online data reduction	binning at 25	Sec. 6.2
Different time grouping		
4-months grouping	binning at 1	Sec. 6.3

Table 4.3: Scheme of the X-ray spectrum modelling strategy.

[a]XSPEC is an interactive X-ray spectral-fitting program. Users' manual can be found at this link: *https: //heasarc.gsfc.nasa.gov/xanadu/xspec/manual/XspecManual.html [65].*

CHAPTER 5

Old monitoring X-ray spectral analysis

In the following sections, the X-ray models adopted for the data analysis are reported and applied to the data observed up to 2016. Both the continuum and line emission are modelled based on the work by *S18* and on the hint of the presence of a double Fe Kα line, a possible signature of a SMBH binary (see also *Serafinelli et al., 2020 [119]*). Different emission line profiles are tested on the spectra.

In the previous work (*S18*), the data reduction from the online software ("Built Swift-XRT products" [1]) was considered; in this thesis, I reduced the data using a script that I developed ("manual" reduction) and compared them with those reduced by the online tool (for details, see section 4.1).

5.1 Data loading in XSPEC

The starting point of this thesis project is devoted to the analysis of the past monitoring. In particular, analysing the XRT monitoring up to 2016 (discussed in *S18*) and comparing the results with the manually-reduced data enabled us to verify the reliability of the online procedure and to validate the model components already tested in *S18*. All the observations, from 2008 up to 2016, are collected in a single "summed" spectrum, referred to as the 2008-2016 "summed" spectrum, via the summing procedure described in section 4.2. We notice that the observations taken in 2008 and 2009 have a small impact on the "summed" spectrum in terms of source counts and exposure times (i.e. being their contribution in counts $< 5\%$) with respect to the daily-weekly observations of December 2015 and January-February 2016. The total exposure time and source counts for the "summed" spectrum are reported in Table 4.2.

At first, the data are binned to have 1 count per bin channel. This is the standard approach adopted for low-photon counting regime (the statistics adopted is the Cash statistics, *Cash, 1979 [17]*). The resultant spectrum is loaded in XSPEC environment, ignoring bad

[1] Online software at this link: *https://www.swift.ac.uk/user_objects/ [78].*

channels and those below 1 keV (dominated by the background) and above 10 keV. In the plotting environment (PGPLOT), the data are plotted in logarithmic scale and as a function of the energy scale [2] (using the information contained in the RMF matrix for the conversion between the channel/instrumental scale to the energy/physical one, see Sec 4.1). In addition, for plotting purpose, source counts are "combined" using the *rebin* command (e.g *setplot rebin 5 10* would combine adjacent bins to reach a significant detection at least as large as 5 (in σ units) grouping a maximum of 10 channels to reach that significance).
An example of the "summed" spectrum of the old monitoring is shown in Figure 5.1 [3].

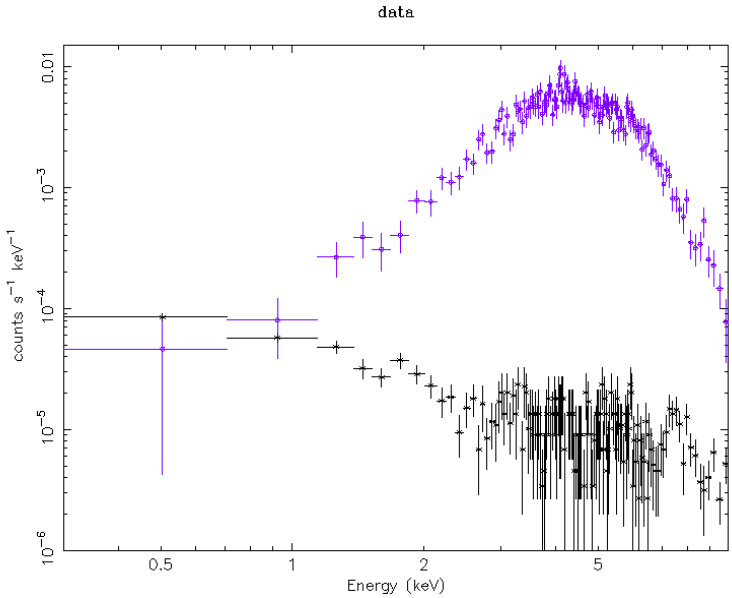

Figure 5.1: 0.3-10 keV MCG+11-11-032 XRT spectrum (purple points) of the summed observations from the past monitoring (2008-2016). Background data points are shown in black. The data are plotted adopting a logarithmic scale and rebinned the collected counts in such a way that each datapoints has a significance of 5σ, grouping no more than 10 bins (for visual purpose only).

The source counts provide statistically significant signal above 1 keV. In agreement with the optical classification as type 2 AGN, MCG+11-11-032 soft X-ray emission appears suppressed, as evident from the low-energy cut-off. The hard band is characterized by a combination of primary power-law and reflection components (see Sec. 1.4 for the description of the emission components).

Regarding the binning choice of the spectra, the line characterization may strongly depend on it. The adopted energy sampling is selected so that it does not oversample the energy resolution of the instrument (for XRT, $\sim$ 140 eV at 6 keV), i.e. the data channels should be grouped into bin channels with a resolution that does not exceed the one of the instrument. In particular, if the energy sampling worsens the spectra resolution, a double line can be observed as one single broad line; conversely, a weak single line cannot be recognized as such if the statistics in a single bin is not high enough.

[2] Indeed, the source spectrum is convolved with the response matrices.
[3] The color code is decoupled from the colors used in the light curve for data points visualization.

When the data are binned, the energy sampling can be verified through *wdata* command. For example, in case of the "summed" spectrum under discussion here (containing the observational datasets from 2008 to 2016), binning at 1 count per bin would produce an energy sampling of $\sim$ 10 eV, while binning at 20 would produce an energy sampling of $\sim$ 70 eV. With the binning choice of 25 counts per bin, the energy sampling is $\sim$ 75 eV.
In addition, the Shannon-Nyquist theorem states that a continuous function $f(x)$ extending in a range of frequency up to ν_{max} may be reconstructed from uniformly spaced samples separated in time by a factor $\frac{1}{2\nu_{max}}$ (or band-limited signal is completely determined by its values at an equally spaced grid), called Nyquist rate (e.g. *Kaastra and Bleeker, 2016 [61]*). In this context, the signal of the X-ray spectrum represents the continous function $f(x)$ and the equally spaced grid values are the energy bins. The Nyquist criterium defined a minimum number of binning points needed to reconstruct the X-ray spectra according to the instrumental energy resolution, maximizing the count statistics in each bin. Therefore, the X-ray spectrum of MCG+11-11-032 binned at 25 counts/bin samples the energy resolution of XRT with at least 2 energy bins.

For this reason, the binning of 25 counts/bin is a good compromise according to the energy resolution of XRT, the Nyquist sampling criterium and the counts statistics (i.e. the adoption of the χ^2 statistics is ensured since the Gaussian regime is achieved in each spectral bin). From now on, the adopted binning is the one at 25 for the subsequent X-ray spectral analysis.

5.2 Model Components

To model the X-ray emission, both the continuum and line emission are considered: the continuum consists of a primary power-law, modulated by the absorption in the soft band that sets the soft energy cut-off depending on the level of obscuration, and a reflection component; as part of the reprocessed emission, line features are included (see Sec. 1.4 and Sec. 1.4.1). The Milky Way absorption in terms of n_H column density is considered as well. These components are presented in the following, and their description is inferred from the XSPEC manual [65]:

- **Galactic absorption** - The n_H parameter is taken directly from XSPEC [4], giving in input the source coordinates (i.e. RA and DEC), and is fixed to $5.20 \cdot 10^{20} cm^{-2}$ from now on in all the spectral analysis. To model the Galactic absorption component, the Tuebingen-Boulder ISM absorption model (*tbabs* in XSPEC) is used. The model takes into account the gas-phase ISM, the grain-phase ISM and molecules of the ISM.

[4]The value is derived from the HI map of the Leiden/Argentine/Bonn (LAB) survey, obtained by merging the Leiden/Dwingeloo Survey (LDS) and the Instituto Argentino de Radioastronomìa Survey (IAR), that shows the HI emission distributed over the Milky Way sky map (*Kalberla P.M.V. et al., 2005 [62]*).

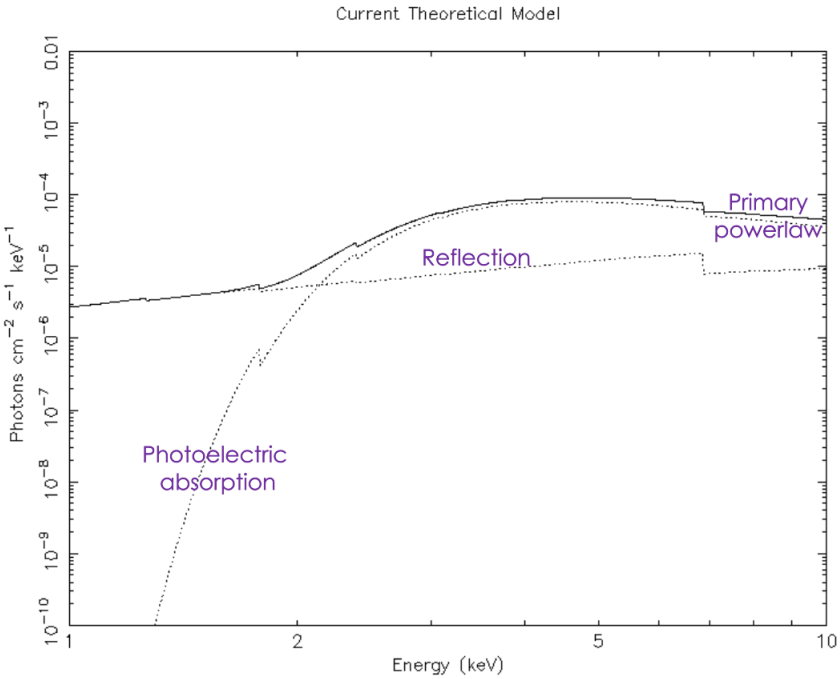

Figure 5.2: Model components in the energy range $1-10$ keV, with intrinsic power-law clearly truncated at low energies because of the photoelectric absorption. The reflection gives its major contribution above 2 keV, but account also for some soft-band continuum emission.

- **Primary power-law** - The *zpowelaw* model in XSPEC accounts for the primary AGN emission, produced by "cold" UV photons from the accretion disk being upscattered by the hot electrons of the corona (see Sec. 1.4). The shape of the power-law function is

$$f(E) = K \cdot [E(1+z)]^{-\alpha} \tag{5.1}$$

  where E is the photon energy, K is the normalization factor (in units of $photons/keV/cm^{-2}/s$ at 1 keV) and α is the dimensionless photon index (see section 1.5).

- **Photoelectric absorption** - The level of intrinsic obscuration is defined through the n_H parameter, expressed by the model *ztbabs* in XSPEC, including the redshift dependence. The absorption component modulates the power-law photon index.

- **Reflection component** - The *pexrav* additive component is included for the continuum fitting of the hard X-ray energy range. Its origin is related to the reprocessed radiation coming from the hot corona: these photons impact back on the disk and are radiated away (see Section 1.4). The *pexrav* model is an exponential cut-off power-law reflected by neutral material. The only reflection component is obtained by setting the *refl* parameter to be negative. For all the models presented in the following, the reflection component is constrained between -2 and 0. The photon index of this component is linked to the one of the intrinsic power-law, as well as the normalization. The cut-off energy is set to 100 keV. The metal abundance (in units of solar abundance) and

iron one (relative to the metal one) are set at standard values, in these models both equal to 1. The *cos(i)*, with i the angle between the line of sight and the plane of the disk from where the *pexrav* emission component originates, of the material responsible for this component is frozen to the default value of 0.45. Even if the *pexrav* model gives its major contribution in the hard X-ray band, it is used also to model in a more appropriate way the soft data points with energies below 2 keV.

5.3 Manually-reduced spectrum

First of all, we analysed the "2008-2016" summed spectrum, which was already reported by *S18*. We tested both data reduction approaches, reducing the observations with the online tool or with the manual reduction. The latter is reported first.
The first model applied on the X-ray spectrum accounts for the continuum emission and comprises an absorbed power-law and a reflection component, as described in the above Section. Figure 5.3 shows clearly that the continuum emission is well fitted, since the residuals place around 0. The best fit values [5] are reported in Table 5.1, with associated errors at the 90% confidence level for one parameter of interest (*Avni, 1976 [7]*) and the statistics in terms of reduced χ^2 (i.e. [χ^2 over *degrees of freedom* [6]]). The photon index, relative normalization, intrinsic column density and reflection parameter are consistent within the errors with previous results from the analysis performed in *S18 [123]*; therefore, the current fitting model for the continuum (i.e. *tbabs*(pexrav+ztbabs*zpo)* in XSPEC) is adopted hereafter for the X-ray analysis.

tbabs(pexrav+ztbabs*zpo)*				
Model component	Model name	Parameter		
1	pexrav	1	refl	$-1.64^{+0.56}_{*}$
2	ztbabs	1	$n_H(10^{22})$	$13.1^{+1.8}_{-1.6}$
3	zpo	1	Gamma	$1.58^{+0.21}_{-0.20}$
		2	norm	$\left(1.67^{+0.89}_{-0.56}\right) \cdot 10^{-3}$

Table 5.1: Model parameters and best fit values for the continuum emission of the "summed" spectrum 2008-2016 ($\tilde{\chi}^2 = \frac{\chi}{dof} = \frac{124.8}{125}$). The " * " symbol in the error evaluation of the "refl" parameter indicates that the 90% lower error of the reflection component is consistent with the boundary value of -2.

The reflection parameter, confined to the negative values in the range [-2;0], is compatible with *S18* estimation (~ 0.09, defined as the ratio between the 2-10 keV flux of the reflected and direct continuum components, which corresponds to a *refl* parameter of ~ -1).

[5] The parameters that are not reported in the Table, like the Galactic absorption, the *pexrav* cut-off energy and so on, are set as defined in the model lists of the previous section (Sec. 5.2).
[6] The degrees of freedom for the model are defined as: *n° of datapoints-n° of free parameters.*

The parameters n_H and Γ are degenerate, as also shown by the contour plot, reported in Figure 5.4.

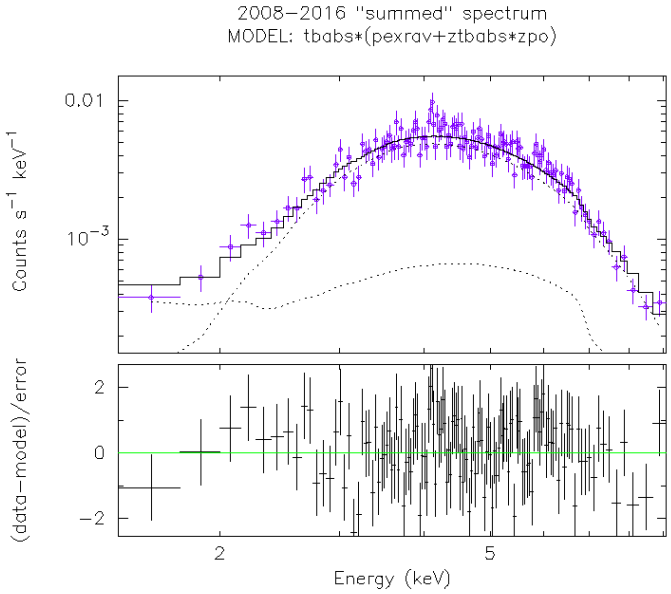

Figure 5.3: MCG+11-11-032 "summed" 1-10 keV spectrum (2008-2016), binned at 25 counts per bin, reported in units of $counts\, s^{-1}\, keV^{-1}\, cm^{-2}$ (purple circle points); The fit model (black line) is shown in the upper panel with dotted lines representing the individual components. Residuals in units of χ, i.e. the difference between data and model (in units of σ) are plotted in the lower panel.

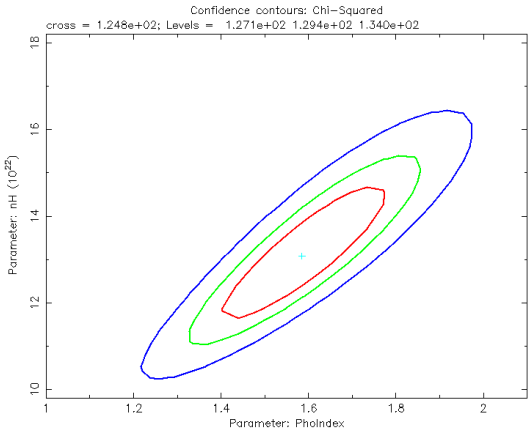

Figure 5.4: Contour plot n_H-Γ. The contours at the 68% (in red), 90% (in green) and 99% (in blue) confidence levels are shown.

The possible presence of an Fe emission line at the rest-frame energy of 6.4 keV is tested adding a line component. *zgauss* is defined with the line energy in the source frame in keV, the width in keV, the redshift and the $photons/cm^{-2}/s$ in the line as normalization. The

width parameter is frozen at $\sigma = 0.01$ keV. The *zgauss* line energy best-fit value is at $6.18^{+0.09}_{-0.08}$ keV, with significance of 2.4σ, consistent with the one from *S18* (see section 3.2). Adding a line component improves significantly the fit (i.e. $\frac{\Delta\chi^2}{k} = 6$, with k the difference between the degrees of freedom of the two models).
The best fit values are reported in Table 5.2. Model fitting and relative line contour plot are shown in Figure 5.5.

tbabs(zgauss+pexrav+ztbabs*zpo)*				
Model component	Model name	Parameter		
1	zgauss	1	Line E (keV)	$6.18^{+0.09}_{-0.08}$
		2	norm	$(8.83 \pm 5.04) \cdot 10^{-6}$
2	pexrav	1	refl	$-1.54^{+0.55}_{*}$
3	ztbabs	1	$n_H(10^{22} cm^{-2})$	$12.9^{+1.7}_{-1.6}$
4	zpo	1	Gamma	1.61 ± 0.21
		2	norm	$\left(1.70^{+0.93}_{-0.58}\right) \cdot 10^{-3}$

Table 5.2: Model parameters and best fit values for the "summed" spectrum 2008-2016 with the addition of a line component ($\tilde{\chi}^2 = \frac{\chi}{dof} = \frac{116.5}{123}$). The " * " in the error evaluation of the "refl" parameter indicates that the 90% lower error of the reflection component is consistent with the boundary value of -2.

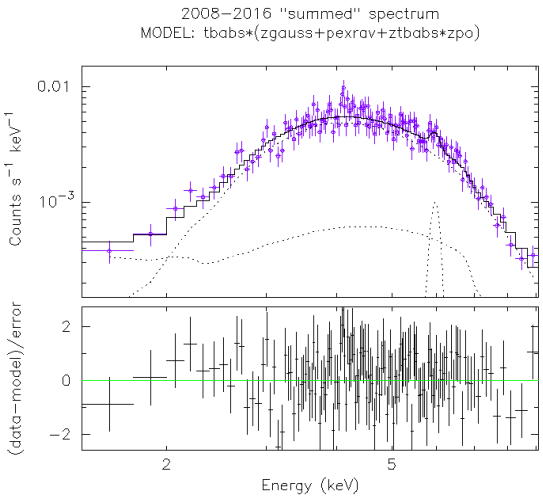

(a) Source "summed" spectrum (2008-2016), binned at 25 counts/bin (purple points). Refer to Fig. 5.3 for the units of the spectrum and panels description. Model components are shown with dotted lines.

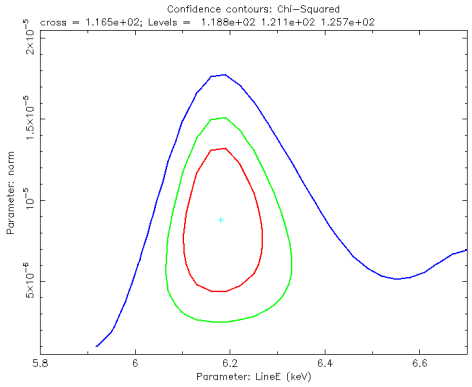

(b) Contour plot of line energy-normalization. The contour levels are the same as in Figure 5.4.

Figure 5.5: MCG+11-11-032 1-10 keV "summed" spectrum in panel **(a)** and line contour plot in panel **(b)**.

The contour plot (Figure 5.5) at 99 % confidence level extends at energies larger than 6.2 keV. This shape suggests the possible presence of another line component. For this reason, another narrow emission line is added. While the first line remains stable at 6.18 ± 0.09 keV, the second feature is found at ~ 6.7 keV. However, it is noteworthy that both error evaluation and contour plot of this second line are inconclusive (see Figure 5.6 for spectrum and fit model and for contour plot relative to the 6.18 keV line).
The significance of the additional narrow line is below 1σ and does not improve the spectra modelling. In the *S18* work, the second line was found at 6.56 ± 0.16 keV, thus compatible with a line energy at ~ 6.7 keV. The difference can be attributed to the data reduction and binning choice, being the line strongly sensitive to both. The best fit values are reported in Table 5.3, adopting the same confidence level for the error evaluation. The observed-frame 2-10 keV flux is $4.8\,[4.1 - 4.9]\,10^{-12}\frac{erg}{cm^2\,s}$.

tbabs(zgauss+zgauss+pexrav+ztbabs*zpo)*				
Model component	Model name	Parameter		
1	zgauss	1	Line E (keV)	6.18 ± 0.09
		2	norm	$(9.10 \pm 5.05) \cdot 10^{-6}$
2	zgauss	1	Line E (keV)	$\underline{6.70}$
		2	norm	$\left(3.61^{5.35}_{*}\right) \cdot 10^{-6}$
2	pexrav	1	refl	$-1.46^{+0.54}_{*}$
3	ztbabs	1	$n_H(10^{22}cm^{-2})$	$12.9^{+1.7}_{-1.6}$
4	zpo	1	Gamma	1.64 ± 0.22
		2	norm	$\left(1.70^{+1.01}_{-0.62}\right) \cdot 10^{-3}$

Table 5.3: Model parameters and best fit values for the "summed" spectrum 2008-2016 with two narrow line components ($\tilde{\chi}^2 = \frac{\chi}{dof} = \frac{115.3}{121}$). The second line energy is underlined to indicate that the error evaluation does not converge. The " * " in the error evaluation of the "refl" parameter indicates that the 90% lower error of the reflection component is consistent with the boundary value of -2. In case of normalization, the " * " symbol means that the evaluation is consistent with the boundary value of 0.

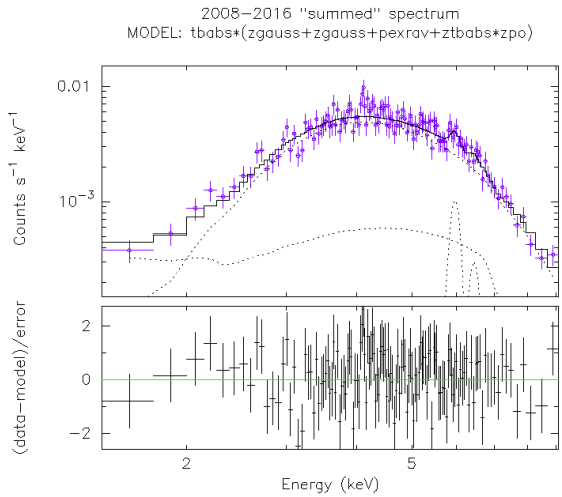

(a) Source "summed" spectrum (2008-2016), binned at 25 counts/bin (purple points). Refer to Fig. 5.3 for the units of the spectrum and panels description. Model components are shown with dotted lines.

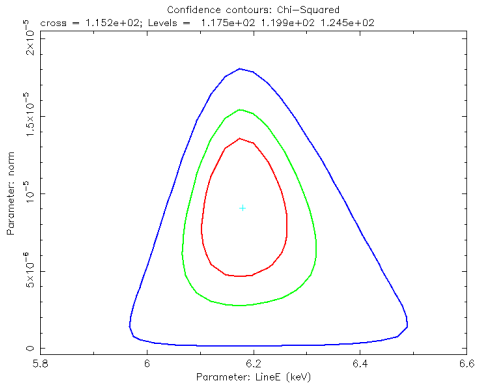

(b) Contour plot of line energy-normalization from the line of lower-energy in the model. The contour levels are the same as in Figure 5.4.

Figure 5.6: MCG+11-11-032 1-10 keV "summed" spectrum and line contour plot in panel **(b)**.

5.4 Online-reduced spectrum

In the X-rays study of MCG+11-11-032, the online-reduced spectrum, presented in *S18*, is also considered. In *S18* work the adopted binning was of 50 counts/bin. Since the binning choice can play an important role in the line sampling, we re-analyzed also the online spectrum using a different binning, i.e. 25 counts/bin (the results are reported in this section).

The online-reduced spectrum is obtained from the "Build Swift-XRT products" tool (*[78]*). The *object name*, *target ID* (interested "ObsID" minus last 3 digits) and *source coordinates* (in terms of source RA and DEC) are given as inputs. The other parameters are left as default, like the *centroid option* and the *search radius* of 1 arcmin (i.e. the software looks for source localization within 1 arcmin from the source position and assumes the brightest object in the region to be the source of interest). The spectrum obtained using the online tool is extracted to maximize the signal-to-noise ratio (see *Evans et al., 2009 [34]*). The online-tool works both on individual observations, giving in input the specific *ObsID*, and on multiple observations, with the *target ID* as input and computing automatically the summing procedure, hence producing a single "summed" spectrum. The total exposure times, fraction of the source counts, net source counts (background-subtracted) and count rates are reported in Table 5.4.

Online reduced spectrum: old monitoring				
Year	Exp. Time (s)	$\frac{Src\,cnts}{Total\,cnts}$	Net src cnts	Cnts/s
(1)	(2)	(3)	(4)	(5)
2008-2016	165900	99.1 %	3921	$(2.363\pm0.0379)\cdot10^{-2}$

Table 5.4: Summed spectra for the X-ray modelling. (1): relative years of the summed spectra, (2): total exposure time, (3): source contribution over total counts, (4): source net counts (background-subtracted) with associated errors assuming Poisson distribution, (5): count rate.

The fitting components are adopted as in the previous section, with the same continuum modelling and eventually line components. The continuum fitting produces consistent best-fit parameters within errors with the fitting shown in Sec. 5.3 on the manually-reduced spectrum. The positive residuals around 6 keV of panel **(a)** in Figure 5.7 suggest the addition of a narrow ($\sigma = 0.01$ and frozen) line component (*zgauss* additive XSPEC model). The line energy is fit at $6.16^{+0.11}_{-0.08}$ keV (panel **(b)**), with significance of 2.2σ, in agreement with *S18* results. Its EW is $98[46-154]$ eV. By looking at the line energy vs normalization contour plot, the contour at the 90% confidence level suggests the presence of an additional line at energies larger than 6.4 keV (panel **(c)**). When a second narrow line is added to the fit, the first line remains stable at 6.14 ± 0.08 keV (with $EW = 81[22-137]$ eV), while the second one is placed at $6.50^{+0.15}_{-0.14}$ keV (with $EW = 97[40-166]$ eV), which is compatible with the one from *S18*. This second component is poorly constrained and its significance is about 1.5σ. The spectrum and fit model are shown in Figure 5.7, with relative line contour plots. The relevant best fit values of the modelling are reported in Table 5.5.

tbabs(pexrav+ztbabs*zpo)*				
Model component	Model name	Parameter		
2	pexrav	1	refl	$-1.38^{+0.44}_{-0.58}$
3	ztbabs	1	$n_H(10^{22}cm^{-2})$	$14.6^{+1.7}_{-1.6}$
4	zpo	1	Gamma	$1.74^{+0.20}_{-0.19}$
		2	norm	$\left(2.24^{+1.16}_{-0.74}\right)\cdot 10^{-3}$
tbabs(zgauss+pexrav+ztbabs*zpo)*				
Model component	Model name	Parameter		
1	zgauss	1	Line E (keV)	$6.16^{+0.11}_{-0.08}$
		2	norm	$(8.07 \pm 4.67)\cdot 10^{-6}$
2	pexrav	1	refl	$-1.32^{+0.43}_{-0.57}$
3	ztbabs	1	$n_H(10^{22}cm^{-2})$	$14.4^{+1.71}_{-1.59}$
4	zpo	1	Gamma	$1.76^{+0.21}_{-0.20}$
		2	norm	$\left(2.27^{+1.19}_{-0.76}\right)\cdot 10^{-3}$
tbabs(zgauss+zgauss+pexrav+ztbabs*zpo)*				
Model component	Model name	Parameter		
1	zgauss	1	Line E (keV)	6.14 ± 0.08
		2	norm	$\left(7.91^{+4.70}_{-4.75}\right)\cdot 10^{-6}$
2	zgauss	1	Line E (keV)	$6.50^{+0.15}_{-0.14}$
		2	norm	$\left(6.30^{+4.90}_{-4.85}\right)\cdot 10^{-6}$
2	pexrav	1	refl	$-1.24^{+0.42}_{-0.54}$
3	ztbabs	1	$n_H(10^{22}cm^{-2})$	$14.4^{+1.71}_{-1.59}$
4	zpo	1	Gamma	$1.80^{+0.22}_{-0.20}$
		2	norm	$\left(2.39^{+1.31}_{-1.59}\right)\cdot 10^{-3}$

Table 5.5: Model parameters and best fit values of the "summed" spectrum 2008-2016 ($\tilde{\chi}^2 = \frac{\chi}{dof} = \frac{152.5}{133}$ for model at the top, $\tilde{\chi}^2 = \frac{\chi}{dof} = \frac{144.3}{131}$ for model in the middle, $\tilde{\chi}^2 = \frac{\chi}{dof} = \frac{139.9}{129}$ and 2-10 keV flux of $4.5\,[3.9-4.6]\,10^{-12}\frac{erg}{cm^2\,s}$ for model at the bottom).

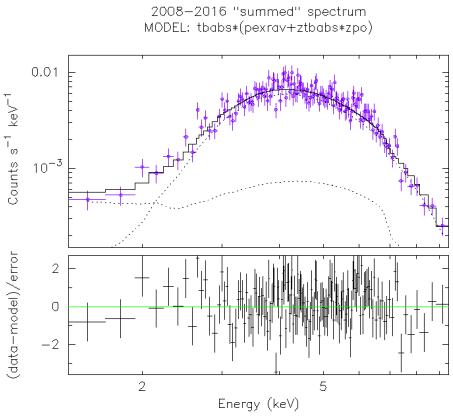

(a) Continuum fitting

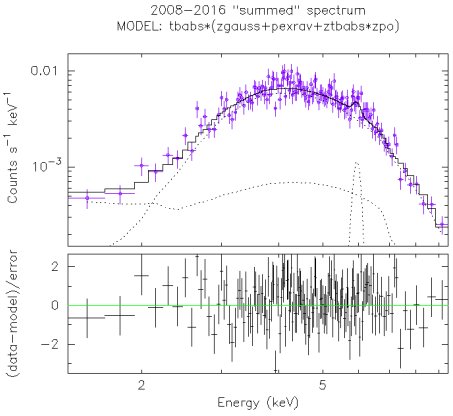

(b) One line component.

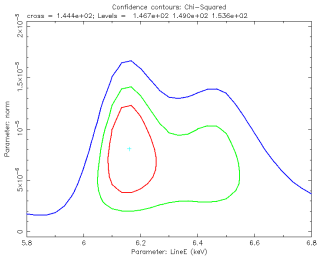

(c) contour plot.

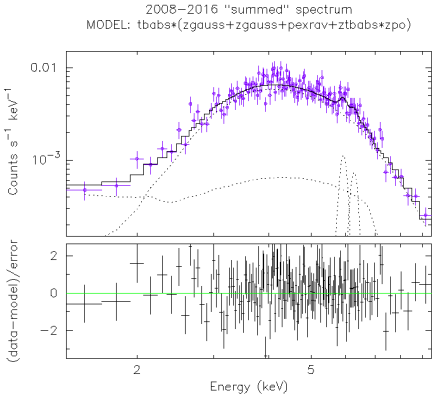

(d) Two line components.

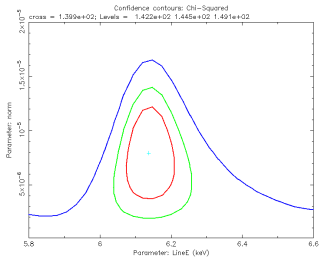

(e) Contour plot ($\sim$ 6.14 keV line).

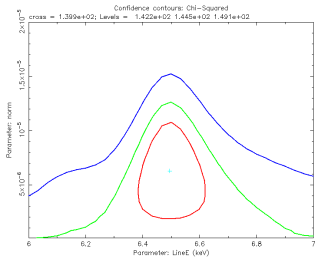

(f) Contour plot ($\sim$ 6.50 keV line).

Figure 5.7: Source "summed" spectrum (2008-2016) using the online-reduction tool, binning at 25 counts/bin (purple points), reported in units of $counts\, s^{-1} keV^{-1} cm^{-2}$, with fit model (black line) and model residuals in units of χ in each spectrum fitting. Continuum modelling is presented in panel **(a)**, the model with one narrow emission line in panel **(b)**; model with two narrow emission lines in panel **(d)**. The relative line energy vs normalization contour plots are displayed in panels **(c)**, **(e)** and **(f)**.

To summarize, from the analysis of the manually-reduced spectrum, an intrinsic absorbed power-law plus a reflection component is a statistically good fit for the continuum emission. The binning choice of 25 counts per bin is considered, since it samples properly the spectrum according to the energy resolution of the instrument and the Nyquist criterium. The addition of a single narrow line component at energy ~ 6.18 keV improved statistically the fit and the contour plot on the line-normalization suggests the addition of a second narrow line. This second line feature is not constrained, by using both the manual data reduction and the online one, and its significance is low.
When the online-reduced spectrum is modelled, the results are consistent within the errors with the modelling of the manually-reduced spectrum. Hence, for the subsequent chapter on the analysis of the new monitoring data, the online data reduction is considered and all the presented spectra will be obtained from "Built XRT products" tool. The results presented in this chapter concerning the emission line properties are summarized in Table 5.6.

Line comparison in "2008-2016" summed spectrum			
Spectrum	Line configuration	Line energy [keV]	Line significance [σ]
S18	Single line	6.18 ± 0.09	2.6
	Double line	6.16 ± 0.08 6.56 ± 0.16	1.3
Manually-reduced spectrum	Single line	$6.18^{+0.09}_{-0.08}$	2.4
	Double line	6.18 ± 0.09 $\underline{6.7}$	< 1
Online-reduced spectrum	Single line	$6.16^{+0.11}_{-0.08}$	2.2
	Double line	6.14 ± 0.08 $6.50^{+0.15}_{-0.14}$	1.5

Table 5.6: Summaring on the line fitting of different spectra used for the old monitoring (2008-2016) analysis.

CHAPTER 6

New monitoring X-ray spectral analysis

In this chapter, the X-ray modelling of the 2022-2023 spectra is reported. The exposure time and source counts of the individual observations are reported in Table 4.1. All the data collected in 2022 are summed in a single spectrum, referred to as the 2022 "summed" spectrum, and those collected in 2023 in a single spectrum referred to as the 2023 "summed" spectrum. Following the considerations reported in Sec. 5.1, the two spectra are obtained from the online tool, and channels are grouped to have 25 counts/bin.

It is worth mentioning that by grouping the data to have 1 counts/bin (as usual in X-rays in the case of low-statistics regime) or at a signal-to-noise ratio of 3 in each bin, we obtained results similar to those derived by adopting a binning of 25 counts/bin, i.e. the parameter values are consistent within the errors. The exposure times, fraction of source counts over total ones, the net source counts and count rate are reported in Table 6.1.

Online reduced spectrum: new monitoring				
Year	Exp. Time (s)	$\frac{Src\,cnts}{Total\,cnts}$	Net src cnts	Cnts/s
(1)	(2)	(3)	(4)	(5)
2022	76270	98.9 %	955 ± 31	$(1.238 \pm 0.004)10^{-2}$
2023	65790	98.8%	1072 ± 33	$(1.629 \pm 0.005)10^{-2}$

Table 6.1: Summed spectra obtained from the 2022 and 2023 observations. (1): Year of observations (2): total exposure time, (3): source contribution over total counts, (4): source net counts (background-subtracted) with associated errors assuming Poisson distribution, (5): count rate.

6.1 2022 Monitoring

The 2022 "summed" spectrum is loaded in XSPEC ignoring bad channels and those below 1 keV (background dominated) and above 10 keV. The fitting model includes a continuum plus line emission (*tbabs*(zgauss+pexrav+ztbabs*zpo)* in XSPEC), already used in Sec. 5.2. To better visualize the 1-10 keV spectrum, the source counts are further binned using the *rebin* command (in this case *setplot rebin 3 6*). The best fit results and the $n_H - \Gamma$ contour plot are consistent with those reported in the previous chapter (see Sec. 5.4 for continuum modelling and Sec. 5.3 for contour plot). We will concentrate on the modelling of the hard X-ray emission (i.e. above 2 keV), in particular on the study of the Fe emission lines.

By fitting the continuum emission with an absorbed power-law plus a reflection component (*tbabs*(pexrav+ztbabs*zpo)* in XSPEC), significant positive residuals are left around 6 keV. Tha addition of a narrow emission line component improved the fit by $\frac{\Delta\chi^2}{k} = \frac{32.7-22.5}{2} \sim 5.1$. The emission line is significant at the $\sim 3\sigma$ level and has an energy of $6.24^{+0.09}_{-0.10}$ keV (with $EW = 250[122 - 378]$ eV). Figure 6.1 displays both the model fitting and the contour plot of the line energy versus normalization. Best fit values, with error evaluation, are reported in Table 6.2. The line energy is consistent, within the errors, with the line modelling of the 2008-2016 "summed" spectrum (i.e. red line component at energy of $6.16^{+0.11}_{-0.08}$ keV).

tbabs(zgauss+pexrav+ztbabs*zpo)*				
Model component	Model name	Parameter		
1	zgauss	1	Line E (keV)	$6.24^{+0.09}_{-0.10}$
		2	norm	$\left(1.21^{+0.62}_{-0.62}\right) \cdot 10^{-5}$
2	pexrav	1	refl	$-1.43^{+0.77}_{*}$
3	ztbabs	1	$n_H(10^{22})$	$20.6^{+5.3}_{-4.9}$
4	zpo	1	Gamma	$2.0^{+0.56}_{-0.49}$
		2	norm	$\left(2.27^{+5.04}_{-1.39}\right) \cdot 10^{-3}$

Table 6.2: Model parameters and best fit values for the 2022 "summed" spectrum with the addition of a line component ($\tilde{\chi}^2 = \frac{\chi}{dof} = \frac{22.5}{31}$). The " * " in the error evaluation of the "refl" parameter indicates that the 90% lower error of the reflection component is consistent with the boundary value of -2.

The right panel in Fig. 6.1 indicates that the rest-frame energy of the emission line is not consistent with the rest-frame energy of the neutral Fe Kα emission line at the 90 % confidence level. In addition, the shape of the 99 % confidence level line suggests the presence of a second emission line at rest-frame energies lower than 6.2 keV. A similar hint comes also from the positive residuals around 6 keV of Fig. 6.1, panel **(a)**.

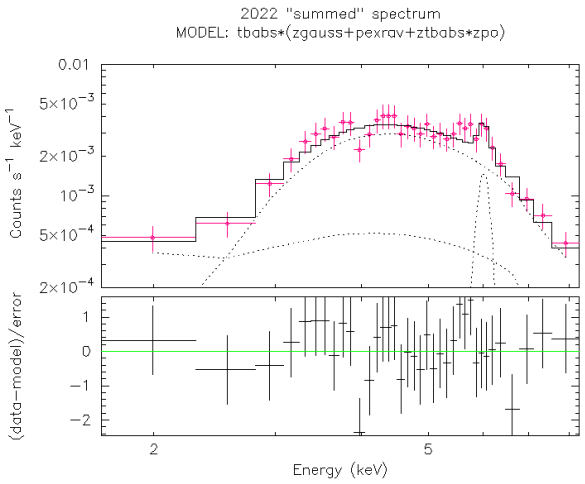

(a) Source "summed" spectrum (2022) binned at 25 counts/bin (pink points). Refer to Fig. 5.3 for units of the spectrum and panels description. Model components are shown with dotted lines.

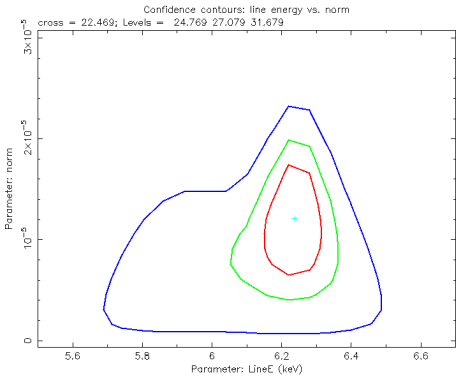

(b) Contour plot of line energy-normalization. The contour levels are the same as in Fig. 5.4.

Figure 6.1: MCG+11-11-032 1-10 keV "summed" spectrum of 2022 monitoring and line contour plot in panel **(b)**.

When a second line component is added to the model, the best fit energy value of the bluer emission line remains almost unchanged ($E = 6.25 \pm 0.09$ keV and $EW = 256[127-401]$ eV), while the energy of the redder component converges to $E = 5.86^{+0.15}_{-0.14}$ keV (with $EW = 154[42-268]$ eV) and its significance is roughly 2.3σ. Model fitting and relative line contour plots are shown in Figure 6.2, while model best fit values are reported in Table 6.3. The observed-frame 2-10 keV flux is $2.5\,[0.4-2.7]\,10^{-12}\frac{erg}{cm^2\,s}$.

tbabs(zgauss+zgauss+pexrav+ztbabs*zpo)*				
Model component	Model name	Parameter		
1	zgauss	1	Line E (keV)	$5.86^{+0.15}_{-0.14}$
		2	norm	$\left(7.45^{+5.47}_{-5.42}\right)\cdot 10^{-6}$
2	zgauss	1	Line E (keV)	6.25 ± 0.09
		2	norm	$(1.22 \pm 0.63)\cdot 10^{-5}$
3	pexrav	1	refl	$-1.46^{+0.81}_{*}$
4	ztbabs	1	$n_H(10^{22})$	$19.7^{+5.2}_{-4.9}$
4	zpo	1	Gamma	$1.99^{+0.58}_{-0.52}$
		2	norm	$\left(2.10^{+4.83}_{-1.32}\right)\cdot 10^{-3}$

Table 6.3: Model parameters and best fit values for the 2022 "summed" spectrum with two narrow line components ($\tilde{\chi}^2 = \frac{\chi}{dof} = \frac{17.4}{29}$). The " * " in the error evaluation of the "refl" parameter indicates that the 90% lower error of the reflection component is consistent with the boundary value of -2.

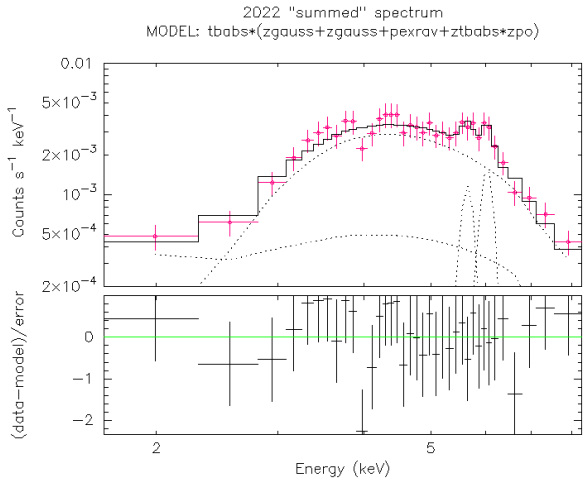

(a) Source "summed" spectrum (2022), binned at 25 counts per bin. Refer to Fig. 5.3 for the units of the spectrum and panels description. Model components are shown with dotted lines.

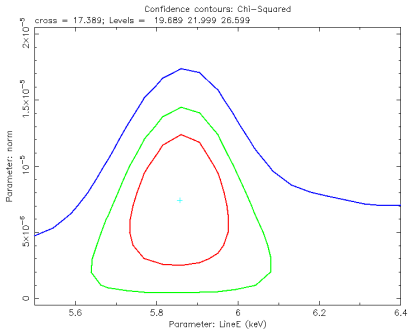

(b) Contour plot of line energy-normalization from the line component at lower enegies in the model.

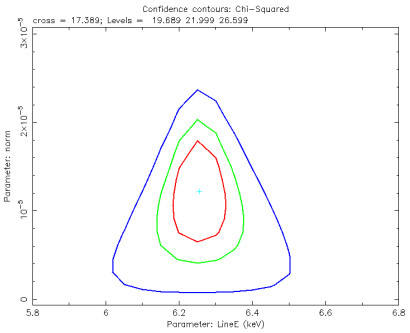

(c) Contour plot of line energy-normalization from the line component at larger energies in the model.

Figure 6.2: MCG+11-11-032 1-10 keV "summed" spectrum of 2022 monitoring and line contour plots in panel **(b)** and **(c)**. The contour levels are the same as in Fig. 5.4.

By comparison with the results obtained with the 2008-2016 spectrum, the continuum best fit parameters are consistent within the errors. The 2-10 keV flux level is on average $\sim 2.5\,10^{-12}\frac{erg}{cm^2\,s}$ for the 2022 spectrum, a factor ~ 2 lower with respect to the 2008-2016 spectrum ($F_{2-10\,keV} \sim 4.5\,10^{-12}\frac{erg}{cm^2\,s}$). When a second line is added to the fit, it is red-shifted with respect to the ~ 6.2 keV energy, while in 2008-2016 modelling a second line was found blue-shifted with respect to the ~ 6.2 keV energy.

To summarize, the 2022 "summed" spectrum is well fitted by an absorbed continuum and a reflection component plus a single narrow emission line at the same energy as the 2008-2016 previous modelling. The model with two narrow Gaussian emission lines (best fit values of $E = 5.86^{+0.15}_{-0.14}$ keV, with significance $\sim 2.2\sigma$, and $E = 6.25 \pm 0.09$ keV, with significance $\sim 2.3\sigma$) reproduces well the source datapoints.

6.2 2023 Monitoring

The monitoring obtained by *S18* is still ongoing at the time of writing this thesis, and the observations up to September 2023 are included in my analysis. In agreement with the analysis presented in the previous sections, the 2023 "summed" spectrum is binned in order to have 25 counts/bin, and bad channels and the those below 1 keV and above 10 keV are ignored. The continuum emission is fitted using the same model as described for 2022 "summed" spectrum (*tbabs*(pexrav+ztbabs*zpo)* in XSPEC).

The positive residuals around 6 keV suggest the possible presence of an emission line around $6 - 7$ keV. However, by adding a narrow Gaussian component, the fit does not improve significantly ($\frac{\chi^2}{dof} = \frac{26.8}{36}$ vs. continuum model $\frac{\chi^2}{dof} = \frac{29.9}{38}$). The emission line, with best fit energy of $E = 6.62^{+0.27}_{-0.29}$ keV, turns out to have a low significance (1.5σ), with poorly constrained energy and normalization values (see contour plot in panel **(b)** of Fig. 6.3). Best fit values are reported in Table 6.4, while X-ray spectrum, model components and line energy vs. normalization contour plot are shown in Figure 6.3.

tbabs(zgauss+pexrav+ztbabs*zpo)*				
Model component	Model name	Parameter		
1	zgauss	1	Line E (keV)	$6.62^{+0.19}_{-0.25}$
		2	norm	$\left(7.53^{+7.13}_{-6.94}\right) \cdot 10^{-6}$
2	pexrav	1	refl	$-0.74^{+0.46}_{-0.76}$
3	ztbabs	1	$n_H(10^{22})$	$14.9^{+2.96}_{-2.69}$
4	zpo	1	Gamma	$2.19^{+0.48}_{-0.43}$
		2	norm	$\left(3.37^{+5.07}_{-1.91}\right) \cdot 10^{-3}$

Table 6.4: Model parameters and best fit values for the "summed" spectrum 2023 with the addition of a line component (statistics $\tilde{\chi}^2 = \frac{\chi}{dof} = \frac{26.8}{36}$).

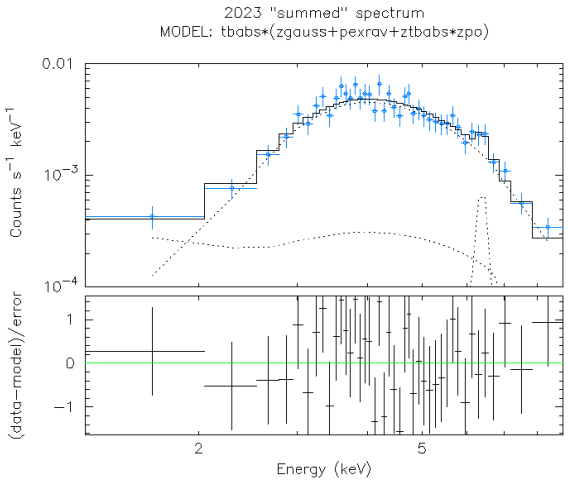

(a) Source "summed" spectrum (2023), binned at 25 counts/bin (light blue points). Referred to previous figures for units of the spectrum and panel description. Model components are shown with dotted lines.

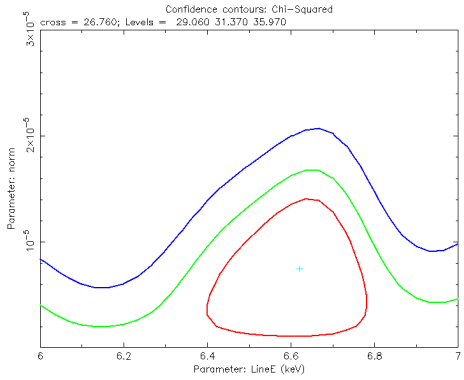

(b) Contour plot of line energy-normalization. The contour levels are the same as in previous figures.

Figure 6.3: MCG+11-11-032 2023 "summed" 1-10 keV spectrum and line contour plot in panel **(b)**.

In the single line model presented above, there is no evidence for significant positive residuals in the $6-7$ keV energy range (panel **(a)** of Figure 6.3).
The continuum emission in 2023 is higher than that measured in 2022 by 10 %. To investigate whether the absence of a significant line detection at ~ 6.2 keV in 2023 is attributed to an increased continuum contribution compared to a constant line intensity or to an effective reduction in the line emission, we incorporate a line in the 2023 modeling with the same energy and intensity as observed in 2022. The results are shown in Fig. 6.4; notably, such a line would have been detected in the 2023 spectrum if it had the same intensity measured in 2022. This implies that the line in 2023 has a flux definitely lower than that of 2022 ($F_{line} < 1.1 \cdot 10^{-13} \frac{erg}{cm^2\, s}$). In the 2023 modelling, we can place stronger constraints by computing the flux of the continuum at energies $E = 6.18 - 6.25$ keV (i.e., in a spectral region centered on the line). We obtain $\sim 2.5\,[0.6 - 2.6]\, 10^{-14} \frac{erg}{cm^2\, s}$, hence the line intensity is lower than $2.6 \cdot 10^{-14} \frac{erg}{cm^2\, s}$. Overall, while the continuum emission increases from 2022 to 2023 by 10 %, the 6.25 keV-line decreases by at least a factor of 4, resulting to be highly variable.

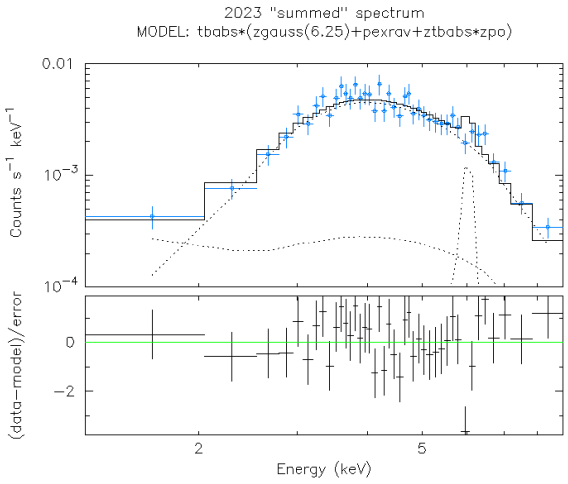

(a) Source "summed" spectrum (2023), binned at 25 counts/bin (light blue points). Refer to previous figures for units of the spectrum and panel description. Model components are shown with dotted lines.

Figure 6.4: MCG+11-11-032 2023 "summed" 1-10 keV spectrum with line feature of fixed energy.

6.3 Forth-months temporal binning

As anticipated in Sec. 4.2, the data summing adopted in the previous chapters tested the variability of the line emission over a period of several months or years. In the previous sections, the new monitoring is divided between 2022 and 2023 and the results are compared with the old monitoring modelling. To investigate the line variability on shorter timescales (e.g. 4 months), a new time grouping is adopted. The time grouping of 4-months is chosen to guarantee a minimum photon statistics of ~ 200 counts for each spectrum.

Over the period 2022-2023, five different spectra are produced, each comprising four months of observations: Jan-Apr 2022, May-Aug 2022, Sept-Dec 2022, Jan-Apr 2023, May-Aug 2023 and Sep 2023 (this latter including the last two points of the XRT light curve considered in this my analysis). Due to the low photon statistics of each spectrum ($\sim 200-400$ source net counts), the binning at 1 counts/bin is adopted for these "4-months" spectra. For simplicity, in this section we refer to the spectra using the collected months in each time grouping as labels (e.g. JanApr22-spectrum, MayAug22-spectrum). The continuum emission is fitted with an absorbed power-law plus a reflection component as before.

Considering the two consecutive spectra, JanApr22-spectrum (blue panel) and MayAug22-spectrum (pink panel), the two lines are fit at energies comparable to the best fit values found in the 2022 "summed" spectrum modelling, i.e. ~ 5.9 keV (at $< 2\sigma$) and ~ 6.3 keV (at $\sim 2-3\sigma$). Conversely, in the SeptDec22-spectrum (green panel), the emission lines are detected with low significance; in the JanApr23-spectrum (yellow panel), even a single emission line is poorly constrained (for this reason, a second emission line is not considered). Two emission lines are observed again from May-Aug 2023 (purple panel) up to September

2023 (lime panel) at best-fit energies of ~ 5.6 keV and 6.6 keV.
The variability trend is evident from Figure 6.3 and is summarized in Table 6.5. These results will be the subject of future analyses once additional observations of the XRT monitoring (already granted to our group) will be included; the main goal will consist of possibly associating the line(s) presence with the binary orbital motion.

4-months time grouping			
Spectrum	Line configuration	Line energy [keV]	Line significance [σ]
Jan-Apr 2022 spectrum	Single line	6.30 ± 0.08	3.5
	Double line	$5.89^{+0.35}_{-0.22}$ $6.31^{+0.08}_{-0.07}$	1.2
May-Aug 2022 spectrum	Single line	$6.21^{+0.20}_{-0.48}$	1.8
	Double line	$5.87^{+0.43}_{-0.31}$ $6.25^{+0.15}_{-1.22}$	1.4
Sept-Dec 2022 spectrum	Single line	$\underline{6.28}$	< 1
	Double line	$\underline{5.85}$ $\underline{6.25}$	~ 1
Jan-Apr 2023 spectrum	Single line	$\underline{6.71}$	1.1
May-Aug 2023 spectrum	Single line	$6.40^{+0.14}_{-0.13}$	2.1
	Double line	$5.89^{+0.27}_{*}$ $6.40^{+0.14}_{-0.13}$	< 1
Sept 2023 spectrum	Single line	$6.64^{+0.18}_{-0.17}$	1.2
	Double line	$5.61^{+0.10}_{-0.09}$ $6.64^{+0.13}_{-0.12}$	~ 2

Table 6.5: Summarizing the line fitting in 4-months time grouping spectra. The underlined line energy indicates that the error evaluation does not converge.

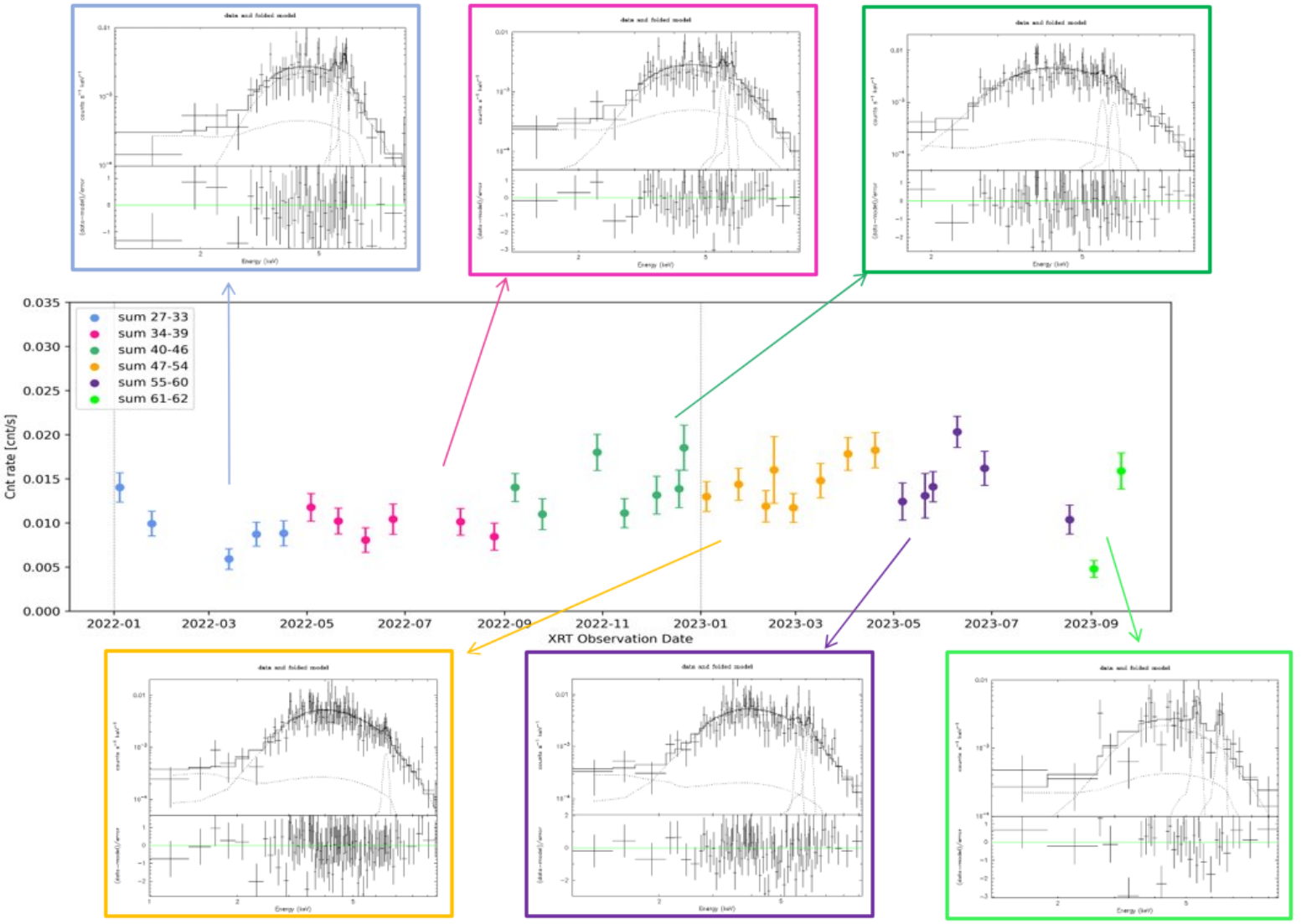

Figure 6.5: MCG+11-11-032 XRT light curve with "4-months" 1-10 keV spectra and model components (continuum modelling+ two narrow Gaussian lines). The panels are color-coded depending on the time grouping: in blue the JanApr22-spectrum, in pink the MayAug22-spectrum, in green the SeptDec22-spectrum, in yellow the JanApr22-spectrum, in purple the MayAug23-spectrum and in lime the Sept23-spectrum. The vertical dotted lines set the start of the year.

CHAPTER 7

Discussion and Conclusions

The analysis presented in my thesis aims at the detailed characterization of the line variations in MCG+11-11-032. This is a radio-quiet Seyfert type 2 galaxy at z=0.0362 and is one of the few SMBH binary candidates (relative separation of the order of milli-pc) currently known.

According to the ΛCDM cosmological framework, the SMBH binary formation is thought to be the natural outcome of the galaxy formation and evolution: when two galaxies merge, the SMBHs, hosted at the centre of each one, start to accrete and, possibly, are activated as AGN. As the merger proceeds, the two AGN approach each other and shrink at smaller and smaller separations, reaching the scale of pc/sub-pc relative distances.

MCG+11-11-032 was observed by the XRT instrument on-board of the Swift satellite. A total of 66 datatsets, both proprietary and archival ones, for a total ~ 330 ksec of exposure time, are included in our analysis. The XRT monitoring campaign enables the study of the source over a significant time interval (about 15 years) and sampling various timescales (from months to years). This is essential for evaluating potential periodic behaviors in the light curves and in the intensity and energy of the emission lines. The X-ray analysis presented in this thesis, summarized in the X-ray modeling below, provides hints of the presence of a double emission line in MCG+11-11-032 spectrum, potentially associated with a double Fe Kα line. The two emission lines, appearing and disappearing in time, result to be extremely variable in energy and intensity, a behavior in agreement with the theoretical predictions. The binary source hypothesis is reinforced by the BAT light curve analysis. The BAT light curve spans approximately 123 months, representing around 10 years of continuous monitoring, and has unveiled possible periodicity in the variability pattern over $\sim 25 - 26$ months (*Severgnini et al., 2018 [123], Serafinelli et al., 2020 [119].*

A brief summary of the thesis project carried out in this dissertation is reported here:

- **Chp. 1**. I summarized the theory on AGN, describing their structure, classification and observational properties. I focused on SMBH binary systems, pointing out the theoretical background and what is known on this topic from numerical simulations and observations by looking at the literature studies.

- **Chp. 1** In the second chapter, the principle of the X-ray telescopes is described, with

a detailed characterization of the *Swift* telescope and on-board instruments.

- **Chp. 3**. I outlined previous results found for the optical and X-ray properties of MCG+11-11-032. The source was identified as a promising SMBHB system.

- **Chp. 4**. I presented the adopted data reduction process to extract the spectra. The summing procedure is described, choosing a binning of 25 counts/bin according to the XRT energy resolution and to the Nyquist criterium. The XRT and BAT light curves are presented and analysed. A modular behavior is detected in both light curves, in particular in the 123-months BAT light curve "ups and downs" are observed on a ~ 25 months occurence (*Serafinelli et al., 2020 [119]*).

- **Chp. 5, Chp. 6 and Chp. 7**. The X-ray spectral modelling is presented and discussed in detail. Both the 2008-2016 "summed" spectrum and the 2022/2023 "summed" spectrum are considered. We verified that the manually-reduced spectra and the online-reduced ones yield consistent X-ray modelling within the errors, therefore we decided to adopt the latter procedure. For each spectrum, the fitting model comprises the continuum plus (one or two) emission line components. Up to the 2022 monitoring, double emission lines are well constrained, albeit with different best-fit parameters, but in some cases comparable within the errors (refer to Table 7.1 for a summary on the line modelling). Conversely, in the 2023 monitoring no statistically significant double emission lines was detected.

The results obtained in Chp. 5, Chp. 6 and Chp. 7 are outlined in the following paragraph.

By looking at the XRT light curve, the first approach was to split the monitoring into three groups, depending on the observational date:

- "2008-2016" summed spectrum - sum of the datasets up to 2016 (1.5 months of daily/weekly monitoring + sparse observations before 2015);

- "2022" summed spectrum - sum of the datasets obtained during the year 2022 (monthly monitoring);

- "2023" summed spectrum - sum of the datasets obtained during the year 2023 (monthly monitoring).

We defined the model components to be apply on the spectra, according to the physical processes in action for AGN. The AGN high-energy continuum emission can be divided in a direct and a reflected component: the primary component is produced by the cold accretion disk photons that are up-scattered by the hot electrons in the corona toward the observer; part of the up-scattered photons are sent back toward the nucleus and reflected, mainly by the accretion disk, where depending on their energies are subject to metal absorption, Thomson or Compton scattering. In our models, the continuum emission does not seem to

vary significantly among the three "summed" datasets, being the main parameters consistent within the errors. In particular, the photon index is in the range $[1.6-2]$, being steeper in the 2022-2023 observations, and the column density is of the order of $10^{23}\,cm^{-2}$, in agreement with the source classification as type 2 Seyfert galaxy. The observed-frame flux 2-10 keV is on average $\sim 4.5\cdot10^{-12}\,\frac{erg}{cm^2\,s}$ in the 2008-2016 spectrum modelling, while a factor $\sim 2\,(\sim 1.5)$ lower in the 2022 (2023) "summed" spectrum.

Once the continuum modelling is applied to the spectra, we found positive data-model residuals at energies of $\sim 6-7$ keV in all the "summed" spectra. For this reason, a narrow Gaussian line is included. The line modelling of the 2008-2016 "summed" spectrum produces consistent line fit with the one obtained by *S18* (see Table 7.1 for a recap). The line at $E\sim 6.24$ keV results highly significant in the 2022 monitoring (i.e. $\sim 3\sigma$), while in 2023, such emission line is not detected and only a poorly constrained emission at $E\sim 6.62$ keV is present (the significance here is below $\sim 2\sigma$). When comparing the line energy vs. normalization contour plots, the 99% confidence contour in the "2008-2016" case extends toward energies $>$ 6.2 keV (contour plot in panel **(b)** of Figure 5.5), while in the "2022" case, it extends toward energies $<$ 6.2 keV (contour plot in panel **(b)** of Figure 6.1). Subsequently, a second Gaussian narrow line component is added to the fit of the 2022 spectrum and identified at $E\sim 5.86$ keV with $\sim 2.3\sigma$ significance. The energy shift between the two line peaks detected in 2022 is of the order of $\Delta E = E_{line1} - E_{line2} = (6.25 - 5.86)\,keV = 0.39$ keV, which corresponds to a velocity offset of $\sim 0.06\,c$, compatible with what found in *S18* analysis (see Sec. 3.2).

For what concerns the 2023 monitoring, no statistically significant emission line is derived. For this reason, we tried to include in the 2023 "summed" spectrum the line detected in the "2022" summed spectrum, with the same properties in terms of line energy (~ 6.2) and intensity ($\sim 1.1\cdot10^{-13}\,\frac{erg}{cm^2\,s}$). The spectrum indicates that such a line, if present, would be of much small intensity (by a factor $\gtrsim 4$ lower).

The 2022-2023 monitoring, analysed for the first time in the current thesis work, provides new insights on the source X-ray variability, in particular on the modelling of the Fe Kα emission lines. Connecting the double and highly variable emission lines identified in MCG+11-11-032 with emission lines from a single AGN proves to be challenging. Moreover, the variability of the line energy and intensity probes further the binary hypothesis, reinforcing the scenario of periodic accretion flows from the circumbinary disk toward the circum-single disks structure or the variability related to the mini-disks orbital motion (e.g. *Serafinelli et al., 2020 [119]*).

Due to the complexity of the SMBH binary phenomenon, as a qualitative test we evaluated also the line variability on shorter scales: we adopted a "4-months" temporal binning on the 2022-2023 monitoring. We observed that the line emission around ~ 6.2 keV is present throughout 2022, but in 2023, when the fit converges, the line is not detected ($< 2\sigma$). It is only from September 2023 that a tentative double line profile is detectable ($E\sim 5.6$ keV

and $E \sim 6.6$ keV).

Additional monitoring observations are needed to place the results obtained so far on a more solid ground by confirming the observed photometric modulation and the relation of the iron lines properties (intensity, line ratio and velocity shifts) with a possible source phase. The increased exposure for each of the orbital phase will provide a higher quality spectrum at the Fe Kα energy band, which will improve our constraints on the two Fe Kα emission lines. Additional $\sim$ 100 ksec of observations with Swift-XRT were proposed by *Severgnini's group* and already accepted. The data will be acquired every 15-20 days over one year. In this context, longer light curves (also with BAT instrument) will enhance the significance of the estimated period of variability. Additionally, the source was recently observed by Chandra (data are not publicly available yet), and one XMM-Newton observation is planned. These data will not contribute to the study of the variability pattern highlighted from the monitoring campaigns, but for sure they will point out new details on the source emission thanks to the sensitivity of Chandra and the large effective area of XMM-Newton.

MODEL: Single narrow line			
	E [keV]	EW[eV]	Significance
"Summed" spectrum 08-16	$6.16^{+0.10}_{-0.08}$	98[46-154]	$\sim 2.2\sigma$
"Summed" spectrum 2022	$6.24^{+0.09}_{-0.10}$	250[122-378]	$\sim 3\sigma$
"Summed" spectrum 2023	$6.62^{+0.19}_{-0.25}$	156[12-305]	$\sim 1.5\sigma$

MODEL: Double narrow lines						
	E_1 [keV]	EW_1[eV]	Significance	E_2 [keV]	EW_2[eV]	Significance
"Summed" spectrum 08-16	6.14 ± 0.08	81[22-137]	$\sim 2.2\sigma$	$6.50^{+0.15}_{-0.14}$	97[40-166]	$\sim 1.5\sigma$
"Summed" spectrum 2022	$5.86^{+0.15}_{-0.14}$	154[42-268]	$\sim 2.3\sigma$	6.25 ± 0.09	265[127-401]	$\sim 3\sigma$

Table 7.1: Scheme of the X-ray line modeling.

7.1 Future perspectives

The search of dual/binary AGN is a hot topic in the astrophysics, in particular because of the important contribution in the framework of galaxy formation and evolution. Although gravitationally bound AGN pair emits a broad-band electromagnetic spectrum, the present-day capabilities of existing facilities in detecting binary AGN remain constrained by limitations in angular and energy resolution. For these reasons, various indirect methods have been investigated in the literature to identify and study these systems.

For what concerns imaging survey, the radio band could definitively offer one of the best angular resolution achievable, thanks to the interferometric technique. For example, the unprecedented structural sensitivity provided by the SKA baseline and the improved flux density given by the VLBI array will possibly detect a large number of dual AGN candidates and local binaries AGN down to about 0.1 pc scale of relative separation (*De Rosa et al., 2019 [28]*).

From an X-ray point of view, the ESA space mission NewAthena (expected to be launched around 2037) will combine unprecedented effective collecting area ($A_{eff} = 0.152\,m^2$ at 7 keV), high energy resolution ($\sim$ 2.5 eV below 7 keV) and enhanced sensitivity ($\sim 3 \cdot 10^{-17}\,erg\,s^{-1}\,cm^{-2}$ in the range [0.5-2] keV) thanks to both on-board imaging and spectroscopy instruments (Wield Field Imager, WFI and X-ray Integral Field Units, X-IFU). With WFI angular resolution preliminary estimate of $6''$ over the $40'$ x $40'$ FoV, the achievable AGN separation is of the order of a few tens of kpc. Thanks to the eV-like energy resolution, the X-IFU would be capable of detecting AGN pairs with binary mass ratio $q \gtrsim 0.1$ and separation of 100s of r_g (i.e. for a $M_{BH} = 10^8\,M_{sun}$, a separation $a \sim 100\,pc$ or so) (*De Rosa et al., 2019 [28]*). The spectral power of X-IFU would be of crucial importance in order to disentangle Fe features and follow their variability in emission. Following this line of reasoning, the XRISM satellite (launched in September 2023) is characterized by " "hyperspectral" resolution < 7 eV at 6 keV thanks to the Resolve X-ray micro-calorimeter and may resolve accurately the double-peaked Fe Kα profile.

One of the main signature of SMBH binary systems is their periodic variability in the UV/X-ray bands (see Chapter 4). Periodic modulation in UV and X-ray light curves is expected with periods comparable to the binary period (or semi-period). Time-domain surveys, like those provided by the LSST-Large Synoptic Survey Telescope (Rubin Observatory) expected to be operating by 2024, are a promising search tool for SMBHBs in the optical band.

Given their poor observational characterization, the search for pc/sub-pc binary systems separation goes hand in hand with cosmological theory and simulations, to properly investigate growth phenomena, the structure of the circumbinary disk and the binary evolution.

We have seen that SMBHB are loud emitters of Gravitational Waves. In particular, the collective signal from the SMBH binary population perturbs the space-time metric and af-

fects the propagation of the electromagnetic signal, detectable in millisecond pulsars periodic emission. This technique is exploited by the Pulsar Timing Array (PTA) campaigns (e.g. *Agazie et al., 2023 [2]*). On the other hand, the ground-based interferometers (Ligo-Virgo-Kagra) are not sensitive to the amplitudes and frequency of the GW produced by SMBHBs. Hence, the future LISA detector, which will benefit of space distances, will shed light on the mHz-nHz Universe for the first time with observations on $M_{BH} \sim 10^3 - 10^7\, M_{sun}$ BH mergers. The LISA source sky localisation depends on the luminosity and distance (i.e. redshift) of the interested object, in principle it could be sensitive to mergers months before the coalescence. In this way, the detected sources can be investigated with e.g. optical/X-ray follow-ups, to better characterize also the host systems.

From this picture, it is clear that a multiwavelength synergy is the mandatory approach to look for Dual/Binary AGN, combining hints from different observational bands and advanced cosmological simulations. However, the key role of X-ray studies is inevitable, being the X-ray photons less affected by gas absorption and unveiling the source innermost central regions. The pioneering (though challenging work) carried out in this thesis reveal the potentialities of the study of the double Fe Kα emission lines and their variability in the search for binary systems.

Bibliography and Sitography

[1] B. P. Abbott et al. “GW150914: First results from the search for binary black hole coalescence with Advanced LIGO”. In: 93.12, 122003 (June 2016), p. 122003. DOI: 10.1103/PhysRevD.93.122003. arXiv: 1602.03839 [gr-qc].

[2] Gabriella Agazie et al. “The NANOGrav 15 yr Data Set: Constraints on Supermassive Black Hole Binaries from the Gravitational-wave Background”. In: 952.2, L37 (Aug. 2023), p. L37. DOI: 10.3847/2041-8213/ace18b. arXiv: 2306.16220 [astro-ph.HE].

[3] D. M. Alexander and R. C. Hickox. “What drives the growth of black holes?” In: 56.4 (June 2012), pp. 93–121. DOI: 10.1016/j.newar.2011.11.003. arXiv: 1112.1949 [astro-ph.GA].

[4] R. R. J. Antonucci and J. S. Miller. “Spectropolarimetry and the nature of NGC 1068.” In: 297 (Oct. 1985), pp. 621–632. DOI: 10.1086/163559.

[5] Robert Antonucci. “Unified models for active galactic nuclei and quasars.” In: 31 (Jan. 1993), pp. 473–521. DOI: 10.1146/annurev.aa.31.090193.002353.

[6] K. A. Arnaud et al. “EXOSAT observations of a strong soft X-ray excess in MKN 841.” In: 217 (Nov. 1985), pp. 105–113. DOI: 10.1093/mnras/217.1.105.

[7] Y. Avni. “Energy spectra of X-ray clusters of galaxies.” In: 210 (Dec. 1976), pp. 642–646. DOI: 10.1086/154870.

[8] J. A. Baldwin, M. M. Phillips, and R. Terlevich. “Classification parameters for the emission-line spectra of extragalactic objects.” In: 93 (Feb. 1981), pp. 5–19. DOI: 10.1086/130766.

[9] R. Scott Barrows et al. “Identification of Outflows and Candidate Dual Active Galactic Nuclei in SDSS Quasars at z = 0.8-1.6”. In: 769.2, 95 (June 2013), p. 95. DOI: 10.1088/0004-637X/769/2/95. arXiv: 1303.3587 [astro-ph.CO].

[10] M. C. Begelman, R. D. Blandford, and M. J. Rees. “Massive black hole binaries in active galactic nuclei”. In: 287.5780 (Sept. 1980), pp. 307–309. DOI: 10.1038/287307a0.

[11] R. D. Blandford and R. L. Znajek. “Electromagnetic extraction of energy from Kerr black holes.” In: 179 (May 1977), pp. 433–456. DOI: 10.1093/mnras/179.3.433.

[12] Matteo Bonetti et al. “Post-Newtonian evolution of massive black hole triplets in galactic nuclei - I. Numerical implementation and tests”. In: 461.4 (Oct. 2016), pp. 4419–4434. DOI: 10.1093/mnras/stw1590. arXiv: 1604.08770 [astro-ph.GA].

[13] Jo Bovy et al. “Think Outside the Color Box: Probabilistic Target Selection and the SDSS-XDQSO Quasar Targeting Catalog”. In: 729.2, 141 (Mar. 2011), p. 141. DOI: 10.1088/0004-637X/729/2/141. arXiv: 1011.6392 [astro-ph.CO].

[14] Marcella Brusa. *Notes from High Energy Astrophysics, Master Degree course*. University of Bologna, 2023.

[15] S. Buttiglione et al. “An optical spectroscopic survey of the 3CR sample of radio galaxies with z $<$ 0.3 . II. Spectroscopic classes and accretion modes in radio-loud AGN”. In: 509, A6 (Jan. 2010), A6. DOI: 10.1051/0004-6361/200913290. arXiv: 0911.0536 [astro-ph.CO].

[16] Pedro R. Capelo et al. “Growth and activity of black holes in galaxy mergers with varying mass ratios”. In: 447.3 (Mar. 2015), pp. 2123–2143. DOI: 10.1093/mnras/stu2500. arXiv: 1409.0004 [astro-ph.GA].

[17] W. Cash. “Parameter estimation in astronomy through application of the likelihood ratio.” In: 228 (Mar. 1979), pp. 939–947. DOI: 10.1086/156922.

[18] Andrea Cimatti, Filippo Fraternali, and Nipoti Carlo. *Introduction to Galaxy formation and evolution*. Cambridge University Press, 2020.

[19] Shaun Cole et al. “Hierarchical galaxy formation”. In: 319.1 (Nov. 2000), pp. 168–204. DOI: 10.1046/j.1365-8711.2000.03879.x. arXiv: astro-ph/0007281 [astro-ph].

[20] BOSS Collaboration. *SDSS-III: Baryon Oscillation Spectroscopic Survey*. URL: https://www.sdss3.org/surveys/boss.php.

[21] SDSS Collaboration. *Sloan Digital Sky Survey*. URL: https://www.sdss.org/.

[22] Monica Colpi. “Massive Binary Black Holes in Galactic Nuclei and Their Path to Coalescence”. In: 183.1-4 (Sept. 2014), pp. 189–221. DOI: 10.1007/s11214-014-0067-1. arXiv: 1407.3102 [astro-ph.GA].

[23] Monica Colpi and Alberto Sesana. “Gravitational Wave Sources in the Era of Multi-Band Gravitational Wave Astronomy”. In: *An Overview of Gravitational Waves: Theory*. 2017, pp. 43–140. DOI: 10.1142/9789813141766_0002.

[24] J. Crummy et al. “An explanation for the soft X-ray excess in active galactic nuclei”. In: 365.4 (Feb. 2006), pp. 1067–1081. DOI: 10.1111/j.1365-2966.2005.09844.x. arXiv: astro-ph/0511457 [astro-ph].

[25] Stéphane d’Ascoli et al. “Electromagnetic Emission from Supermassive Binary Black Holes Approaching Merger”. In: 865.2, 140 (Oct. 2018), p. 140. DOI: 10.3847/1538-4357/aad8b4. arXiv: 1806.05697 [astro-ph.HE].

[26] M. Dadina. "Seyfert galaxies in the local Universe ($z \leq 0.1$): the average X-ray spectrum as seen by BeppoSAX". In: 485.2 (July 2008), pp. 417–424. DOI: 10.1051/0004-6361:20077569. arXiv: 0801.4338 [astro-ph].

[27] B. de Marco et al. "PG 1211+143: probing high-frequency lags in a high-mass active galactic nucleus". In: 417.1 (Oct. 2011), pp. L98–L102. DOI: 10.1111/j.1745-3933.2011.01129.x. arXiv: 1108.3503 [astro-ph.HE].

[28] Alessandra De Rosa et al. "The quest for dual and binary supermassive black holes: A multi-messenger view". In: 86, 101525 (Dec. 2019), p. 101525. DOI: 10.1016/j.newar.2020.101525. arXiv: 2001.06293 [astro-ph.GA].

[29] Tiziana Di Matteo, Volker Springel, and Lars Hernquist. "Energy input from quasars regulates the growth and activity of black holes and their host galaxies". In: 433.7026 (Feb. 2005), pp. 604–607. DOI: 10.1038/nature03335. arXiv: astro-ph/0502199 [astro-ph].

[30] Chris Done. "Observational characteristics of accretion onto black holes". In: *arXiv e-prints*, arXiv:1008.2287 (Aug. 2010), arXiv:1008.2287. DOI: 10.48550/arXiv.1008.2287. arXiv: 1008.2287 [astro-ph.HE].

[31] Chris Done et al. "Intrinsic disc emission and the soft X-ray excess in active galactic nuclei". In: 420.3 (Mar. 2012), pp. 1848–1860. DOI: 10.1111/j.1365-2966.2011.19779.x. arXiv: 1107.5429 [astro-ph.HE].

[32] M. Dotti, A. Sesana, and R. Decarli. "Massive Black Hole Binaries: Dynamical Evolution and Observational Signatures". In: *Advances in Astronomy* 2012, 940568 (Jan. 2012), p. 940568. DOI: 10.1155/2012/940568. arXiv: 1111.0664 [astro-ph.CO].

[33] Michael Eracleous and Jules P. Halpern. "Completion of a Survey and Detailed Study of Double-peaked Emission Lines in Radio-loud Active Galactic Nuclei". In: 599.2 (Dec. 2003), pp. 886–908. DOI: 10.1086/379540. arXiv: astro-ph/0309149 [astro-ph].

[34] P. A. Evans et al. "Methods and results of an automatic analysis of a complete sample of Swift-XRT observations of GRBs". In: 397.3 (Aug. 2009), pp. 1177–1201. DOI: 10.1111/j.1365-2966.2009.14913.x. arXiv: 0812.3662 [astro-ph].

[35] A. C. Fabian. "A short introduction to broad and variable iron lines around black holes". In: *Astronomische Nachrichten* 327.10 (Dec. 2006), p. 943. DOI: 10.1002/asna.200610669.

[36] A. C. Fabian et al. "Broad Iron Lines in Active Galactic Nuclei". In: 112.775 (Sept. 2000), pp. 1145–1161. DOI: 10.1086/316610. arXiv: astro-ph/0004366 [astro-ph].

[37] A. C. Fabian et al. "Properties of AGN coronae in the NuSTAR era". In: 451.4 (Aug. 2015), pp. 4375–4383. DOI: 10.1093/mnras/stv1218. arXiv: 1505.07603 [astro-ph.HE].

[38] Andrew C. Fabian and Giovanni Miniutti. "The X-ray spectra of accreting Kerr black holes". In: *arXiv e-prints*, astro-ph/0507409 (July 2005), astro–ph/0507409. DOI: 10.48550/arXiv.astro-ph/0507409. arXiv: astro-ph/0507409 [astro-ph].

[39] B. L. Fanaroff and J. M. Riley. "The morphology of extragalactic radio sources of high and low luminosity". In: 167 (May 1974), 31P–36P. DOI: 10.1093/mnras/167.1.31P.

[40] Carla & Roberto Fanti. *Una finestra sull'Universo "Invisibile"- Lezioni di radioastronomia*. Bologna, 2012.

[41] Edward Arthur Fath. "The spectra of some spiral nebulae and globular star clusters". In: *Lick Observatory Bulletin* 149 (Jan. 1909), pp. 71–77. DOI: 10.5479/ADS/bib/1909LicOB.5.71F.

[42] Laura Ferrarese and Holland Ford. "Supermassive Black Holes in Galactic Nuclei: Past, Present and Future Research". In: 116.3-4 (Feb. 2005), pp. 523–624. DOI: 10.1007/s11214-005-3947-6. arXiv: astro-ph/0411247 [astro-ph].

[43] Laura Ferrarese and David Merritt. "A Fundamental Relation between Supermassive Black Holes and Their Host Galaxies". In: 539.1 (Aug. 2000), pp. L9–L12. DOI: 10.1086/312838. arXiv: astro-ph/0006053 [astro-ph].

[44] J. W. Fried and H. Schulz. "NGC 6240 : a unique interacting galaxy." In: 118 (Feb. 1983), pp. 166–170.

[45] Hai Fu et al. "The Nature of Double-peaked [O III] Active Galactic Nuclei". In: 745.1, 67 (Jan. 2012), p. 67. DOI: 10.1088/0004-637X/745/1/67. arXiv: 1107.3564 [astro-ph.CO].

[46] Gaskin J. et al. "SuperHERO: Design of a new hard-X-ray focusing telescope". In: *Journal of Astronomical Instrumentation* (2015).

[47] Karl Gebhardt et al. "A Relationship between Nuclear Black Hole Mass and Galaxy Velocity Dispersion". In: 539.1 (Aug. 2000), pp. L13–L16. DOI: 10.1086/312840. arXiv: astro-ph/0006289 [astro-ph].

[48] N. Gehrels et al. "The Swift Gamma-Ray Burst Mission". In: 611.2 (Aug. 2004), pp. 1005–1020. DOI: 10.1086/422091. arXiv: astro-ph/0405233 [astro-ph].

[49] Gabriele Ghisellini. *Radiative Processes in High Energy Astrophysics*. Heildelberg: Springer, 2013.

[50] V. E. Gianolli et al. "Uncovering the geometry of the hot X-ray corona in the Seyfert galaxy NGC 4151 with IXPE". In: 523.3 (Aug. 2023), pp. 4468–4476. DOI: 10.1093/mnras/stad1697. arXiv: 2303.12541 [astro-ph.GA].

[51] Lei Hao et al. "The Distribution of Silicate Strength in Spitzer Spectra of AGNs and ULIRGs". In: 655.2 (Feb. 2007), pp. L77–L80. DOI: 10.1086/511973. arXiv: astro-ph/0612509 [astro-ph].

[52] C. M. Harrison. “Impact of supermassive black hole growth on star formation”. In: *Nature Astronomy* 1, 0165 (July 2017), p. 0165. DOI: 10.1038/s41550-017-0165. arXiv: 1703.06889 [astro-ph.GA].

[53] Christopher Mark Harrison. “Observational constraints on the influence of active galactic nuclei on the evolution of galaxies.” In: (2014). URL: http://etheses.dur.ac.uk/10744/.

[54] Kimitake Hayasaki. “A New Mechanism for Massive Binary Black-Hole Evolution”. In: 61 (Feb. 2009), p. 65. DOI: 10.1093/pasj/61.1.65. arXiv: 0805.3408 [astro-ph].

[55] Ryan C. Hickox and David M. Alexander. “Obscured Active Galactic Nuclei”. In: 56 (Sept. 2018), pp. 625–671. DOI: 10.1146/annurev-astro-081817-051803. arXiv: 1806.04680 [astro-ph.GA].

[56] R. G. Hine and M. S. Longair. “Optical spectra of 3CR radio galaxies.” In: 188 (July 1979), pp. 111–130. DOI: 10.1093/mnras/188.1.111.

[57] Philip F. Hopkins et al. “A Cosmological Framework for the Co-Evolution of Quasars, Supermassive Black Holes, and Elliptical Galaxies. I. Galaxy Mergers and Quasar Activity”. In: 175.2 (Apr. 2008), pp. 356–389. DOI: 10.1086/524362. arXiv: 0706.1243 [astro-ph].

[58] Philip F. Hopkins et al. “A Unified, Merger-driven Model of the Origin of Starbursts, Quasars, the Cosmic X-Ray Background, Supermassive Black Holes, and Galaxy Spheroids”. In: 163.1 (Mar. 2006), pp. 1–49. DOI: 10.1086/499298. arXiv: astro-ph/0506398 [astro-ph].

[59] Agenzia Spaziale Italiana. *Multi-Mission Interactive Archive*. URL: https://www.ssdc.asi.it/mmia/index.php?mission=swiftmastr.

[60] Fredrick A. Jenet et al. “Detecting the Stochastic Gravitational Wave Background Using Pulsar Timing”. In: 625.2 (June 2005), pp. L123–L126. DOI: 10.1086/431220. arXiv: astro-ph/0504458 [astro-ph].

[61] J. S. Kaastra and J. A. M. Bleeker. “Optimal binning of X-ray spectra and response matrix design”. In: 587, A151 (Mar. 2016), A151. DOI: 10.1051/0004-6361/201527395. arXiv: 1601.05309 [astro-ph.IM].

[62] P. M. W. Kalberla et al. “The Leiden/Argentine/Bonn (LAB) Survey of Galactic HI. Final data release of the combined LDS and IAR surveys with improved stray-radiation corrections”. In: 440.2 (Sept. 2005), pp. 775–782. DOI: 10.1051/0004-6361:20041864. arXiv: astro-ph/0504140 [astro-ph].

[63] E. Kara et al. “The curious time lags of PG 1244+026: discovery of the iron K reverberation lag.” In: 439 (Mar. 2014), pp. L26–L30. DOI: 10.1093/mnrasl/slt173. arXiv: 1311.5164 [astro-ph.HE].

[64] Guinevere Kauffmann et al. “The host galaxies of active galactic nuclei”. In: 346.4 (Dec. 2003), pp. 1055–1077. DOI: 10.1111/j.1365-2966.2003.07154.x. arXiv: astro-ph/0304239 [astro-ph].

[65] Arnaud Keith et al. *Xspec. An X-Ray Spectral Fitting Package, Users' Guide for version 12.13.1.* 2023. URL: https://heasarc.gsfc.nasa.gov/xanadu/xspec/manual/.

[66] K. I. Kellermann et al. “VLA Observations of Objects in the Palomar Bright Quasar Survey”. In: 98 (Oct. 1989), p. 1195. DOI: 10.1086/115207.

[67] Roy P. Kerr. “Gravitational Field of a Spinning Mass as an Example of Algebraically Special Metrics”. In: 11.5 (Sept. 1963), pp. 237–238. DOI: 10.1103/PhysRevLett.11.237.

[68] L. J. Kewley et al. “Theoretical Modeling of Starburst Galaxies”. In: 556.1 (July 2001), pp. 121–140. DOI: 10.1086/321545. arXiv: astro-ph/0106324 [astro-ph].

[69] S. Komossa et al. “Discovery of a Binary Active Galactic Nucleus in the Ultraluminous Infrared Galaxy NGC 6240 Using Chandra”. In: 582.1 (Jan. 2003), pp. L15–L19. DOI: 10.1086/346145. arXiv: astro-ph/0212099 [astro-ph].

[70] John Kormendy and Douglas Richstone. “Inward Bound—The Search For Supermassive Black Holes In Galactic Nuclei”. In: 33 (Jan. 1995), p. 581. DOI: 10.1146/annurev.aa.33.090195.003053.

[71] Michael Koss et al. “UNDERSTANDING DUAL ACTIVE GALACTIC NUCLEUS ACTIVATION IN THE NEARBY UNIVERSE”. In: *The Astrophysical Journal* 746.2 (Feb. 2012), p. L22. DOI: 10.1088/2041-8205/746/2/l22. URL: https://doi.org/10.1088%2F2041-8205%2F746%2F2%2Fl22.

[72] Michael J. Koss et al. “A population of luminous accreting black holes with hidden mergers”. In: 563.7730 (Nov. 2018), pp. 214–216. DOI: 10.1038/s41586-018-0652-7. arXiv: 1811.03641 [astro-ph.GA].

[73] Szymon Kozłowski. “Revisiting Stochastic Variability of AGNs with Structure Functions”. In: 826.2, 118 (Aug. 2016), p. 118. DOI: 10.3847/0004-637X/826/2/118. arXiv: 1604.05858 [astro-ph.GA].

[74] Dong Lai and Diego J. Muñoz. “Circumbinary Accretion: From Binary Stars to Massive Binary Black Holes”. In: 61 (Aug. 2023), pp. 517–560. DOI: 10.1146/annurev-astro-052622-022933. arXiv: 2211.00028 [astro-ph.HE].

[75] Isabella Lamperti et al. “BAT AGN Spectroscopic Survey - IV: Near-Infrared Coronal Lines, Hidden Broad Lines, and Correlation with Hard X-ray Emission”. In: 467.1 (May 2017), pp. 540–572. DOI: 10.1093/mnras/stx055. arXiv: 1701.02755 [astro-ph.GA].

[76] G. Lanzuisi et al. “The Chandra COSMOS Legacy Survey: Compton thick AGN at high redshift”. In: 480.2 (Oct. 2018), pp. 2578–2592. DOI: 10.1093/mnras/sty2025. arXiv: 1803.08547 [astro-ph.GA].

[77] D. A. Leahy et al. “On searches for pulsed emission with application to four globular cluster X-ray sources : NGC 1851, 6441, 6624 and 6712.” In: 266 (Mar. 1983), pp. 160–170. DOI: 10.1086/160766.

[78] University of Leicester. *Data analysis. Build Swift-XRT products.* URL: https://www.swift.ac.uk/user_objects/.

[79] University of Leicester. *Swift: Catching Gamma Ray Bursts on the Fly.* URL: https://www.swift.ac.uk/about/index.php.

[80] University of Leicester. *XRT Data Analysis.* URL: https://www.swift.ac.uk/analysis/xrt/.

[81] University of Leicester. *XRT Data Analysis, Software Guide.* URL: https://www.swift.ac.uk/analysis/xrt/files/xrt_swguide_v1_2.pdf.

[82] Malcolm S. Longair. *High Energy Astrophysics.* Cambridge: Cambridge University Press, 2011.

[83] Piero Madau and Mark Dickinson. “Cosmic Star-Formation History”. In: 52 (Aug. 2014), pp. 415–486. DOI: 10.1146/annurev-astro-081811-125615. arXiv: 1403.0007 [astro-ph.CO].

[84] Pawel Magdziarz and Andrzej A. Zdziarski. “Angle-dependent Compton reflection of X-rays and gamma-rays”. In: 273.3 (Apr. 1995), pp. 837–848. DOI: 10.1093/mnras/273.3.837.

[85] John Magorrian et al. “The Demography of Massive Dark Objects in Galaxy Centers”. In: 115.6 (June 1998), pp. 2285–2305. DOI: 10.1086/300353. arXiv: astro-ph/9708072 [astro-ph].

[86] A. Malizia et al. “BeppoSAX Average Spectra of Seyfert Galaxies”. In: 589.1 (May 2003), pp. L17–L20. DOI: 10.1086/375712. arXiv: astro-ph/0304133 [astro-ph].

[87] Federico Marulli et al. “The spatial distribution of X-ray selected AGN in the Chandra deep fields: a theoretical perspective”. In: 396.3 (July 2009), pp. 1404–1414. DOI: 10.1111/j.1365-2966.2009.14851.x. arXiv: 0904.0256 [astro-ph.CO].

[88] I. McHardy. “X-Ray Variability of AGN and Relationship to Galactic Black Hole Binary Systems”. In: *Lecture Notes in Physics, Berlin Springer Verlag.* Ed. by Tomaso Belloni. Vol. 794. 2010, p. 203. DOI: 10.1007/978-3-540-76937-8_8.

[89] Maggiore Michele. *Gravitational Waves : Volume 1: Theory and Experiments*. OUP Oxford, 2007. ISBN: 9780198570745. URL: http://ezproxy.unibo.it/login?url=https://search.ebscohost.com/login.aspx?direct=true&db=nlebk&AN=215694&site=ehost-live&scope=site.

[90] M. Middleton. "Black Hole Spin: Theory and Observation". In: *Astrophysics of Black Holes: From Fundamental Aspects to Latest Developments*. Ed. by Cosimo Bambi. Vol. 440. Astrophysics and Space Science Library. Jan. 2016, p. 99. DOI: 10.1007/978-3-662-52859-4_3. arXiv: 1507.06153 [astro-ph.HE].

[91] Miloš Milosavljević and David Merritt. "The Final Parsec Problem". In: *The Astrophysics of Gravitational Wave Sources*. Ed. by Joan M. Centrella. Vol. 686. American Institute of Physics Conference Series. Oct. 2003, pp. 201–210. DOI: 10.1063/1.1629432. arXiv: astro-ph/0212270 [astro-ph].

[92] Michele Ennio Maria Moresco and Carlo Nipoti. *Gravitational Wave Astrophysics and Cosmology, Master Degree course*. University of Bologna, 2023.

[93] Alberto Moretti et al. "SWIFT XRT point spread function measured at the Panter end-to-end tests". In: *X-Ray and Gamma-Ray Instrumentation for Astronomy XIII*. Ed. by Kathryn A. Flanagan and Oswald H. W. Siegmund. Vol. 5165. Society of Photo-Optical Instrumentation Engineers (SPIE) Conference Series. Feb. 2004, pp. 232–240. DOI: 10.1117/12.504857.

[94] R. Morrison and D. McCammon. "Interstellar photoelectric absorption cross sections, 0.03-10 keV." In: 270 (July 1983), pp. 119–122. DOI: 10.1086/161102.

[95] A. Mücke et al. "Photomeson production in astrophysical sources". In: *Nuclear Physics B Proceedings Supplements* 80 (Jan. 2000), pp. 08/10. DOI: 10.48550/arXiv.astro-ph/9905153. arXiv: astro-ph/9905153 [astro-ph].

[96] Ramesh Narayan and Insu Yi. "Advection-dominated Accretion: Underfed Black Holes and Neutron Stars". In: 452 (Oct. 1995), p. 710. DOI: 10.1086/176343. arXiv: astro-ph/9411059 [astro-ph].

[97] NASA. *ΛCDM Model of Cosmology*. URL: https://lambda.gsfc.nasa.gov/education/graphic_history/univ_evol.html.

[98] Nasa. *Neil Geherls Swift Observatory*. URL: https://swift.gsfc.nasa.gov/.

[99] Nasa. *Swift Fact Sheet*. URL: https://swift.gsfc.nasa.gov/about_swift/Sci_Fact_Sheet.pdf.

[100] Hagai Netzer. "Revisiting the Unified Model of Active Galactic Nuclei". In: 53 (Aug. 2015), pp. 365–408. DOI: 10.1146/annurev-astro-082214-122302. arXiv: 1505.00811 [astro-ph.GA].

[101] Hagai Netzer. *The Physics and Evolution of Active Galactic Nuclei*. 2013.

[102] D. E. Osterbrock. “Seyfert galaxies with weak broad H alpha emission lines”. In: 249 (Oct. 1981), pp. 462–470. DOI: 10.1086/159306.

[103] P. Padovani et al. “Active galactic nuclei: what’s in a name?” In: 25.1, 2 (Aug. 2017), p. 2. DOI: 10.1007/s00159-017-0102-9. arXiv: 1707.07134 [astro-ph.GA].

[104] Giovanni Pareschi, Daniele Spiga, and Carlo Pelliciari. *The WSPC Handbook of Astronomical Instrumentation. Volume 4: X-Ray Astronomical Instrumentation. Chapter 1.* World Scientific Series in Astrophysics, 2023. DOI: 10.1142/9789811203800_0001.

[105] PennState. *Mission Operations Center for Swift-XRT Optics*. URL: https://www.swift.psu.edu/xrt/optics.php.

[106] M. Perna et al. “The ultra-dense, interacting environment of a dual AGN at z $\sim$ 3.3 revealed by JWST/NIRSpec IFS”. In: *arXiv e-prints*, arXiv:2304.06756 (Apr. 2023), arXiv:2304.06756. DOI: 10.48550/arXiv.2304.06756. arXiv: 2304.06756 [astro-ph.GA].

[107] Bradley M. Peterson. “Toward Precision Measurement of Central Black Hole Masses”. In: *Co-Evolution of Central Black Holes and Galaxies*. Ed. by Bradley M. Peterson, Rachel S. Somerville, and Thaisa Storchi-Bergmann. Vol. 267. May 2010, pp. 151–160. DOI: 10.1017/S1743921310006095. arXiv: 1001.3675 [astro-ph.GA].

[108] E. Piconcelli et al. “The XMM-Newton view of PG quasars. I. X-ray continuum and absorption”. In: 432.1 (Mar. 2005), pp. 15–30. DOI: 10.1051/0004-6361:20041621. arXiv: astro-ph/0411051 [astro-ph].

[109] Luka Č. Popović. “Super-massive binary black holes and emission lines in active galactic nuclei”. In: 56.2-3 (Feb. 2012), pp. 74–91. DOI: 10.1016/j.newar.2011.11.001. arXiv: 1109.0710 [astro-ph.CO].

[110] L. A. Pozdnyakov, I. M. Sobol, and R. A. Syunyaev. “Comptonization and the shaping of X-ray source spectra - Monte Carlo calculations”. In: 2 (Jan. 1983), pp. 189–331.

[111] Cristina Ramos Almeida and Claudio Ricci. “Nuclear obscuration in active galactic nuclei”. In: *Nature Astronomy* 1 (Oct. 2017), pp. 679–689. DOI: 10.1038/s41550-017-0232-z. arXiv: 1709.00019 [astro-ph.GA].

[112] C. S. Reynolds and A. C. Fabian. “Warm absorbers in active galactic nuclei”. In: 273.4 (Apr. 1995), pp. 1167–1176. DOI: 10.1093/mnras/273.4.1167. arXiv: astro-ph/9502006 [astro-ph].

[113] Christopher S. Reynolds and Michael A. Nowak. “Fluorescent iron lines as a probe of astrophysical black hole systems”. In: 377.6 (Apr. 2003), pp. 389–466. DOI: 10.1016/S0370-1573(02)00584-7. arXiv: astro-ph/0212065 [astro-ph].

[114] C. Ricci et al. “Growing supermassive black holes in the late stages of galaxy mergers are heavily obscured”. In: 468.2 (June 2017), pp. 1273–1299. DOI: 10.1093/mnras/stx173. arXiv: 1701.04825 [astro-ph.HE].

[115] C. Ricci et al. “Reflection in Seyfert galaxies and the unified model of AGN”. In: 532, A102 (Aug. 2011), A102. DOI: 10.1051/0004-6361/201016409. arXiv: 1104.3676 [astro-ph.CO].

[116] G. Risaliti et al. “Probing general relativistic effects during active galactic nuclei X-ray eclipses”. In: 417.1 (Oct. 2011), pp. 178–183. DOI: 10.1111/j.1365-2966.2011.19055.x. arXiv: 1105.2318 [astro-ph.CO].

[117] M. Schmidt and R. F. Green. “Quasar evolution derived from the Palomar bright quasar survey and other complete quasar surveys.” In: 269 (June 1983), pp. 352–374. DOI: 10.1086/161048.

[118] ASI; SDSS. *Swift*. URL: https://swift.asdc.asi.it/.

[119] Roberto Serafinelli et al. “Unveiling Sub-pc Supermassive Black Hole Binary Candidates in Active Galactic Nuclei”. In: 902.1, 10 (Oct. 2020), p. 10. DOI: 10.3847/1538-4357/abb3c3. arXiv: 2009.06662 [astro-ph.HE].

[120] Alberto Sesana, Francesco Haardt, and Piero Madau. “Interaction of Massive Black Hole Binaries with Their Stellar Environment. I. Ejection of Hypervelocity Stars”. In: 651.1 (Nov. 2006), pp. 392–400. DOI: 10.1086/507596. arXiv: astro-ph/0604299 [astro-ph].

[121] Alberto Sesana, Francesco Haardt, and Piero Madau. “Interaction of Massive Black Hole Binaries with Their Stellar Environment. II. Loss Cone Depletion and Binary Orbital Decay”. In: 660.1 (May 2007), pp. 546–555. DOI: 10.1086/513016. arXiv: astro-ph/0612265 [astro-ph].

[122] P. Severgnini et al. “Supermassive Black Hole Binaries and dual AGN”. In: 93.2-3 (Nov. 2022), p. 74. DOI: 10.36116/MEMSAIT_93N2_3.2022.9.

[123] P. Severgnini et al. “Swift data hint at a binary supermassive black hole candidate at sub-parsec separation”. In: 479.3 (Sept. 2018), pp. 3804–3813. DOI: 10.1093/mnras/sty1699. arXiv: 1806.10150 [astro-ph.HE].

[124] Carl K. Seyfert. “Nuclear Emission in Spiral Nebulae.” In: 97 (Jan. 1943), p. 28. DOI: 10.1086/144488.

[125] N. I. Shakura and R. A. Sunyaev. “Black holes in binary systems. Observational appearance.” In: 24 (Jan. 1973), pp. 337–355.

[126] K. P. Singh, G. P. Garmire, and J. Nousek. “Observations of Soft X-Ray Spectra from a Seyfert 1 and a Narrow Emission-Line Galaxy”. In: 297 (Oct. 1985), p. 633. DOI: 10.1086/163560.

[127] Kulinder Pal Singh. “Grazing incidence optics for X-ray astronomy, X-ray optics”. In: *Optical Society of India* (2011).

[128] S. Soldi et al. “Long-term variability of AGN at hard X-rays”. In: 563, A57 (Mar. 2014), A57. DOI: 10.1051/0004-6361/201322653. arXiv: 1311.4164 [astro-ph.HE].

[129] Volker Springel, Tiziana Di Matteo, and Lars Hernquist. “Black Holes in Galaxy Mergers: The Formation of Red Elliptical Galaxies”. In: 620.2 (Feb. 2005), pp. L79–L82. DOI: 10.1086/428772. arXiv: astro-ph/0409436 [astro-ph].

[130] Seppe Staelens and Gijs Nelemans. “The Astrophysical Gravitational Wave Background in the mHz band is likely dominated by White Dwarf binaries”. In: *arXiv e-prints*, arXiv:2310.19448 (Oct. 2023), arXiv:2310.19448. DOI: 10.48550/arXiv.2310.19448. arXiv: 2310.19448 [astro-ph.HE].

[131] *Swift BAT 157-Month Hard X-ray Survey*. 2019. URL: https://swift.gsfc.nasa.gov/results/bs157mon/.

[132] Yike Tang, Zoltán Haiman, and Andrew MacFadyen. “The late inspiral of supermassive black hole binaries with circumbinary gas discs in the LISA band”. In: 476.2 (May 2018), pp. 2249–2257. DOI: 10.1093/mnras/sty423. arXiv: 1801.02266 [astro-ph.HE].

[133] Corbin Taylor and Christopher S. Reynolds. “X-Ray Reverberation from Black Hole Accretion Disks with Realistic Geometric Thickness”. In: 868.2, 109 (Dec. 2018), p. 109. DOI: 10.3847/1538-4357/aae9f2. arXiv: 1808.07877 [astro-ph.HE].

[134] C. Megan Urry and Paolo Padovani. “Unified Schemes for Radio-Loud Active Galactic Nuclei”. In: 107 (Sept. 1995), p. 803. DOI: 10.1086/133630. arXiv: astro-ph/9506063 [astro-ph].

[135] F. Vagnetti et al. “Ensemble X-ray variability of active galactic nuclei. II. Excess variance and updated structure function”. In: 593, A55 (Sept. 2016), A55. DOI: 10.1051/0004-6361/201629057. arXiv: 1607.02629 [astro-ph.GA].

[136] Eugene Vasiliev, Fabio Antonini, and David Merritt. “The Final-parsec Problem in the Collisionless Limit”. In: 810.1, 49 (Sept. 2015), p. 49. DOI: 10.1088/0004-637X/810/1/49. arXiv: 1505.05480 [astro-ph.GA].

[137] C. Vignali et al. “Probing black hole accretion in quasar pairs at high redshift”. In: 477.1 (June 2018), pp. 780–790. DOI: 10.1093/mnras/sty682. arXiv: 1803.08508 [astro-ph.GA].

[138] Cristian Vignali. *Notes from Active Galactic Nuclei and Supermassive Black Holes, Master Degree course*. University of Bologna, 2021.

[139] Marta Volonteri, Francesco Haardt, and Piero Madau. “The Assembly and Merging History of Supermassive Black Holes in Hierarchical Models of Galaxy Formation”. In: 582.2 (Jan. 2003), pp. 559–573. DOI: 10.1086/344675. arXiv: astro-ph/0207276 [astro-ph].

[140] Jian-Min Wang et al. “Active Galactic Nuclei with Double-Peaked Narrow Lines: Are they Dual Active Galactic Nuclei?” In: 705.1 (Nov. 2009), pp. L76–L80. DOI: 10.1088/0004-637X/705/1/L76. arXiv: 0910.0580 [astro-ph.CO].

[141] S. D. M. White and M. J. Rees. “Core condensation in heavy halos: a two-stage theory for galaxy formation and clustering.” In: 183 (May 1978), pp. 341–358. DOI: 10.1093/mnras/183.3.341.

[142] D. R. Wilkins and A. C. Fabian. “Determination of the X-ray reflection emissivity profile of 1H 0707-495”. In: 414.2 (June 2011), pp. 1269–1277. DOI: 10.1111/j.1365-2966.2011.18458.x. arXiv: 1102.0433 [astro-ph.HE].

[143] Colleen A. Wilson-Hodge et al. “When a Standard Candle Flickers”. In: 727.2, L40 (Feb. 2011), p. L40. DOI: 10.1088/2041-8205/727/2/L40. arXiv: 1010.2679 [astro-ph.HE].

[144] Charles Zivancev, Jeremiah Ostriker, and Andreas H. W. Küpper. “The fates of merging supermassive black holes and a proposal for a new class of X-ray sources”. In: 498.3 (Nov. 2020), pp. 3807–3816. DOI: 10.1093/mnras/staa2581. arXiv: 2004.06083 [astro-ph.GA].